Channel Modeling in small cell and millimeter-wave scenarios

Qi Hong

Department of Electronic and Electrical Engineering
University of Sheffield

This thesis is submitted for the approval of the
Doctor of Philosophy

August 2018

Acknowledgements

I would like to express the deepest appreciation to my supervisor Professor Jie Zhang, who has the attitude and the substance of a genius: he continually and convincingly conveyed a spirit of adventure in regard to research and scholarship, and an excitement in regard to teaching. Without his guidance and persistent help this dissertation would not have been possible. Besides, I would like to thank Dr. Xiaoli Chu for her great support in my entire study.

I would like to thank Dr. Jiliang Zhang, whose work demonstrated to me that concern for global affairs supported by an “engagement” in comparative literature and modern technology, should always transcend academia and provide a quest for our times. Without his precious support it would not be possible to conduct this research.

A thank you to my colleagues, Mr. Baoling Zhang, Mr. Haonan Hu, Mr. Hao Li, Ms. Hui Zheng, Mr. Weijie Qi and Mr. Kan Lin who gave me their help and time in listening to me and helping me work out my problems during the difficult course of the thesis. A special mention goes to Mr. Tian Feng, Mr. Shuaida Ji, and Ms. Lukai Zheng, who have shared many happy memories in my leisure time.

In addition, please allow me to express my sincere appreciation to the examiners of this thesis, Prof. Chengxiang Wang and Dr. Salam Khamas, for the most valuable suggestions and corrections to improve the quality of the thesis.

Last but not the least, I would like to thank my family: my parents (Keyan Hong, Hui Zhou), my wife Xuexue Shen and son Zichen Hong, for supporting me spiritually throughout my life.

Abstract

One common feature of the research works on future wireless communication technologies is the pursuit of high spectral efficiency while multiple mobile stations access the network. The small cell and the millimter-wave are two key enabling technologies to tackle these challenges. To thoroughly investigate small cell and millimeter-wave, it is essential to have a good understanding of radio-propagation characteristics of transmission path between a base station and an mobile station which are small cell channel model and millimeter-wave channel model.

In this study, we first investigate the problem of elevation angle in the three-dimensional (3-D) channel model. The impact of antenna height on elevation angle of departure (EAoD) and elevation angle of arrival (EAoA) is investigated under typical outdoor scenarios: straight street, fork road, and crossroad. The closed-form joint and marginal probability density functions (PDFs) of both the EAoD and the EAoA are obtained through simulations. With the derived PDF equations, the related angle spread and delay spread are also presented. We give the conclude that the characteristics of EAoD and EAoA change dramaticlly when the base station antenna height is half of the building's height in the forked road and crossroad scenarios. Moreover, the results of the angle spread and the delay spread show that in order to obtain the maximum or minimum value of the angle spread and the delay spread, the base station antenna should be deployed at half of the building's height.

Then we propose an elevation angle model for small cell environment with geometrically based single bounce method. We investigate two scattering models in this study: in the first case, it is assumed that scattering objects are located uniformly within an ellipse around the mobile station; in the second case, the ellipse scattering model was extended to a 3-D model. Closed-form expressions for PDF of the EAoD are derived and validated by Monte Carlo simulation.

With our proposed PDF, the spatial correlation is discussed. The results show that the distance between the base station and the mobile station affects the spatial correlation more patently than the base station antenna height.

After researching the small cell channel model, we investigate the millimeter-wave channel model at last. The diffuse scattering effect on the millimeter-wave is investigated using typical building structures through measurement. We proposed an algorithm to separate the two referred rays when performing the measurement. Some notable results on the relationship between the scattering lobe parameters and the incident angle are gained. With the obtained values, the power of the diffuse reflection rays can be calculated and used to generate the diffuse scattering in 3-D ray launching tool.

List of Publications

Published

1. **Q. Hong**, J. Zhang, H. Zheng, H. Li, H. Hu, B. Zhang, Z. Lai, and J. Zhang, "The impact of antenna height on 3D-MIMO channel: a ray launching based analysis,"*MDPI. Electronics*, vol. 7, no. 2, 2018.

2. **Q. Hong**, H. Hu, H. Li, H. Zheng, B. Zhang and J. Zhang, "A Proposed Elevation Angle Model for Small Cell Environments," *IEEE Signal Processing and Integrated Networks.*, Accepted.

3. H. Li, J. Zhang, **Q. Hong**, H. Zheng, and J. Zhang, "Digraph-based joint routing and resource allocation in software-defined backhaul networks," in *2017 IEEE 22nd International Workshop on Computer Aided Modeling and Design of Communication Links and Networks (CAMAD)*, pp. 1-5, 2017.

4. H. Li, J. Zhang, **Q. Hong**, H. Zheng, and J. Zhang, "QoS-aware channel-width adaptation in wireless mesh networks," in *2016 IEEE International Conference on Communications (ICC)*, pp. 1-6, 2016.

Table of contents

List of figures

List of tables

List of Abbreviations

AoA	Angle of Arrival
AoD	Angle of Departure
AS	Angle Spread
BS	Base Station
CDF	Cumulative Distribution Function
DS	Delay Spread
EAoA	Elevation Angle of Arrival
EAoD	Elevation Angle of Departure
GBSB	Geometrical Based Single Bounce
GBSM	Geometry-Based Stochastic Physical Model
HDR	Horizontal Diffraction and Reflection
IRLA	Intelligent Ray Launching Algorithm
LOS	Light-Of-Sight
LTE	Long-term Evolution

MEDE	Minimum Euclidean Distance Estimator
MIMO	Multiple-input Multiple-output
MS	Moble Station
MU	Multi User
NGBSM	Non-Geometry Based Stochastic Physical Model
PDF	Probability Distribution Function
QoS	Quality of Service
RL	Ray Launching
RT	Ray Tracing
SCM	Spatial Channel Model
VD	Vertical Diffraction
VNA	Vector Network Analyzer

List of Symbols

h_{ij}	the sub-channel from the ith transmitter antenna to the jth receiver antenna
$\Delta_{N,M,AoD}$	the AoD of the M subpath in N main path
$\Delta_{N,M,AoA}$	the AoA of the M subpath in N main path
$\lambda_{1,2EAoD}$	the rate parameters of EAoD double-sided exponential functions
$\lambda_{1,2EAoA}$	the rate parameters of EAoA double-sided exponential functions
$f_{EAoD,EAoA}(x)$	the PDF of EAoD or EAoA
σ_{AS}	the angle dispersion of multipath components
σ_{DS}	the time dispersion of multipath components
P_i	the power of ith ray
$F(\theta)$	the CDF
$f_1(\theta)$	the normalization constant of $f(\theta)$
$R_{m,n}$	the spatial correlation coefficient
$\Phi_{m,n}(\theta)$	the phase for mth and nth arrays
V	the volume
E	the the norms of the incident or scattered field

Δ_Ω	the AoD impinging on the scattering surface
K	a constant depending on the amplitude of the impinging wave
δ_s	the area of scattering
$\Gamma_{1,2}$	the amplitudes of the rays
Δt	the time difference between the single reflection ray and second reflection ray

Chapter 1

Introduction

Overview

In this chapter, the background of the thesis will be introduced. Small cell and millimeter-wave technologies have been proposed to address the growing demand for high-data services with the advent of the 5G (5th-Generation Wireless Systems) era. Thus, this thesis aims to investigate the crucial characteristics of these two technologies. The principal objectives are first proposed, and then, the structure of the thesis as well as an overview of its contributions is presented.

1.1 Background and Motivation

With the formation development of a network society, there has been a significant demand for better user experience. Thus, more data traffic is required, owing to the significant increase in the number of smartphones, tablet computers, and other network devices [1]. In 2017, the overall demand should reach 11 exabytes (6×1018 bytes) per month [2]. Moreover, some evidence shows that almost 1000-fold data traffic will be needed in this decade, which is a significant challenge for the wireless industry [3]. To tackle this problem, the following two critical technologies have been developed: small cell and millimeter-wave technologies. To thoroughly investigate small cell and millimeter-wave technologies, it is essential to have a good understanding of the radio-propagation characteristics of the transmission path between the base station (BS) and the mobile station (MS) . Therefore, small cell channel model and millimeter-wave channel model need to be researched.

1.1.1 Small cells

Small cells are radio access point with low power and short range. They are operator-controlled and always installed at households or in hotspot areas. Small cell BSs exhibit similar features to those of macrocell BSs, with the main differences being the cost of small cell is cheaper, the power of small cell is much lower, and the range of small cell is shorter (usually 10 meters to hundreds meters). The reasons why small cells are useful are summarised as follows[4]:

- Due to the low interference, the same spectrum can be allocated to the users in a given area, and hence, the spectrum utilization can be increased.

- Macrocell BSs can allocate their resource more reasonably because the small cells can deal with the data traffic originating in their area.

- As small cells serve only a few users, the quality of service (QoS) for each user can be guaranteed.

Despite the benefits, in order to deploy numerous small cells, operators must face the challenge of backhauling the network traffic from small cell BSs to the core network. Moreover, it is need to minimize signaling load to the core network due to increasing numbers of small cells.

1.1.2 Milllimeter-wave

A Millimetre-wave usually refers to the frequency spectrum ranging from 30GHz to 300GHz and wavelength ranging between 1 and 10 mm.

By using more bandwidth and antennas, long-term evolution (LTE) can significantly increase the capacity and boost QoS provided to the users. However, the current LTE technology is not

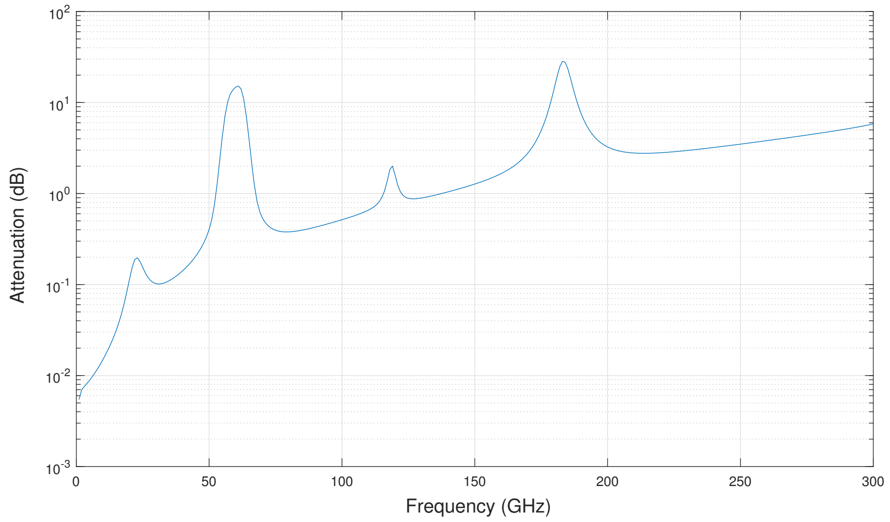

Fig. 1.1 Attenuation at different frequency bands [7].

sufficient for meeting the data traffic demands of users. An effective way to solve this problem is using the millimeter-wave band, such as 60GHz band. In [6], the author indicates that around 8 GHz bandwidth is available for 60GHz wireless communication. However, a 60 GHz wireless channel has 20-40 dB more free-space path loss and atmospheric absorption ranging from 15-30 dB/km than 5GHz channel, as shown in Fig. 1.1.

This attenuation limits the 60GHz band to only short-range communication. Especially for indoor environment, the attenuation cannot be ignored. Furthermore, the transceivers face some design challenges, including limited amplifier gain and increased phase noise. These problems limit the application of millimeter-wave technology.

1.1.3 Channel model

In simple terms, a channel is the way in which a signal travels from a transmitter to a receiver, and constitutes all transmission mediums from the transmitter to the receiver, as shown in Fig. 1.2.

The multiple-input multiple-output (MIMO) technology develop rapid over the past decade. It promises significant improvements in spectral efficieny and network coverage[9]. In addition, actual products have also been used for the wireless market. In order to accurate assess and design

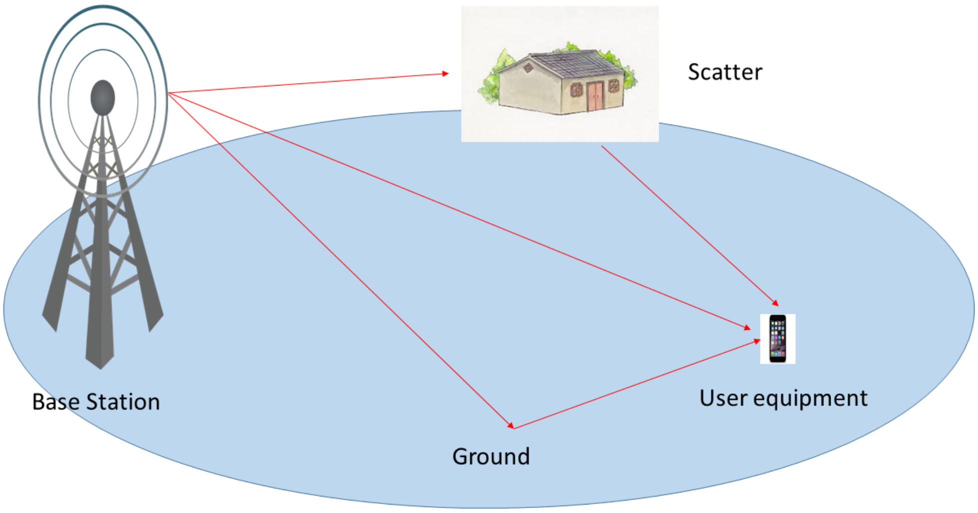

Fig. 1.2 Channel.

the cooperative MIMO systems, realistic cooperative MIMO channel models are introduced [8]. Therefore, when considering the channel model, more attention is paid to the MIMO channel model.

The MIMO system differs from a classic communication system in that it equips multiple antennas at both the transmitter and receiver. Thus, for the MIMO channel, all antenna pairs at the transmitter and receiver should be considered. Assuming that there is an $i \times j$ MIMO system, which means i antennas at the transmitter and j antennas at the receiver, the MIMO channel can be represented as an $i \times j$ matrix [10]:

$$H = \begin{pmatrix} h_{11} & h_{12} & \cdots & h_{1j} \\ h_{21} & h_{22} & \cdots & h_{2j} \\ \vdots & \ddots & \cdots & \vdots \\ h_{i1} & h_{i2} & \cdots & h_{ij} \end{pmatrix} \tag{1.1}$$

where, h_{ij} means the sub-channel from the ith transmitter antenna to the jth receiver antenna.

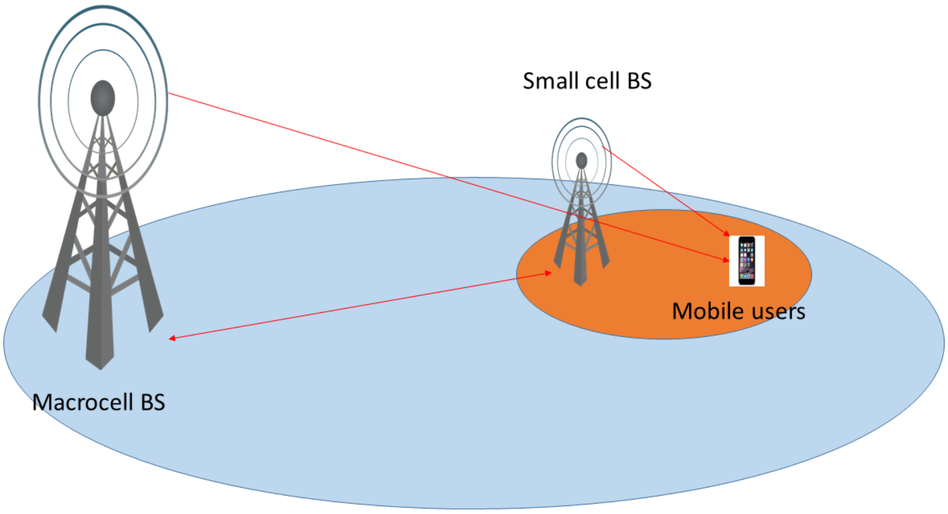

Fig. 1.3 Small cell channel VS Macrocell channel.

Small cell channel model

Conventional studies on a channel model always focus on the horizontal plane, because the distance between a BS and a MS is larger than the height of the BS. However, with a large deployment of small cells and the short coverage of small cell BS, the effect of BS height cannot be ignored, as shown in Fig. 1.3. This figure also indicates that the importance of BS height is one of the main differences between a small cell channel model and a conventional macrocell channel model, which is the main theme of the present study. For simplicity, we only consider the spherical wave transmission model during our research.

Millimeter-wave channel model

Some groups such as the IEEE 802.15.3c, which is called TG3c, are trying to develop a standard for a millimeter-wave-based alternative physical layer extension. A significant challenge in developing this standard is to confirm the propagation characteristics of the frequency band. Therefore, appropriate millimeter-wave channel models are urgently required.

Radio waves in millimeter band have high frequency, high atmospheric attenuation, short range, significant humidity absorption and rain attenuation. Based on these characteristics of millimeter-wave technology, there are some distinct differences between the millimeter-wave channel model and the typical channel model:

- Because of the high signal propagation loss for millimeter-wave technology, more directional antennas are used than omni-directional antennas.

- A slight change in position causes large fading [11].

- The multipath in the millimeter-wave band shows less effect on the channel model than the classic low-frequency band [12].

- In the millimeter-wave band, the effect of diffuse scattering has to be considered during channel modeling because the roughness of the reflection surface cannot be ignored as compared to the wavelength, where diffuse scattering refers to the scattering of signals in several directions rather than a particular direction [13].

Among these challenges, this thesis focuses on two problems in millimeter-wave band. One is the diffuse scattering, the other one is: in order to obtain the specular reflection ray in millimeter-wave measurements, we need to find a best method to reduce the effect of the multiple reflection rays.

1.1.4 Motivation of the Thesis

Over the last decades, indoor small cell channel models based on point-to-point methods have been extensively studied. However, with the introduction of small cells, the structure of the entire wireless network has become more complicated. Thus, system models based on not only the properties of individual links (point-to-point links), but also the variations and collections of multiple links at system level should be considered.

One main challenge in small cell channel model is the angle distribution, especially the Probability Distribution Functions (PDFs) of the angle of departure (AoD) and angle of arrival

(AoA) under some typical scenarios. Previous work indicated that the heights of the antennas at both the BS and the MS significantly impact the distribution of elevation angle of departure (EAoD) and elevation angle of arrival (EAoA) [14]. Therefore, we will first focus on the PDFs of EAoD and EAoA under three typical scenarios: the straight street, the forked road, and the crossroad.

The first research in our work is based on one algorithm and some numerical data. Although some notable results are obtained, they are scenario-limited. Therefore, the following research will focus on the theoretical derivation. Meanwhile, with the universally deployed small cells, the conventional study on channel which focus on the 2-D channel is invalid because of the smaller serving distance of small cells. Therefore, to precisely describe the small cell channel model, the 3-D small cell channel model is introduced. Thus, the 2-D and 3-D channel models will be investigated together in our second research.

After investigating the small cell channel model, the millimeter-wave channel model, which is another important technology for next-generation mobile communication, will be considered. In order to best understand the millimeter-wave channel, some measurements need to be performed to test the millimeter-wave propagation characteristics under different materials. We finally perform the measurements and analyse the data obtained from the measurements.

1.2 Objectives of the Thesis

With the results, the principal objectives of the thesis can be summarised as follows:

- To present an overview of the small cell and millimeter-wave channel models.

- To investigate the impact of antenna height on the channel characteristics of the 3-D MIMO channel. Three typical street scenarios, i.e., the straight street, the forked road, and the crossroad, are selected as benchmarks. The characteristics of the PDFs of EAoD will be obtained under different street scenarios.

• To propose scattering models in small cell scenarios, for which the PDFs of the EAoD and EAoA will be derived and verified.

• To perform the measurements and process the obtained data. The results shed light on how to take diffuse scattering into account in the millimeter-wave channel model.

1.3 Structure of the Thesis

The remainder of this chapter is organised as follows:

Chapter 2: Literature review

This chapter will present an overview of the small cell and millimeter-wave technologies. The classic channel model, together with the small cell channel model and millimeter-wave channel model, is also introduced.

Chapter 3: The Impact of Antenna Height on 3D Channel: a Ray Launching Based Analysis

The impact of antenna height on the channel characteristics of the 3-D MIMO channel is investigated. Three typical street scenarios, i.e., the straight street, the forked road, and the crossroad, are selected as benchmarks. The PDFs of both the EAoD and the EAoA are obtained through simulations. Moreover, the elevation angle spread (AS) and elevation delay spread (DS) under various antenna heights are jointly discussed.

Contributions: 1) The PDFs of EAoD and EAoA are derived in closed-forms under three typical scenarios. We observe that the PDFs of EAoD and EAoA are almost linearly correlated with the antenna height under the straight street scenario. Meanwhile, the characteristics of the PDFs change dramatically when the BS antenna height is half of the building's height under the forked road and crossroad scenarios. 2) We also discuss the effects of antenna height on the AS and the DS under the three typical scenarios, and conclude that the AS and the DS reach their maximum or minimum value when the antenna height is half of the building's height, except for the AS under the crossroad scenario.

Chapter 4: 2-D and 3-D Elevation Angle Model for Small Cell Environments

Two scatterer models are proposed for 2D and 3D small cell scenarios. The closed-form expressions of the PDFs are derived and verified. With the derived PDFs, the spatial correlations are discussed under various conditions.

Contributions: 1) The 2D ellipse scattering model and 3D ellipsoid model are proposed for small cell scenarios. 2) The closed-form expressions of the PDFs of the EAoD can be used to estimate the angle distribution in a small cell channel. 3) The results of the discussion about the spatial correlations indicate that the distance between a BS and an MS affect the spatial correlation more patently than the BS antenna height.

Chapter 5: Diffuse scattering in 3D Ray-Launching

The diffuse scattering effect on the millimeter wave is investigated under typical building structures through measurements. During the measurements, we find that the measurement data is inaccurate because of the multiple reflection rays. Among these rays, the second reflection ray (because the measured material is in the shape of a thin board) dominates the power in multiple reflection rays. Thus, an algorithm for deleting the effect of the second reflection ray. This chapter sheds light on how to integrate diffuse scattering into a ray launching (RL) model.

Contributions: 1) The mechanism of diffuse scattering in a millimeter wave and how to use it in the RL tool is introduced. 2) The scattering of a 40–50 GHz millimeter wave from typical building structures is measured. 3) An algorithm is proposed to deal with the measured data.

Chapter 6: Conclusions and Future Work

The concluding remarks, along with the directions for future work, are presented.

Chapter 2

Literature Review

Overview

This chapter introduces the topics of small cell channel modeling and millimeter-wave channel modeling. For an in-depth investigation of the small-cell and millimeter-wave channel models, the basic characteristics of a small cell and millimeter-wave need to be understood. Therefore, in this chapter, we first introduce a small cell and millimeter-wave, followed by the classic channel model. Finally, the small cell and millimeter-wave channel models are reviewed.

2.1 Reviews of small cell and millimeter-wave

In this section, the basic concepts and problems of a small cell and millimeter-wave are introduced.

2.1.1 Introduction of small cell

Although the capacity of a wireless network is growing significantly, this development cannot meet the future traffic demands, which have shown an exponential growth during the past years. Therefore, operators are trying to find new methods to increase the network capacity, with one of the most suitable approach being network densification. This approach increases the network capacity by deploying more cells through spatial reuse. However, the deployment of more

Fig. 2.1 Small cell BS.

macro-cellular BSs shows problems such as limitation of rooftop and high cost. Thus, a new approach of building smaller BSs has been proposed. [15].

According to [15], a cell is identified as a small cell if it satisfies the following requirements:

- The coverage of a small cell (usually 10m-200m) is much smaller than that of a macro cell. Thus, a macro cell can cover several small cells.

- They are deployed and managed by operators.

- They provide open access to all users.

- Compared to macrocells, their installation and maintenance costs are cheaper.

- They mainly provide data services, although they support voice services as well.

Small cell BSs are mainly deployed at hotspots such as a city centre, as shown in Fig. 2.1. A small cell mainly aims to provide localised coverage and capacity. The same interfaces as those of a macrocell BS make small cell BSs easily cooperate and integrate with macrocell BSs. Meanwhile, unlike macrocell BSs, which can only be deployed at specific locations, small cell BSs can be deployed at ideal locations [16]. For example,

- Outdoor: Deployed on street furniture such as trees, lamp posts, and building sites to provide service to users on the street or the lower floor of buildings.

- Indoor: Deployed in dense user and high-data-demand areas to provide service to users in buildings.

Since small cells can dramatically improve the network capacity, along with exhibiting low cost and flexible deployment, they are widely used by many operators. Some investigations have shown that more than half operators have already deployed or are deploying indoor small cells. The American Telephone and Telegraph Company announced that they will deploy over 40,000 outdoor small cells [17].

However, despite these advantages, the small cells technology also shows some challenges. For examples, the first one is the self-organization, it is a massive work for the huge number of small cells to accomplish the auto-configuration of basic radio and system parameters, the optimization of resource allocation and the recovery from node failures. The second one is the dense and unplanned deployment of small cells results in unpredictable interference patterns and a possibly patchy coverage. The third one is how to manage the interference between small cells and macro cells as well as that of small cells. Meanwhile, the high cost of the small cell wireless backhaul equipment also need to be considered [18].

2.1.2 Introduction of millimeter-wave

The fast growth of mobile data and wide use of network devices such as smartphones and laptops have prompted wireless operators to meet the global bandwidth demands. Nowadays, operators are trying their best to apply low-latency, high-quality multimedia services to users; however, the available carrier frequency spectrum from 700 MHz to 2.6 GHz has limited their products. Therefore, some new approaches, such as the millimeter wave, have been proposed [19].

A millimeter wave refers to the frequency spectrum ranging from 30 to 300 GHz, with its wavelength ranging between 1 and 10 mm. In practice, a radio signal suffers from attenuation caused by scattering, absorption, etc., when propagating through the atmosphere. The propagation characteristics of a millimeter wave are also affected by atmospheric oxygen, rain, fog, and humidity [20], as shown in Table 2.1.

Effect	Comments	Signal loss (dB/km)
Oxygen	Sea level	0.22
Humidity	$30°C$	1.8
Heavy Fog	$10°C$, $1gm/m^3$	3.2
Cloud Burst	$25mm/hr$ rain	10.7

Table 2.1 Signal loss through Atmosphere at 60GHz[21].

Table 2.1 illustrates that the signal loss caused by atmospheric oxygen is negligible. The effects of humidity and fog on signal are slightly higher than that of atmospheric oxygen. Moreover, cloud burst shows the maximum effect on the signal compared to other weather conditions.

Though the attenuation effect on a millimeter wave is significant, it has its own advantages that attract wireless operators, which are listed below:

- Large bandwidth: The bandwidth of millimeter wave is around 270 GHz, which is much greater than the previous bandwidth of wireless communication.

- Narrow-beam and small-scale antenna: An advantage of narrow-beam and small-scale antennas of a millimeter wave is the scalability of their deployment. Unlike low-frequency BSs,

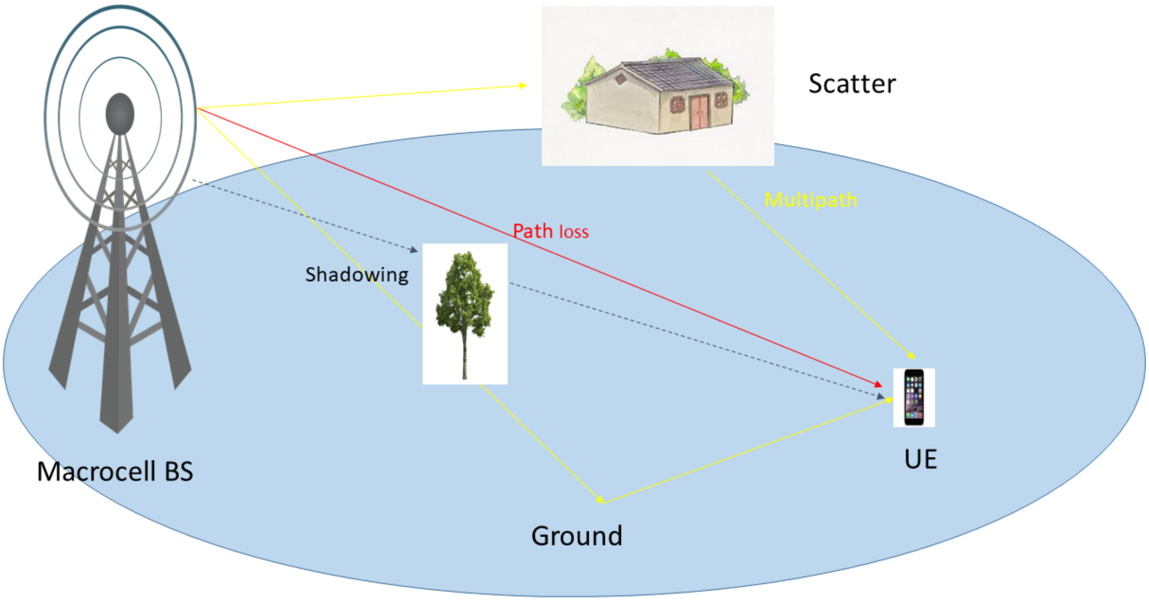

Fig. 2.2 Classic channel model.

millimeter-wave devices can be deployed at small specific locations such as trees and street lamps.

- Low-cost licensing: Without being licensed, a spectrum cannot be used for business purposes. One significant benefit of a millimeter wave is that its licensing cost is much lower than that of the microwave band.

2.2 Review of classic channel model

The research on a channel can be regarded as a research on what happens during a signal's propagation from the transmitter to the receiver, as shown in Fig. 2.2. Fig. 2.2 shows that a channel is determined from the distance between the transmitter antenna and receiver antenna, the propagation path of the signal, and the scatterers around the path. If we have a good knowledge of the channel, we can easily obtain the profile of the received signal from the transmitted signal. Generally, a channel model contains three main component loss, shadowing, and multipath, as shown in Fig. 2.2, the red line, the yellow line and the black dotted line represent the path loss, the shadowing and multipath respectively.

• Path loss: The reduction in power density (attenuation) of an electromagnetic wave as it propagates through space. Path loss is mainly depended on the wavelength of the transmission wave and the distance between the transmitter and the receiver. Commonly, path loss always decreases with the wavelength and increase with the distance.

• Shadowing: It is the result of the signal being blocked by large objects in the propagation path.

• Multipath: It is the result of the signal reaching the receiver antenna by two or more paths. It is caused by ionospheric reflection and refraction, and reflection from objects such as buildings and trees. The effects of multipath include constructive and destructive interference, and phase shifting of the signal.

A channel model can be classified in various ways. For examples, many channel models have been set up by measurements reported over the past decade. At the same time, channel models are also classified as time-varying (the channel characteristics change with time) versus time-invariant models (the channel characteristics do not change with time), and narrowband (source signal bandwidth is sufficiently narrow than the coherence bandwidth of the channel) versus wideband (source signal bandwidth is sufficiently larger than the coherence bandwidth of the channel) models [24]. Here, we classify the channel models by physical wave propagation and MIMO channel matrix, as shown in Fig. 2.3 [25]. Because our research focuses on the physical model, we will introduce the physical model in detail and briefly introduce the analytical model.

2.2.1 Physical channel models

Physical channel models focus on electromagnetic wave propagation, which is independent of the antenna configuration. They illustrate double-directional multipath propagation [26] between

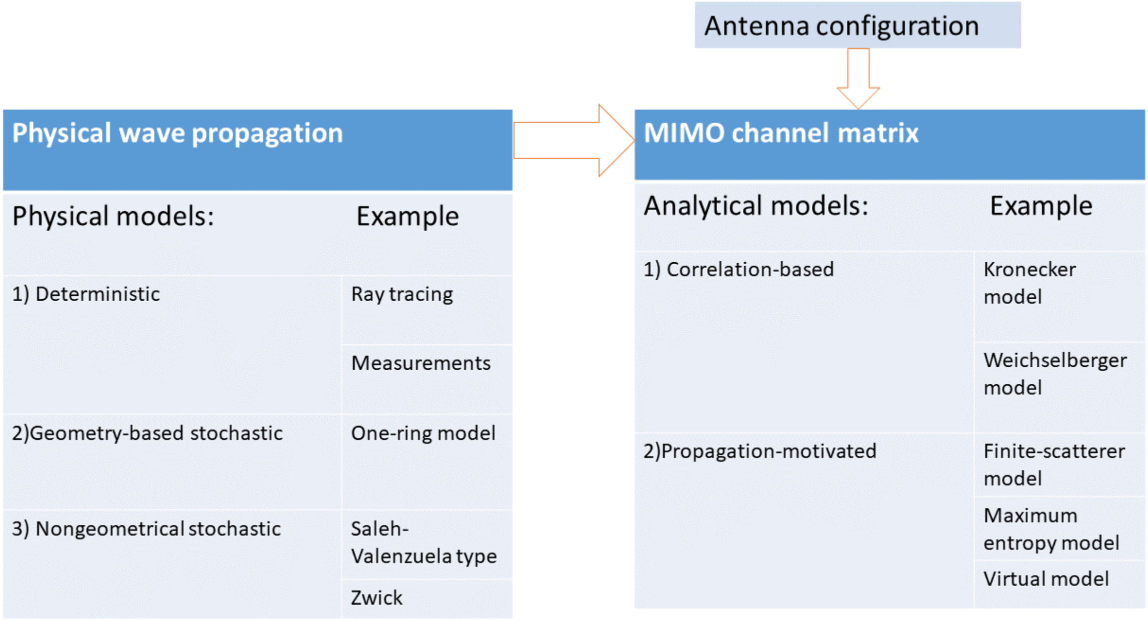

Physical wave propagation

Physical models:	Example
1) Deterministic	Ray tracing
	Measurements
2)Geometry-based stochastic	One-ring model
3) Nongeometrical stochastic	Saleh-Valenzuela type
	Zwick

MIMO channel matrix

Analytical models:	Example
1) Correlation-based	Kronecker model
	Weichselberger model
2)Propagation-motivated	Finite-scatterer model
	Maximum entropy model
	Virtual model

Fig. 2.3 Classification of channel model [25].

the transmit and receive antennas. In these models, wave propagation parameters, such as AoD and AoA, and complex amplitude of each multipath can be clearly obtained. Moreover, some sophisticated models show scenarios of scattering cluster and time variation [27]. Therefore, they can explicitly reproduce radio propagation. Physical channel models can be sub-divided into the following three types of models: deterministic models, geometry-based stochastic models (GBSMs), and non-geometrical stochastic models.

Deterministic models

Deterministic models characterize the physical propagation parameters in a completely deterministic manner. These models require data on the radio link between the transmitter and receiver, the electromagnetic properties of the environment, and geometric features. Buildings in this scene are regarded as flat polygons. They exhibit high accuracy for environments, and thus, are generally used to replace measurements when it is time in-sufficient to execute measurements or when particular cases, which are difficult to measure in practice.

One of the most common physical deterministic models is ray tracing (RT) model as shown

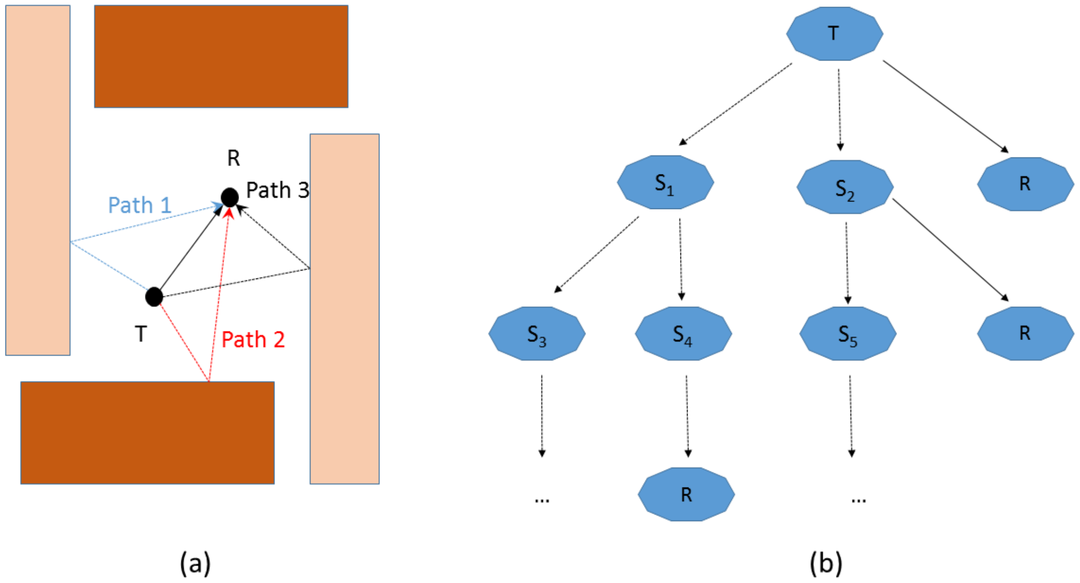

Fig. 2.4 Simple RT illustration: (a) propagation scenario; (b) visibility tree (first three layers shown)

in Fig. 2.4(a). where, T and R represent the transmitter and receiver, respectively. S_i in Fig. 2.4 (b), $i = 1,2,3,4,5$. represent different scatterers. Fig. 2.4(a) illustrates the simple RT mechanism: set a number that represents the maximum number of reflections or diffractions. Then, use a visibility tree (Fig. 2.4(b)) to trace the individual propagation. Fig. 2.4(b) shows a layered structure including nodes and branches. Each node in this tree indicates a corresponding object of the scenario (transmitter, building wall, corner, receiver, etc.), while each indicates the connection between two nodes is in line of sight (LoS). This tree structure can be regarded as a recursive manner: from transmitter to the next layer, and then, turn down through an LoS branch. One procedure ends once the branch arriving arrives at the receiver. Finally, all end when N_{max} is reached.

A representative example is shown in [28], where the authors first proposed a small scene which includes a diffraction wedge and two simple linear arrays, and then concluded that the capacity of this system decreased dramatically with one wedge and increased in the presence of more wedges.

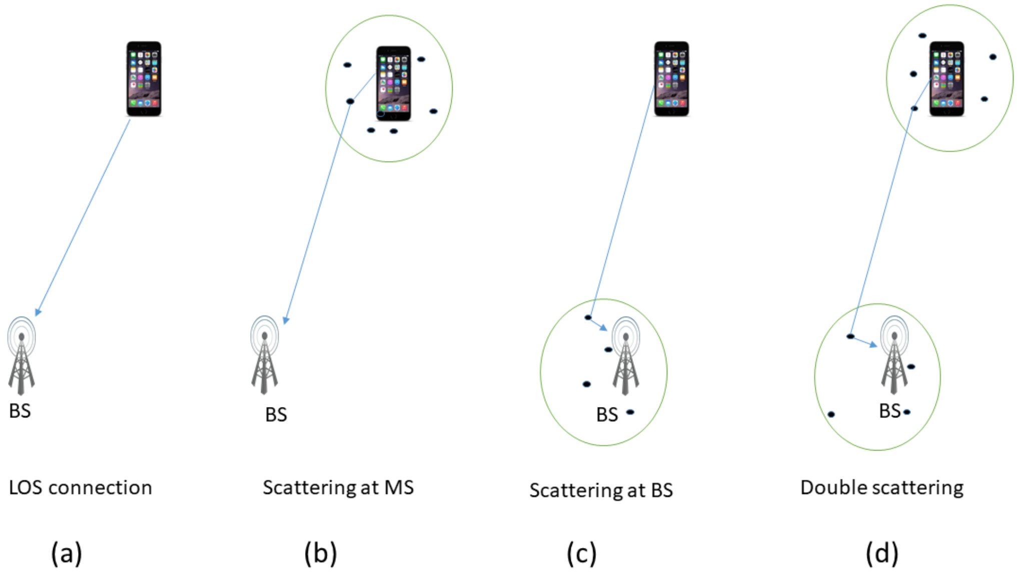

Fig. 2.5 GBSMs

Geometry-based stochastic physical models

The main difference between GBSMs and deterministic models is that the stochastic distribution of scattering around the transmitter and receiver is assumed while that in deterministic models is obtained from the database [29]. A GBSM is mainly determined by the location of scattering. Some typical GBSMs are shown in Fig. 2.5. Fig. 2.5 shows the four typical scattering distributions. Fig. 2.5(a) shows the straightforward way, which has no scatterers. Fig. 2.5(b) and Fig. 2.5(c) present examples in which the scatterers are distributed around the MS and BS, respectively. Fig. 2.5(d) shows the most complicated GBSM, where the scatterers are located at on both sides of the BS and the MS.

Non-geometrical based stochastic physical models

Non-geometrical stochastic physical models (NGBSMs) do not consider the geometry of a physical environment, but rather focus on the statistical data of the paths from the transmitter to receiver. An example is shown in [30], where the authors explored whether an NGBSM can capture the key features of an indoor channel. They concluded that it is difficult to assess the channel when ignoring its physical characteristics.

2.2.2 Analytical channel models

Unlike physical models, analytical channel models focus on the impulse response between the transmit and receive arrays, rather than wave propagation. Each impulse response is allocated to one matrix of the MIMO channel. These models are very useful for the synthesis of the MIMO matrix system and algorithm [31].

Analytical models can be divided into two types: correlation-based models and propagation-motived models. In correlation-based models, the MIMO channel matrix is investigated statistically according to the correlation between the matrix entries. An example is shown in [32], where the authors proposed joint spatial correlation properties on both transmitter and receiver in a novel analytical model. In propagation-motived models, the MIMO channel matrix is investigated according to the propagation parameters. A typical model is illustrated in [33], where a virtual channel model was proposed to represent the real channel.

After analysing these different types of channel models, we list the key features and main difference of the models in Table 2.2.

2.2.3 Standard channel models

As illustrated before, both the physical channel model and analytical model have their own features. To better utilize these models, some standardized models are developed, such as European cooperation in the field of scientific and technical research (COST) 259, WINNER channel models, IEEE 802.11n TGn model, spatial channel model (SCM) and etc..

COST 259 is the first physical model which took into account the relationship between the distance form the BS to MS, the angle spread, delay spread, and etc.. It contains 13 different environments (typical urban, open square, indoor office, and etc.) [34]. WINNER channel models adopted the GSCMs principle. They used the same generic structure to model all types of scenarios [35]. IEEE 802.11n is a NGBSM which was introduced for indoor environments.

	Key features	Main differences
Deterministic models	Aim at reproducing the actual physical radio propagation process. Physically meaningful, and potentially accurate.	Store the characteristics of geometric and electromagnetic in environment databases. The corresponding propagation process can be simulated through computer programs.
GBSMs	All information is inherent to the distribution of the scatterers. Many effects (small-scale fading, AoD, delay and etc.) are implicitly reproduced	An immediate relation to physical reality. Key parameters can be obtained by geometrical considerations.
NGBSMs	Do not consider the geometry of a physical environment.	Focus on statistical data of paths from transmitter to receiver.
Analytical models	Focus on the impulse response of the channel in an analytical or mathematical way.	Without consider the wave propagation. Suitable for synthesizing MIMO matrices.

Table 2.2 Key features of the different models

The statistic data in the model was obtained by some practice measurements [36].

In this chapter, we select the SCM for detailed description.

SCM was developed for evaluating different outdoor scenarios. In SCM, the wideband characteristics of the channel, which contains statistic channel parameters such as angular spread, power azimuth spectrum (PAS), and mean direction, are investigated. Meanwhile, the antenna configurations are also given in SCM.

SCM follows the below mechanism:

- It was developed by 3GPP/3GPP2 for estimating outdoor MIMO environments. The centre frequency and bandwidth are set to 2 GHz and 5 MHz, respectively. SCM mainly contains two parts: calibration model and simulation model.

- A calibration model aims to ensure the correctness of the simulation, and can be regarded as either an NGBSM (where parameters such as PAS, DS, and AS are given) or an analytical model (where various antenna configurations are).

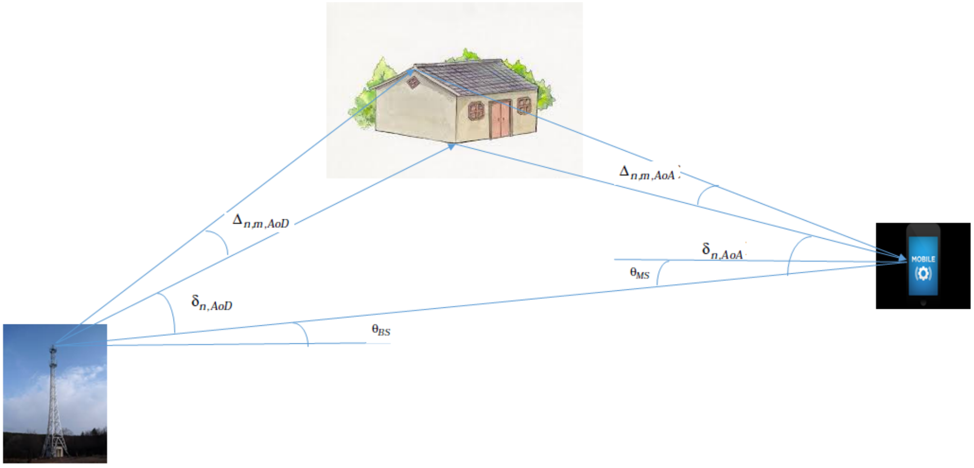

Fig. 2.6 SCM: a single link

- A simulation model describes the following three scenarios: urban macrocell, suburban marcocell, and urban microcell. The model structure and simulation methodology for these three scenarios in an SCM are the same. However, the parameters such as AoA, angular of departure, and DS differ.

In SCM, six main paths are fixed in each scenario and twenty subpaths are allocated in each main path. One single path is illustrated in Fig. 2.6, where the MS is located randomly and the movement direction of the MS as well as the orientation of the antenna array are also chosen randomly. On one hand, the main contribution of SCM is the use of the subpath concept. Because the scatterers always have a volume which can be represented as the house in Fig. 2.6, only one path cannot truly determine the characteristic of this link. Therefore, two angles $\Delta_{N,M,AoD}$ (the AoD of the M subpath in N main path) and $\Delta_{N,M,AoA}$ (the AoA of the M subpath in N main path) are introduced to represent the AS. An SCM assumes that there are 20 sub-paths each in $\Delta_{N,M,AoD}$ and $\Delta_{N,M,AoA}$, which have slightly different directions. On the other hand, the movement of the MS will affect the variation in the impulse response that causes different phase shifts of the sub-paths [37].

2.3 Review of small cell channel models

Although some previous MIMO channel models can be used to model small cell channel models, some new challenges exist in small cell channel modeling.

One distinct challenge is how to model the multipath links at the system level. In [38], the authors indicated that existing theoretical research on MIMO channel models focuses on simple narrowband fading channel models such as Rician model and Rayleigh model. Obviously, these models are too simplified and mainly emphasise on point-to point links. However, with the introduction of small cells, the structure of the entire wireless network has become more complicated. Thus, a small cell MIMO channel model should account for not only the properties of individual links (point-to-point links) but also the variations and collections of multiple links at the system level [39].

Over the past decade, small cell channel models have been extensively studied. In [40], the authors provided the path loss data by using millimeter-wave measurement under small cell scenarios. Two providers (Nokia and Samsung) used the data in their small cell channel modeling. In [41], a 3-D GBSM was proposed in the microcell environment by using the data measured at 10 GHz. In [42], a ray-based model for dual-polarised channels was developed and verified by the measurement. In [43], a 3D ray tracing framework was used to research the channel at 2.6GHz. The authors conclude that the delay spread is highly depended on the environments, and angle spread at transmitter is highly related to the antenna pattern. In [44], a measurement was measured at 2.6GHz in a typical urban scenario, and the authors conclude that the the polarization has not effect on the distribution of the EAoA. In [45], a measurement was conducted at 3.7GHz with the small cell base station height is below 10m. They found that the channel characteristics in 3.7GHz show higher average cell throughputs than that of conventional channel.

As we can see from Table 2.3, almost all previous studies on small cell channel modeling were investigated through measurement. This is mainly because of the short coverage of the small cells, which helped the researchers perform the measurements. However, with the increasing cost and demand of accuracy, it is impossible to perform the measurement under all scenarios. Therefore, a theoretical research of small cell channel models is also required.

Type	Research Status	Key features
Ray-based models	Little literatures	They are inaccuracy, but time efficient. Sometimes need verified by measurement.
Measurement models	More literatures but not too much	They are accuracy, but time consuming. Suitable for complex scenario

Table 2.3 Key features of the small cell models

2.4 Review of millimeter-wave channel models

The characteristics of a channel in a millimeter-wave band show several critical differences from those of the channel in the low-frequency band:

- According to the Friis transmission equation, the small wavelength of the millimeter wave causes a very huge propagation loss. Therefore, highly directional transmitter and receiver antennas need to be used to compensate for the loss. Consequently, the channel model should consider the relative angle from the transmit and receive antennas. Meanwhile, the model should suitable for all types of antenna technologies.

- As indicated in [47, 48], a dramatic feature of a millimeter-wave is its quasi-optical property: the diffraction effect on a millimeter-wave can be ignored and most rays' transmission type between the transmitter and receiver is LoS.

- Basically, each propagation path should have only a single ray if the reflection path is ideally in a common communication system. However, owing to the small wavelength of a millimeter wave, each scattering ray may contain several rays due to diffuse scattering [48], and consequently, diffuse scattering should be accounted for when modelling a millimeter-wave channel model.

- Another characteristic that should be considered in millimeter-wave channel modeling is polarization. The evidence given by [49] shows that the power degradation for a millimeter-wave system due to polarization can be as high as around 15 dB.

Several studies have been conducted on millimeter-wave channel models. In [50], the authors proposed a channel model for indoor 60 GHz propagation through a statistical method and proposed a general mathematical structure of the model. The main contribution of this paper is the precise space-time characteristic of the indoor channel model. In [51], it was certificated that the millimeter-wave frequencies are much suitable for future wireless communication. Meanwhile, the authors used the RT method to realise millimeter-wave channel modeling.

In the first approach, the channel model was obtained using a statistical method and parameters such as AoD, AoA, and delay profile are defined. However, it is sometimes difficult to obtain the best consensus parameters to model the channel under a specific environment. In the second approach, the channel model is obtained using the RL method, which is in accordance with the propagation of electromagnetic waves. This method can regenerate the channel model more naturally, but is much more complex.

Owing to the low precision of the statistical method and high complexity of the ray-based method, extensive research has been conducted to create channel models which have high precision and low complexity. Reference [52] proposed a channel model which exhibits the characteristics of both statistical method and ray-based method. The main contribution of this model is the use of geometry statistics data such as the distribution of scatterers (buildings, trees, etc.), reflection loss, and distribution of time of arrival as input data. Finally, it is proved that the proposed channel model matches the existing measurement results well.

In [53], a ray tracing method was used to analyze the impact of human blockage on wireless communications under 60 GHz. In [54], the authors investigated the human blockage at 11, 16, 28 and 32 GHz by measurements. They concluded that the losses caused by human blockage do not show obvious increasing with the frequency increases. In [55], some key channel characteristics like channel gain, K-factor and DS were investigated at 13-17 GHz by measurement. In [56], the authors conducted channel measurements with large antenna arrays in an indoor office scenario, and they showed that the massive MIMO effects should be taken into account for millimeter wave channel models. In [57], a statistical millimeter wave channel model was developed to address the multipath parameters for omni-directional and directional channels. In [58], the authors applied the angular averaged power delay profile method to data of a millimeter wave channel measurement, and estimated the angular stationarity region of the channels. In [59–61], several measurements at 28, 38, 60 and 73 GHz were conducted in campus, BS-MS access and vehicular scenarios. In [62], the authors conducted the millimeter-wave measurements at four different bands to compare the propagation characteristics such as power azimuth profile, AS and DS. The results showed that the propagation characteristics have similar proprieties for different bands. After analysing these different types of millimeter-wave channel models, we list the key features of the models in Table 2.4.

	Key features
Statistical models	The propagation parameters are defined. However, they are difficult to obtain the best consensus parameters under a specific scenarios
Ray-base models	They are in accordance with the propagation of electromagnetic waves. They can regenerate the channel model more naturally, but are much more complex.
Combined methods	High precision and low complexity.
Measurement models	The most precise methods, but have high cost and low efficiency.

Table 2.4 Key features of the millimeter wave channel models

At present, the millimeter-wave technology is widely used for cellular backhaul, satellite communication, and local area networks. However, how to apply millimeter-wave bands for a longer range is another serious problem due to the properties of millimeter-wave propagation, such as high atmospheric attenuation, especially rain attenuation and Doppler spreads. Owing to these limitations, advanced technology needs to be developed for a stable communication across NLOS and over a longer range [63]. Two crucial technologies have been proposed for this purpose: CMOS RF, which attempts to reduce the cost of millimeter-wave devices, and small cellular network, which will be used for future wireless communication. In many fields, an area of 100-200 meters is enough for a cellular network suitable for a millimeter-wave [64]. Thus, we conclude that the millimeter-wave channel model perfectly fits a small cell channel model.

2.5 Summary

This chapter consists of four major review sections: small cell and millimeter-wave, classic channel models, small-cell channel models, and millimeter-wave channel models.

In the small cell and millimeter-wave review, the basic concepts of small cells and millimeter wave have been introduced. A small cell shows features similar to those of a macrocell, but has shorter coverage, lower price, and lower power. Millimeter wave refers to the 30-300 GHz, and always suffers from larger attenuation than the ferquency below 4GHz. Some key features of small cells and millimeter wave are also given in this section.

In the review of classic channel model, we first introduce the three main components of a channel model: path loss, shadowing, and multipath. Then, we have classified the channel models into physical channel models and analytical channel models. Because this study focuses on the physical model, we introduce the physical model in detail and only briefly introduce the analytical model. Finally, some standard channel models such as COST 259, WINNER channel model, SCM are introduced.

In the review of a small cell channel model, the challenges of small cell channel modeling are given. Some examples of the measurement of the small cell channel are illustrated. The reason why we need to model the small cell channel theoretically is shown in this section.

In the review of the millimeter-wave channel model, the difference between a millimeter-wave channel model and a low-frequency channel model is first given. Then, some relative studies are introduced and we conclude that the millimeter-wave channel model perfectly fits a small-cell channel model.

Chapter 3

The Impact of Antenna Height on 3-D small cell Channel: a Ray Launching Based Analysis

Overview

3-D MIMO is one of the enabling technologies for 4G and 5G mobile communications. As the elevation angle in the 3-D MIMO channel model might vary against the height of the BS antenna, it should be considered in channel modeling. In this chapter, the impact of antenna height on the channel characteristics of the 3-D MIMO channel is investigated by using the intelligent ray launching algorithm (IRLA). Three typical street scenarios, i.e., the straight street, the forked road, and the crossroad, are selected as benchmarks. The joint and marginal PDFs of both the EAoD and the EAoA are obtained through simulations. Moreover, the elevation AS and the elevation DS under various antenna heights are jointly discussed. Simulation results show that the characteristics of the PDFs of EAoD will vary under different street scenarios. It is observed that in order to obtain the maximum or minimum value of the AS and the DS, the BS antenna should be deployed at half of the building's height under the three typical street scenarios.

3.1 Introduction

One common feature of the research works on future wireless communication technologies is the pursuit of high spectral efficiency while MSs access the network. Multi-user (MU) MIMO technology is expected to play a key role to achieve high spectral efficiency [65]. To thoroughly investigate MIMO, it is essential to have a good understanding of radio-propagation characteristics of transmission path between the BS and the MS [66]. Several models are proposed to describe the radio channel [66–68]. In [67] and [68], the authors analyzed the channel characteristics by assuming the scatters are located uniformly within a circle or an ellipse. In [69], the authors argued that stochastic geometry and random graph theory are indispensable tools for the analysis of wireless networks. For the conventional study on channel model, linear antenna arrays were employed in the horizontal direction [70–72]. This assumption is valid since the distance between the MS and the BS is much larger than the distance between the height of the BS antenna and the scatterers around the MS [73].

However, considering 3-D distributed MSs, a better coverage and capacity can be achieved by using a 3-D antenna array [74]. Under this condition, the EAoD and EAoA which significantly affect the performance of MU-MIMO should be considered for channel modeling. The original EAoD and EAoA model was proposed in [75]. In 1990, a measurement in Tokyo based on 900 MHz observed that the distribution of elevation angle is extremely close to be Gaussian [76]. In 2002, the PDF of the EAoD for multipath at the BS was derived by assuming that the scattering objects were located uniformly within a circle around the MS [77]. Then, more research works started to appear over 10 years later. In [78], the SCM was extended to 3-D by considering the elevation angle at the MS. In [79], a 3-D scattering model was generalized for the macrocell environment with an MS located at the center of a 3-D scattering semispheroid and a BS employing a directional antenna which is located outside of the semispheroid. Recently, the scattering behavior was studied in [80]. Some other works focusing on the elevation angle in different propagation environments can be found in [81, 82]. In [81], a new expression, which directly relates the PDF of the elevation angle, was proposed to the power spectral density of the received signal. In [82], the authors applied a novel technique for measuring the angular distribution in different environments. Although previous works have analyzed the distribution of the EAoD and the EAoA, the impact of antenna height on the EAoD and the EAoA has not been considered.

Ultra-dense small cells, with various antenna heights, are widely investigated in 5G networks. Due to small coverage areas, the impact of antenna height on parameters of wireless propagation, especially the EAoD and the EAoA, becomes significant. Previous work indicated that the heights of the antennas at both the BS and the MS impact on the distribution of EAoD and EAoA significantly [83]. However, they did not consider how the antenna height would affect the distribution of elevation angle.

The main contributions of this chapter are as follows. Firstly, the EAoD and the EAoA are characterized under typical scenarios against heights of antennas. Secondly, the PDFs of EAoD and EAoA are derived in closed-forms under each scenario. From derived PDFs, we observe that the PDFs of EAoD and EAoA are almost linearly correlated with the antenna height under the straight street scenario. Meanwhile, the characteristics of PDFs change dramatically when the BS antenna height is half of the building's height under the forked road and crossroad scenarios. Finally, the effects of antenna height on the AS and the DS under the three typical scenarios are also discussed. We conclude that the AS and the DS reach their maximum or minimum value when the antenna height is half of the building's height, except the AS under the crossroad scenario.

This chapter is organized as follows: In Section 3.2, we briefly introduce the IRLA and the experiment scenarios. In Section 3.3, we derive the PDFs of EAoD and EAoA under experiment scenarios through simulations. Meanwhile, the AS and DS are also analyzed. Then, some discussions are drawn in Section 3.4. Finally, the conclusions are given in Section 3.5.

3.2 Methods and Numerical Results

3.2.1 Intelligent Ray Launching Algorithm (IRLA)

Radio wave propagation prediction modeling is critical in wireless network planning and optimization [84]. Types of propagation models have been presented in decades which can be classified as empirical models and deterministic models [85–87]. On the one hand, the channel characteristics in empirical models are determined by empirical factors, like the carrier frequency and the distance between the BS and the MS. These models are time-efficient but with lower accuracy. On other hand, deterministic models mainly consider the environmental information, such as the position and the reflection factor of the buildings. Thus, they are time consuming, but with higher accuracy [88]. The IRLA in our research can be categorized as a deterministic approach. The IRLA is used to compute all the possible reflections and diffractions of the emitting rays from the BS. Once the rays undergo reflections or diffractions, the additional loss will be added to the corresponding signal strength [89].

In [90], the authors originally presented the IRLA model, which relays on the cubic data obtained from discretization of the environment. The building walls, ground, trees and etc. can be regarded as a cube element. Each cube is associated with a set of information. Then the authors proposed and implemented the parallel IRLA based on parallel object-oriented programming in C++ [91]. The IRLA contains three main components: Light-Of-Sight (LOS) , Vertical diffraction (VD) and Horizontal Diffraction and Reflection (HDR) . The LOS component is used to calculate the path which is visible to emitter. VD component is responsible for finding the roof-top diffractions rays. HDR component is the most complicated part which launches a complete set of combination of diffraction and reflection rays. In [92], the authors implemented the angular dispersion of ray launching to improve its accuracy. Moreover, the model was extended to indoor scenarios in [93] and the combination with other methods was given in [94, 95]. The correction of the IRLA model is justified in [93] and [96–98]. A measurement test in [93] showed the indoor IRLA model is promising with accurate results and time saving. Meanwhile, the accuracy of the model under indoor-to-outdoor scenario and outdoor-to-indoor scenario was validated in measurements [96, 97]. Recently, analysis and comparison between the simulation results and measurements showed that the ray-launching methods are efficient and accurate for massive MIMO channel modelling [98].

3.2.2 Numerical results

The simulation scenario is part of the center of Paris, as shown in Fig. 3.1. The size of the area is $500m \times 300m$, and the average building height is approximately $21m$ [99]. We configure the transmit power of the BS as $0dBm$ and the carrier frequency as $2.4GHz$ (these two values can be set as any reasonable values at low frequency). For sake of convenience, we regard there are 4 omnidirectional antennas arranged in horizontal plane in the BS. The maximum reflection and diffraction numbers are 3 and 7, respectively. The parameters are listed in Table 3.1.

Size of area	$500m \times 300m$
Average buildings height	$21m$
BS power	$0dBm$
Carrier frequency	$2.4GHz$
BS Antenna type	Omnidirection 4
Max reflection number	3
Max diffraction number	7
Max number of rays	700,000

Table 3.1 Parameter settings of the experimental scenarios.

Fig. 3.1 illustrates that there are three typical street scenarios: straight street (red solid rectangular area), forked road (black dashed rectangular area), and crossroad (dark red dotted rectangular area) [100]. These three typical scenarios are displayed in Fig. 3.2 and the parameters for each scenario are listed in Table 3.2. During simulations, h is the height of the BS, and n is the index of MSs from 1 to 100,000, which means 100,000 receivers are uniformly distributed around the BS in total. We deployed the BS at $(0,0,h)$ and the receivers at (xn, yn, zn) in the global coordinate system. We regard the angles above the antenna height as negative degree $(< 0^0)$, and the angles below the antenna height as positive degree $(< 0^0)$. For simplify, we have not considered the line-of-sight component.

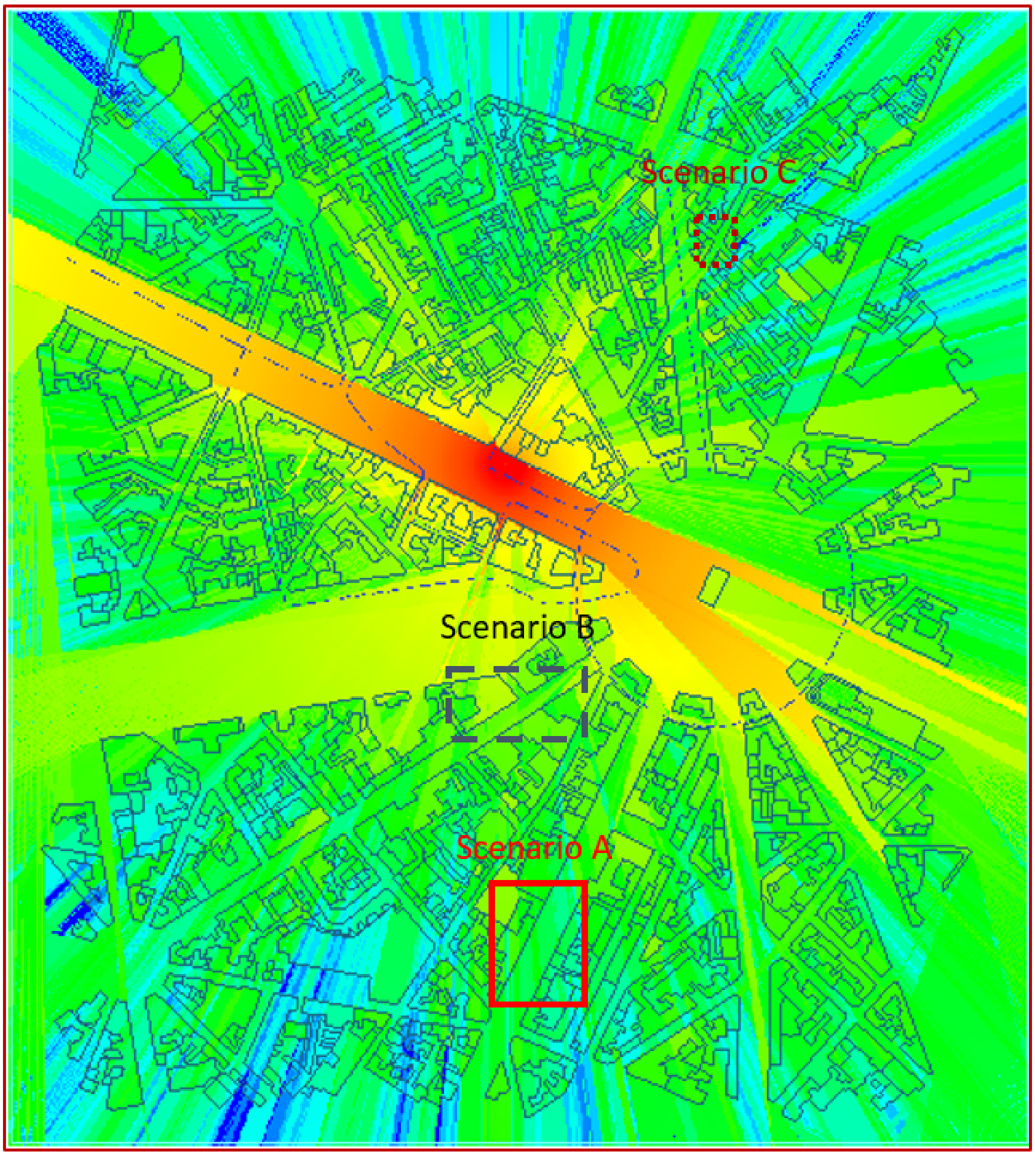

Fig. 3.1 Part of the center of Paris [plotting scale: 1:2500](the red rectangular area, the black rectangular area, and the dark red rectangular area represent one of the straight streets, forked roads, and crossroads, respectively) [99].

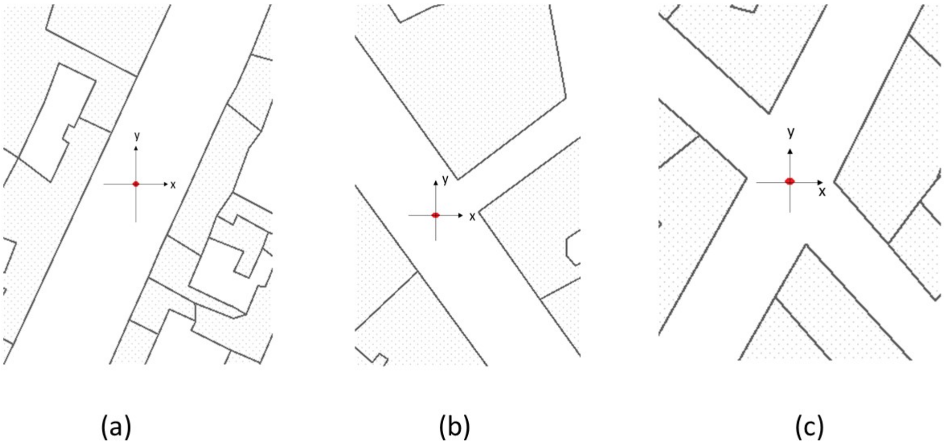

Fig. 3.2 Three typical scenarios: (a) description of the straight street; (b) description of the forked road; and (c) description of the crossroad.

	Straight street	Forked road	Crossroad
Average buildings height	$20m$	$25m$	$22m$
Length of wide street	$80m$	$80m$	$40m$
Width of wide street	$20m$	$20m$	$20m$
Length of narrow street	$0m$	$40m$	$40m$
Width of narrow street	$0m$	$12m$	$12m$

Table 3.2 Parameters of the three scenarios.

3.3 Results

3.3.1 Scenario A: Straight Street in the Center of Paris

Under the straight street in Fig. 3.2(a), the PDFs of EAoD and EAoA are investigated firstly. Due to reflection and diffraction during the signal transmission, each receiver can obtain multiple rays with different path losses, EAoDs, and EAoAs. The PDFs of EAoD and EAoA can then be calculated after adding the weighting value (path loss).

Two simulation results (antenna heights at 8m and 12 m) are indicated in Fig. 3.3. The Figures indicate that the PDF values of both the EAoD and EAoA around 0 radians are obviously greater than the values away from 0 degree, and the sub-curves at the negative and positive

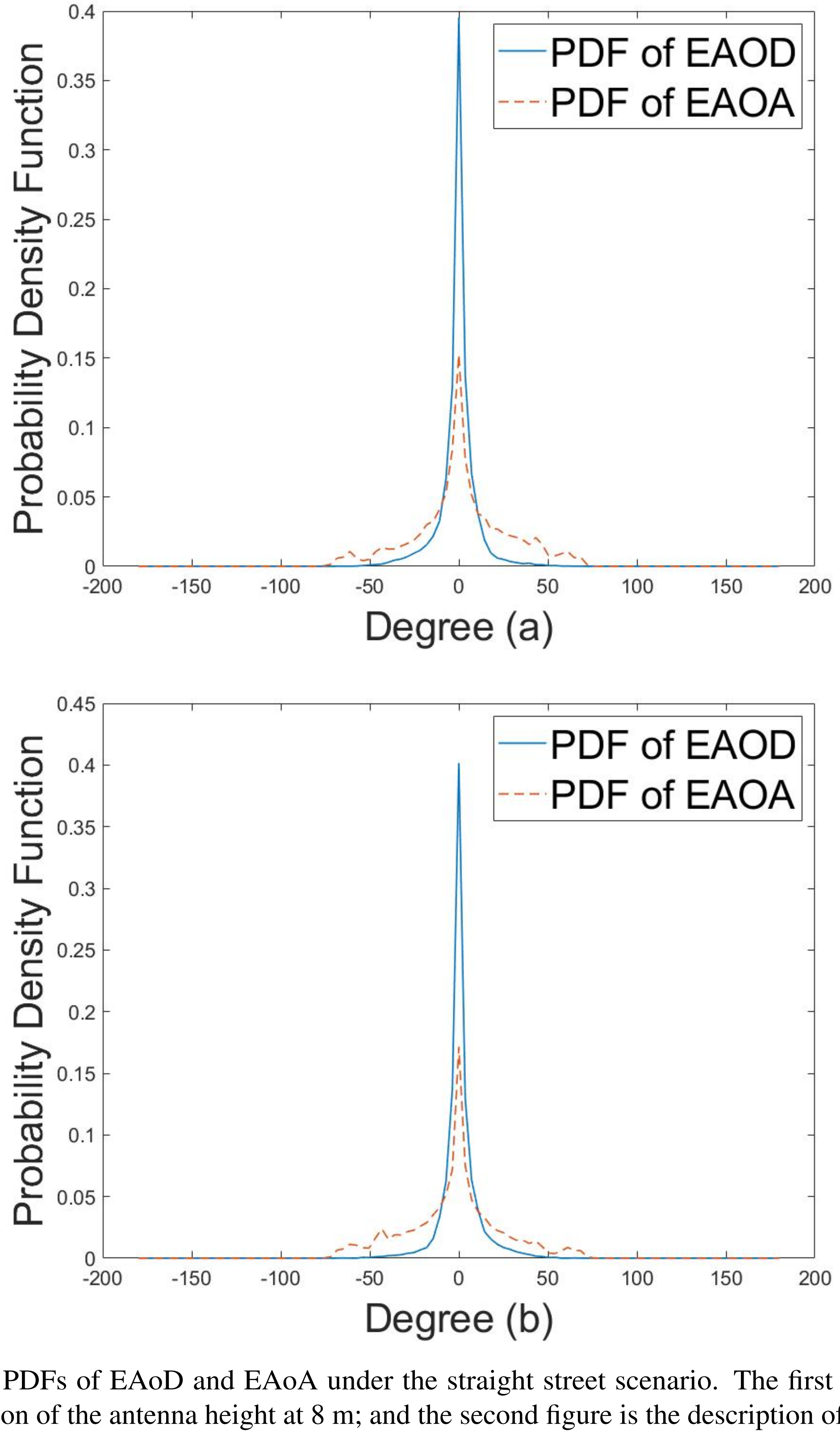

Fig. 3.3 PDFs of EAoD and EAoA under the straight street scenario. The first figure is the description of the antenna height at 8 m; and the second figure is the description of the antenna height at 12 m.

are asymmetrical, which have been verified in [82]. The author observed that a double-sided exponential function is more suitable for the PDF of elevation angles which can be represented as:

$$f_{EAoD}(x) = \begin{cases} \lambda_{1EAoD} \exp(-\lambda_{1EAoD}), & x < 0 \\ \lambda_{2EAoD} \exp(-\lambda_{2EAoD}), & x > 0 \end{cases} \tag{3.1}$$

$$f_{EAoA}(x) = \begin{cases} \lambda_{1EAoA} \exp(-\lambda_{1EAoA}), & x < 0 \\ \lambda_{2EAoA} \exp(-\lambda_{2EAoA}), & x > 0 \end{cases} \tag{3.2}$$

Here, the unit of x is degree. λ_{1EAoD}, λ_{2EAoD}, λ_{1EAoA} and λ_{2EAoA} are the rate parameters of these double-sided exponential functions. Logarithm fitting the PDFs of EAoD and EAoA (for example:$\lambda'_{1EAoD} = -10 \times \log_{10}(\mathrm{e}) \times \lambda_{1EAoD}$), we can finally obtain the values of λ'_{1EAoD}, λ'_{2EAoD}, λ'_{1EAoA} and λ'_{2EAoA}. In Fig. 3.3:$\lambda'_{1EAoD} = 26.83$, $\lambda'_{2EAoD} = -36.48$, $\lambda'_{1EAoA} = 16.43$ and $\lambda'_{2EAoA} = -15.69$. Obviously, the λ' will be different with various antenna heights. In Fig. 3.4, the λ' with various antenna heights (4–18 m) are listed. This illustrates that the logarithm exponent value is almost linearly correlated with the antenna height. Then, we can derive that: $\lambda'_{1EAoD} = 1.64 \times m + 14.35$, $\lambda'_{2EAoD} = 1.60 \times m - 48.83$, $\lambda'_{1EAoA} = -0.63 \times m + 22.84$ and $\lambda'_{2EAoA} = -0.76 \times m - 9.55$, where m is the antenna height whose unit is meter. As we can see from Fig. 3.4, the logarithm exponent values λ'_{1EAoD} and λ'_{2EAoD} (as shown in Equation (1)))) linearly increase with the antenna height growing, and the exponent values λ'_{1EAoA} and λ'_{2EAoA}'2EAoA (as shown in equation (2)) linearly decrease with the antenna height growing.

Finally, the PDFs of EAoD and EAoA related to antenna height can be represented as:

$$f_{EAoD}(x) = \begin{cases} -(0.38m + 3.30) \exp(0.38m + 3.30), & x < 0 \\ -(0.37m - 11.24) \exp(0.37m - 11.24), & x > 0 \end{cases} \tag{3.3}$$

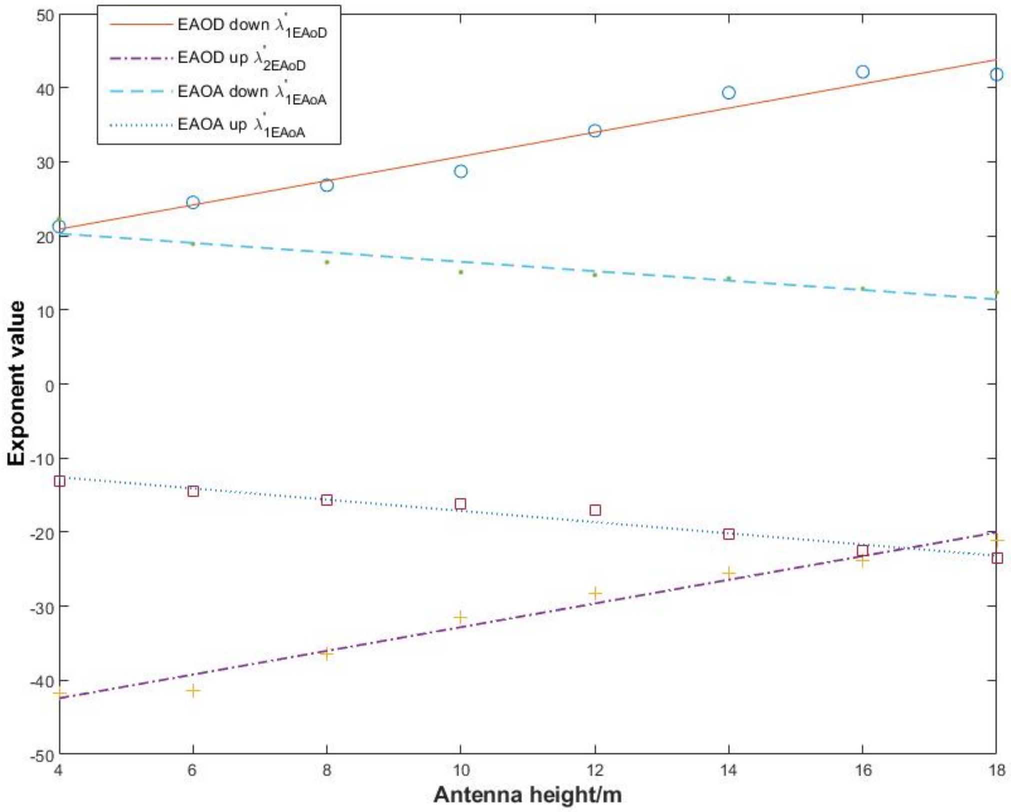

Fig. 3.4 The statistic results of logarithm exponent values under straight street scenario with various antenna heights (4 m, 6 m, 8 m, 10 m, 12 m, 14 m,16 m, and 18 m), the EAoD down, EAoD up, EAoA down, and EAoA up represent $\lambda^{'}_{1EAoD}$, $\lambda^{'}_{2EAoD}$, $\lambda^{'}_{1EAoA}$ and $\lambda^{'}_{2EAoA}$ respectively.

$$f_{EAoA}(x) = \begin{cases} -(-0.15m+5.26)\exp(-0.15m+5.26), & x<0 \\ -(-0.18m-2.20)\exp(-0.18m-2.20), & x>0 \end{cases} \tag{3.4}$$

Using the PDFs, the AS and the DS, which represent the elevation angle dispersion and the time dispersion of multipath components respectively, can be evaluated [77].

$$\sigma_{AS} = \sqrt{\frac{\sum_{i=0}^{L-1} P_i \theta_i^2}{\sum_{i=0}^{L-1} P_i} - (\frac{\sum_{i=0}^{L-1} P_i \theta_i}{\sum_{i=0}^{L-1} P_i})^2} \tag{3.5}$$

$$\sigma_{DS} = \sqrt{\frac{\sum_{i=0}^{L-1} P_i \tau_i^2}{\sum_{i=0}^{L-1} P_i} - (\frac{\sum_{i=0}^{L-1} P_i \tau_i}{\sum_{i=0}^{L-1} P_i})^2} \tag{3.6}$$

where, P_i is the power of ith ray, θ_i and τ_i are the angle and delay of ith ray. The statistic results of the AS and the DS are represented in Fig. 3.5 and Fig. 3.6, respectively.

Fig. 3.5 indicates that the value of the AS of EAoD is smaller than that of EAoA, and the variation range of the AS of EAoD is also smaller. The AS reaches its maximum value when the antenna height (10 m) is half of the building's height. Fig. 3.6 exhibits that the value of the DS is nearly unchangeable when the antenna height is around half of the buildings height and increases conspicuously when the antenna is near the bottom or the top of the buildings. By using the linear least square regression, we can obtain the correlation of the AS and DS with antenna height:

$$\sigma_{AS,EAoD} = \begin{cases} 0.1m+9.4, & m \leq 10 \\ -0.11m+11.5, & 10 < m \leq 20 \end{cases} \tag{3.7}$$

$$\sigma_{AS,EAoA} = \begin{cases} 0.383m+23.07, & m \leq 10 \\ -0.4625m+31.525, & 10 < m \leq 20 \end{cases} \tag{3.8}$$

$$\sigma_{DS} = \begin{cases} -2.905m+53.74, & m \leq 8 \\ 30.5, & 8 < m \leq 12 \\ 2.3667m+2.1, & 12 < m \leq 20 \end{cases} \tag{3.9}$$

where m is the antenna height. $\sigma_{AS,EAoD}$, $\sigma_{AS,EAoA}$ and σ_{DS} are the AS of EAoD, EAoA, and the DS, respectively.

3.3.2 Scenario B: Forked Road in the Center of Paris

Then, by using the same research steps in Section 3.3.1, we investigate the PDFs of EAoD and EAoA under the forked road scenario, as shown in Fig. 3.2(b). The simulation results when the antenna is located at 8 m and 12 m are indicated in Fig.3.7 .

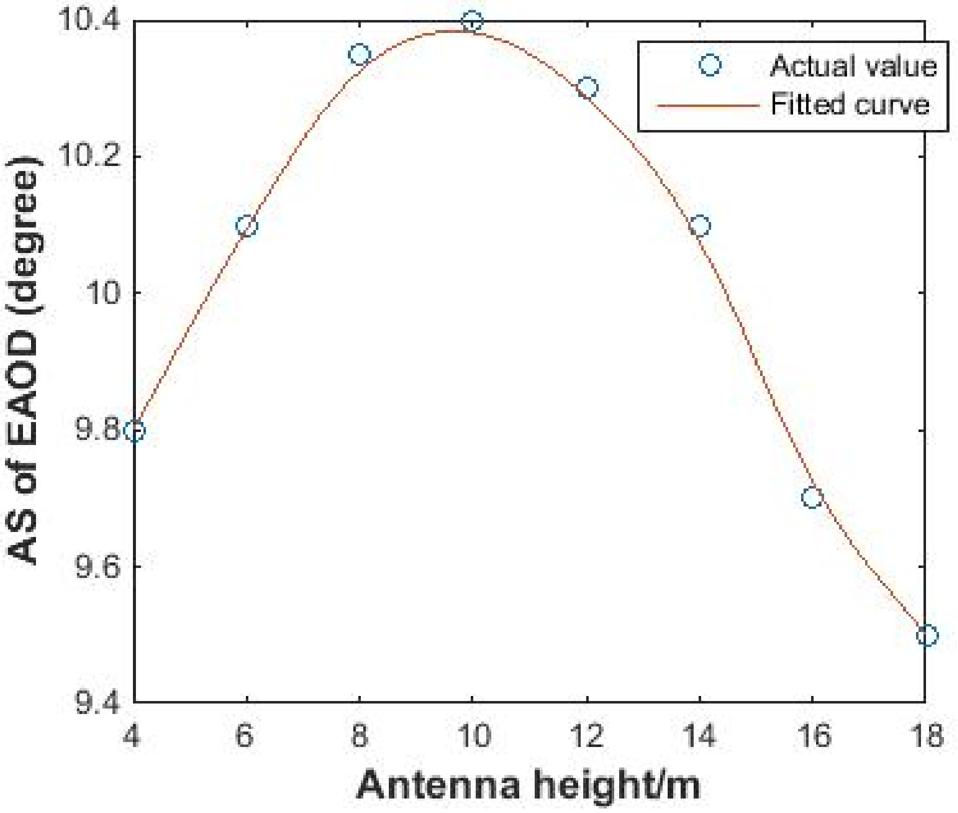

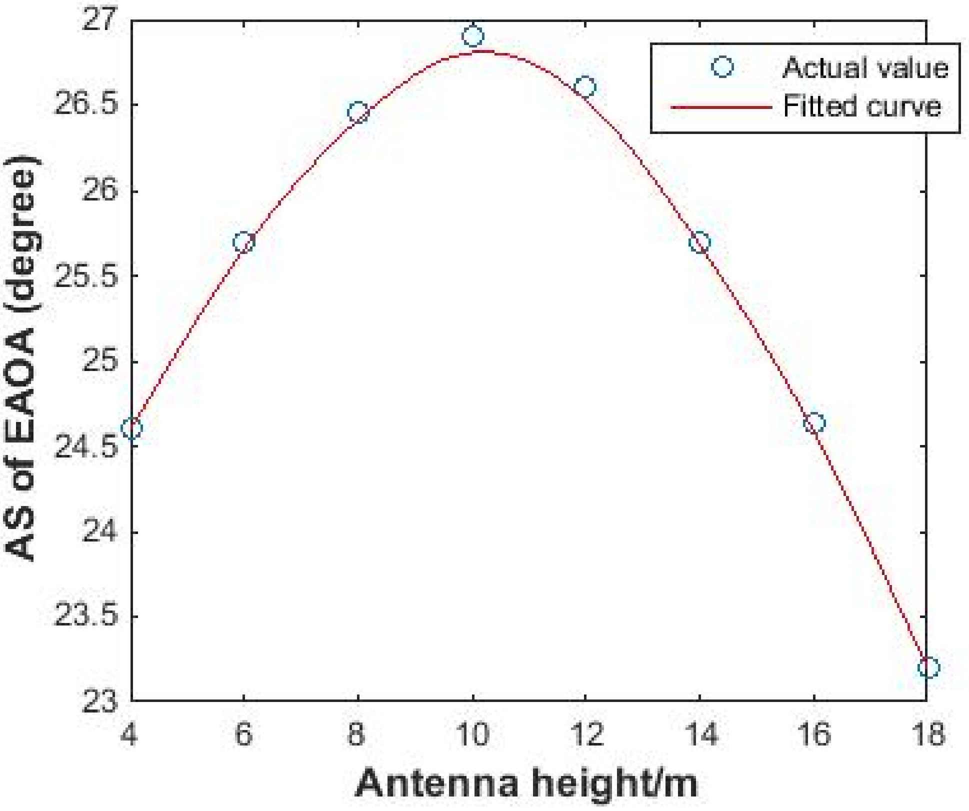

Fig. 3.5 The AS under the straight street scenario with various antenna heights (4 m, 6 m, 8 m, 10 m, 12 m, 14 m, 16 m, and 18 m). The first figure is the description of the AS of EAoD; and the second figure is the description of the AS of EAoA.

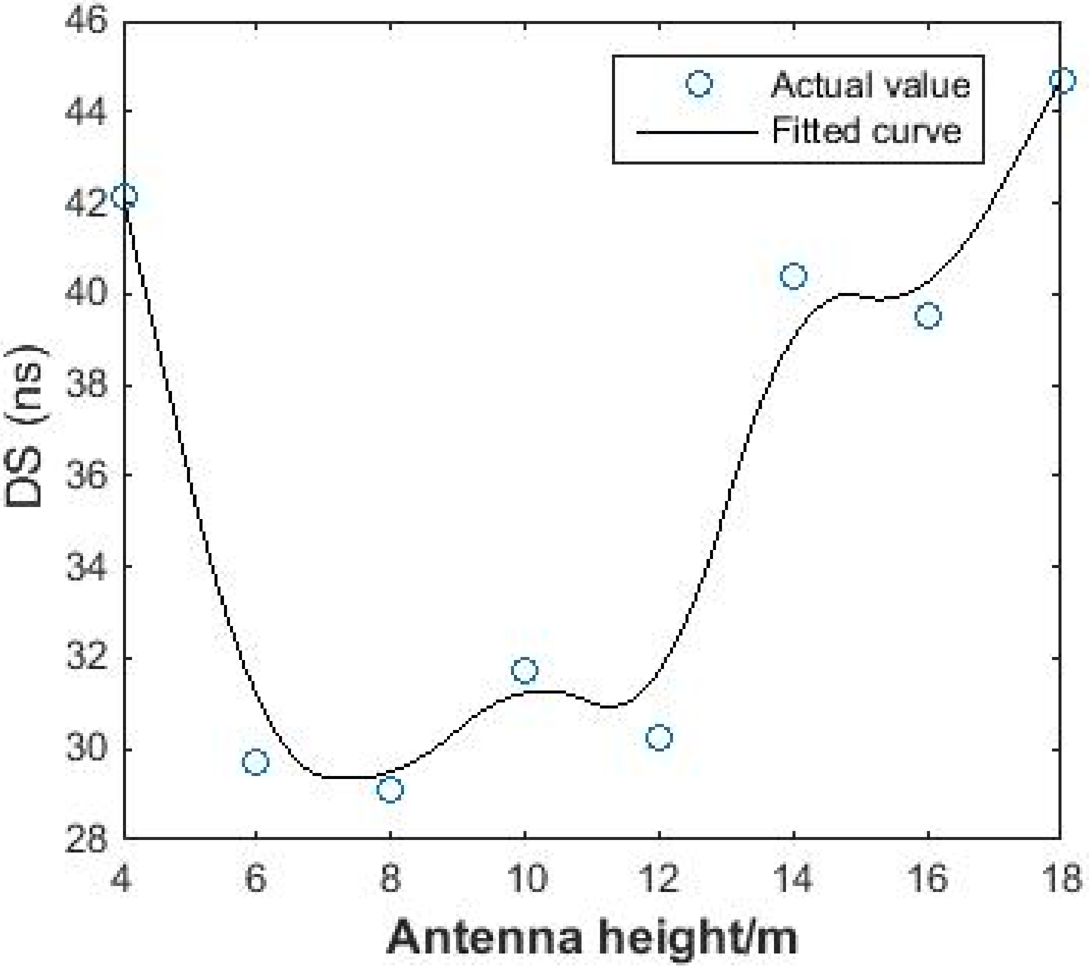

Fig. 3.6 The DS under the straight street with various antenna heights (4 m, 6 m, 8 m, 10 m, 12 m 14 m, 16 m, and 18 m).

After fitting the curves under different antenna heights (4m, 6m, 8m, 10m, 12m, 14m, 16m and 18m), the PDFs of EAoD and EAoA can be obtained as indicated in Table 3.3.

From Table 3.3, two conclusions can be reached:

1. For the PDF of EAoD: the logarithm exponent value $\lambda_{1EAoD}^{'}$ is nearly unchangeable when the antenna height is lower than half of the building's height, but has a dramatic increase when the antenna height grows. However, the logarithm exponent value $\lambda_{2EAoD}^{'}$ enhances when the antenna height is lower than half of the building's height and then remains stable.
2. For the PDF of EAoA: the logarithm exponent value $\lambda_{1EAoA}^{'}$ decreases rapidly when the antenna height is lower than half of the building's height and then varies slightly. However, the

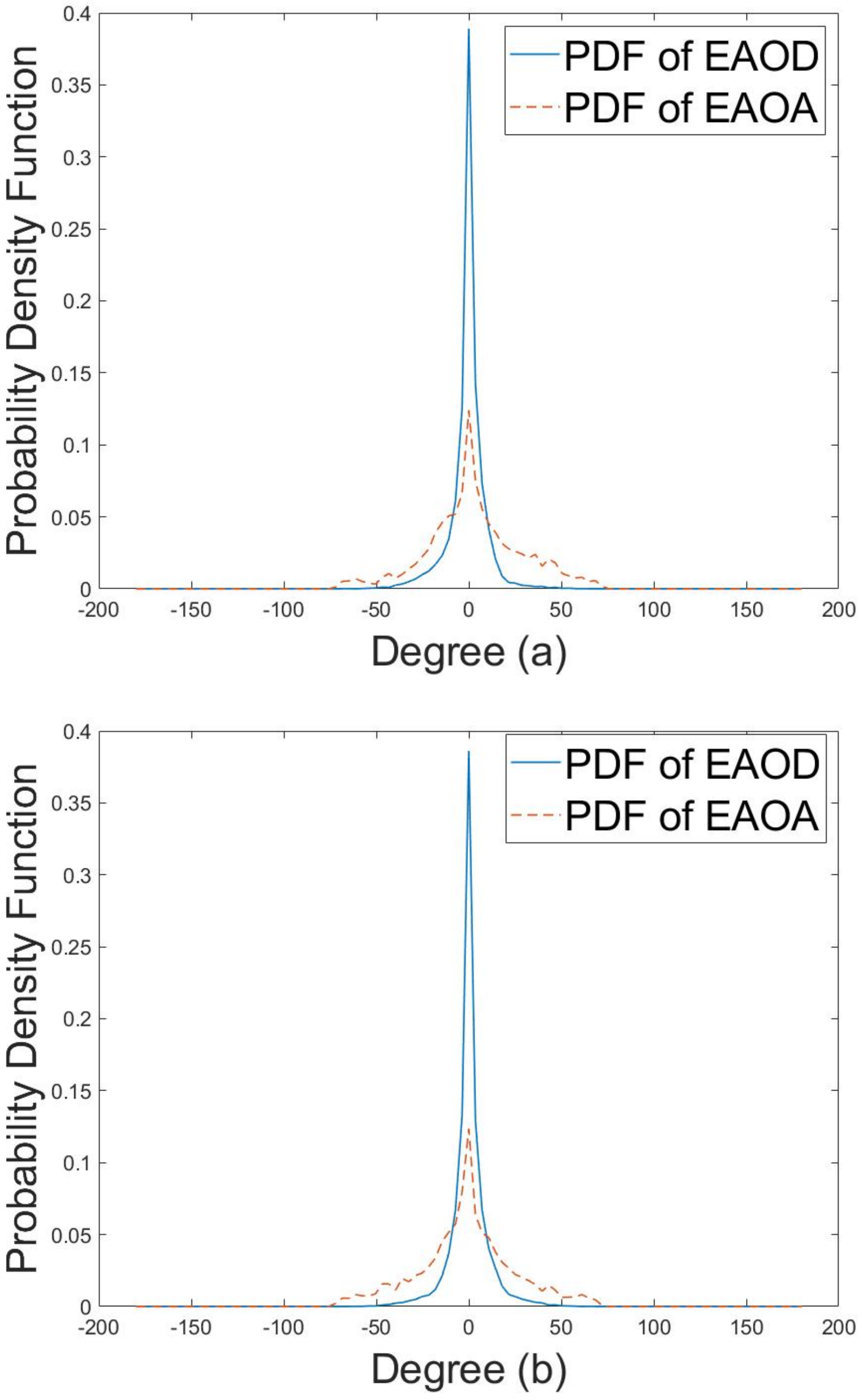

Fig. 3.7 PDFs of EAoD and EAoA under the forked road scenario. The fist figure is the description of the antenna height at 8 m; and the second figure is the description of the antenna height at 12 m.

	4m	6m	8m	10m	12m	14m	16m	18m
EAoD down	40.19	32.86	32.31	33.16	33.16	33.25	34.58	36.2
EAoD up	-32.49	-35.89	-34.23	-33.67	-32.63	-32.99	-32.93	-32.94
EAoA down	17.4	20.92	19.11	18	17.69	17.94	17.95	18.03
EAoD down	-18.06	-16.2	-15.77	-16	-17.06	-16.64	-16.45	-18.68

Table 3.3 The statistic results of logarithm exponent values under fork road scenario with various antenna heights (4 m, 6 m, 8 m, 10 m, 12 m, 14 m, 16 m, and 18 m). Here, EAoD down, EAoD up, EAoA down, and EAoA up represent $\lambda_{1EAoD}^{'}$, $\lambda_{2EAoD}^{'}$, $\lambda_{1EAoA}^{'}$ and $\lambda_{2EAoA}^{'}$ respectively

logarithm exponent value $\lambda_{2EAoA}^{'}$ is almost stable when the antenna height is lower than half of the building's height, but has a significant drop when the antenna height increases.

Finally, the PDFs of EAoD and EAoA related to antenna height can be calculated:

$$f_{EAoD}(x) = \begin{cases} -(7.64)\exp(7.64), & x < 0, m \leq 12.5 \\ -(-0.14m+5.89)\exp(-0.14m+5.89), & x < 0, 12.5 < m \leq 12.5 \\ -(-0.07m-8.43)\exp(-0.07m-8.43), & x > 0, m \leq 25 \\ -(-7.58)\exp(-7.58), & x > 0, 12.5 < m \leq 25 \end{cases} \tag{3.10}$$

$$f_{EAoA}(x) = \begin{cases} -(-0.06m+4.87)\exp(-0.06m+4.87), & x < 0, m \leq 12.5 \\ -(4.13)\exp(4.13), & x < 0, 12.5 < m \leq 25 \\ -(-3.80)\exp(-3.80), & x > 0, m \leq 25 \\ -(-0.06m-3.01)\exp(-0.06m-3.01), & x > 0, 12.5 < m \leq 25 \end{cases} \tag{3.11}$$

With the results obtained above, the AS and the DS of EAoD and EAoA can be gained as displayed in Fig. 3.8 and Fig. 3.9.

It is obvious from Fig. 3.8 that the ASs of EAoD and EAoA arrive at the peak value when

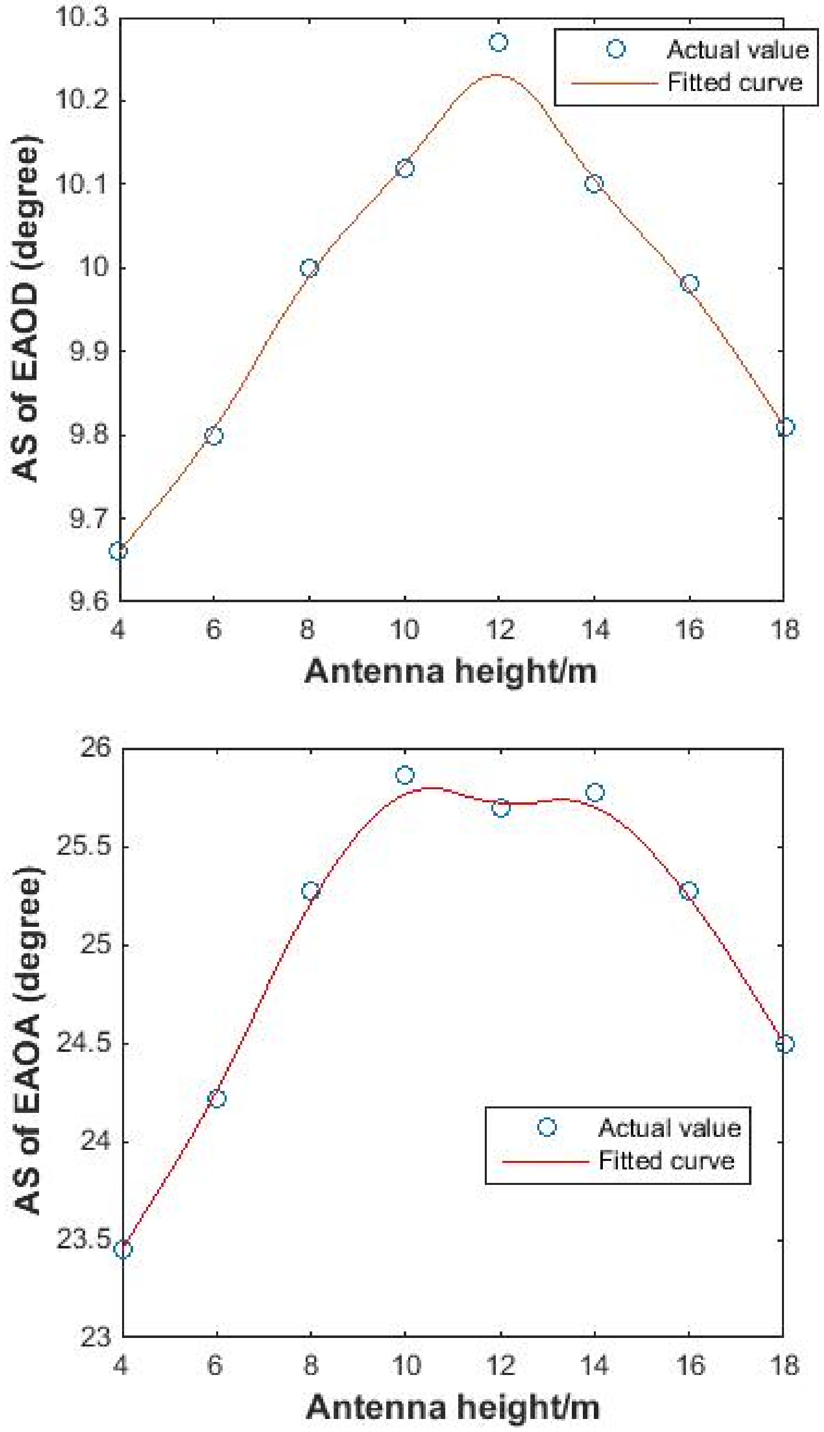

Fig. 3.8 The AS under the forked road scenario with various antenna heights (4 m, 6 m, 8 m, 10 m, 12 m, 14 m, 16 m, and 18 m). The first figure is the description of the AS of EAoD; and the second figure is the description of the AS of EAoA.

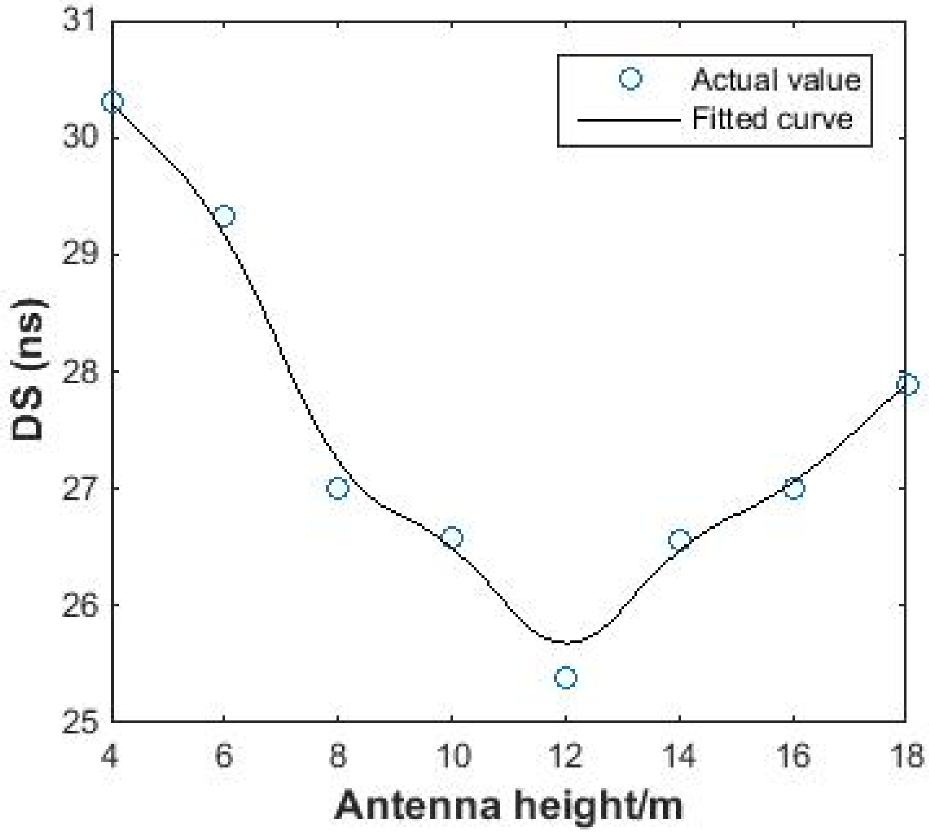

Fig. 3.9 The DS under the forked road scenario with various antenna heights (4 m, 6 m, 8 m, 10 m, 12 m 14 m, 16 m, and 18 m).

the antenna height (12 m) is half of the building's height. In Fig. 3.9, we can conclude that the minimum value of the DS can be achieved when the antenna height is half of the building's height and the value arises when the antenna is near the ground or the top of the buildings.

Finally, the AS and the DS related to antenna height can be represented as:

$$\sigma_{AS,EAoD} = \begin{cases} 0.0824m + 9.2706, & m \leq 12.5 \\ -0.1273m + 11.8909, & 12.5 < m \leq 250 \end{cases} \tag{3.12}$$

$$\sigma_{AS,EAoA} = \begin{cases} 0.2412m + 22.6853, & m \leq 12.5 \\ -0.2m + 28.2, & 12.5 < m \leq 25 \end{cases} \tag{3.13}$$

$$\sigma_{DS} = \begin{cases} -0.5647m + 32.5588, & m \leq 12.5 \\ 0.4364m + 20.0455, & 12.5 < m \leq 25 \end{cases} \tag{3.14}$$

3.3.3 Scenario C: Crossroad in the Center of Paris

Finally, we research the PDFs of EAoD and EAoA under cross road scenario as shown in Fig. 3.2(c). The simulation results are obtained when the antenna located at 8m and 12m as shown in Fig. 3.10.

The logarithm exponent values of EAoD and EAoA can be obtained by fitting the curves through different antenna heights (4 m, 6 m, 8 m, 10 m, 12 m, 14 m, 16 m, and 18 m) which are exhibited in Table 3.4.

	4m	6m	8m	10m	12m	14m	16m	18m
EAoD down	199	149.8	118.3	110.5	88.88	79.08	85.5	79.05
EAoD up	-79.57	-87.87	-76.54	-85.21	-103	-113.1	-131.2	-172.7
EAoA down	19.52	17.72	14.08	12.08	12.87	10.91	9.77	11.1
EAoD down	-9.556	-12.86	-10.7	-11.25	-13.12	-13.46	-15.32	-19.56

Table 3.4 The statistic results of logarithm exponent values under crossroad scenario with various antenna heights (4 m, 6 m, 8 m, 10 m, 12 m, 14 m, 16 m, and 18 m). Here, EAoD down, EAoD up, EAoA down, and EAoA up represent λ'_{1EAoD}, λ'_{2EAoD}, λ'_{1EAoA} and λ'_{2EAoA} respectively

From Table 3.4, we can conclude that:

1. For the PDF of EAoD: the logarithm exponent value λ'_{1EAoD} reduces rapidly when the antenna height is lower than half of the building's height, and gains the minimum value at 14 m, and then the value remains the same. In contrast, the logarithm exponent value λ'_{2EAoD} is nearly unchangeable when the antenna height is lower than half of the building's height, but has a dramatic decrease when the antenna height grows.

2. For the PDF of EAoA: the exponent value decreases λ'_{1EAoA} as the antenna height rises. In contrast, the exponent value λ'_{2EAoA} is nearly unchanged when the antenna height is lower than half of the building's height, but has a significantly drop when the antenna height increases.

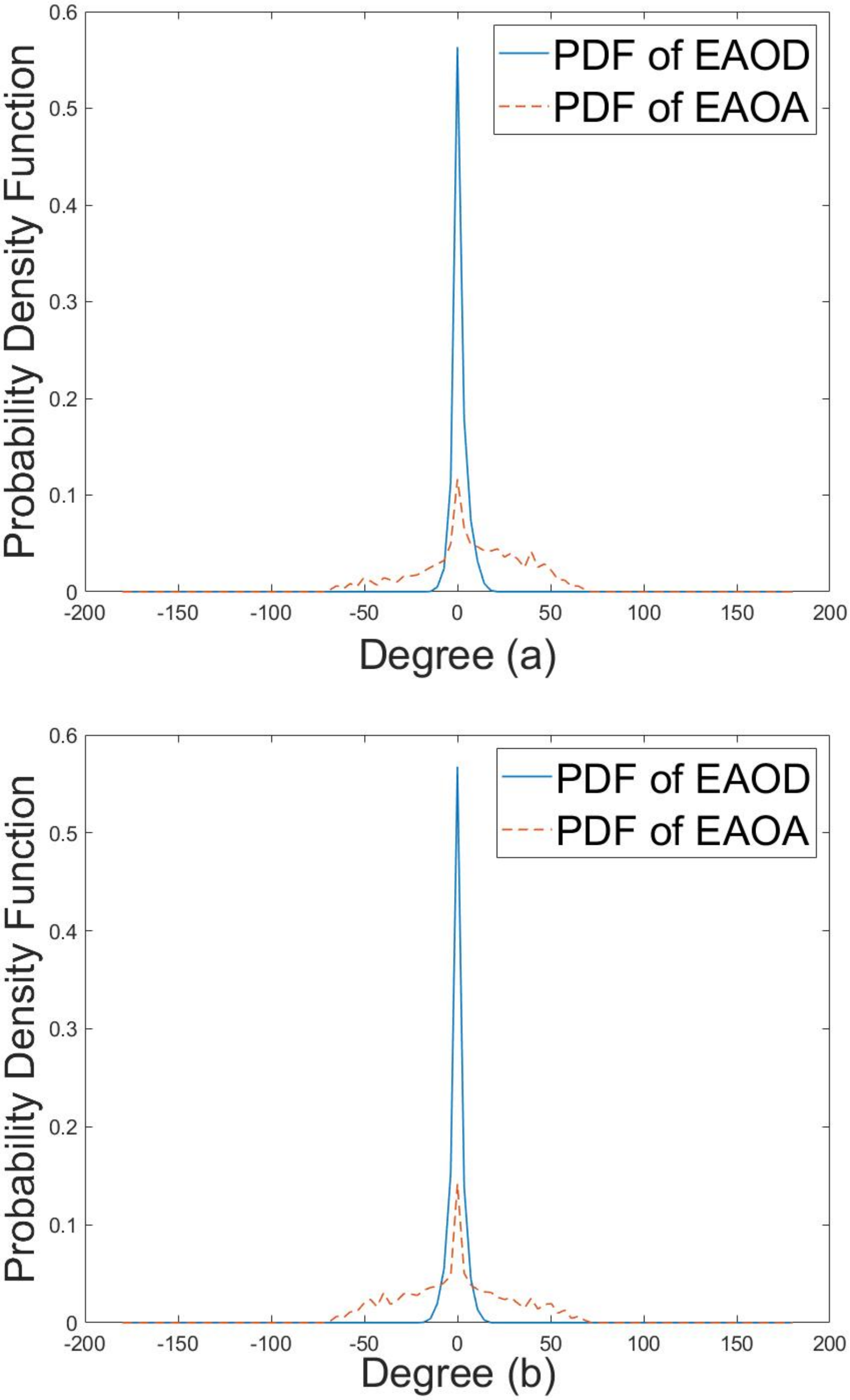

Fig. 3.10 PDFs of EAoD and EAoA under the forked road scenario. The fist figure is the description of the antenna height at 8 m; and the second figure is the description of the antenna height at 12 m.

Then, the PDFs of EAoD and EAoA can be represented as:

$$f_{EAoD}(x) = \begin{cases} -(-2.95m+52.22)\exp(-2.95m+52.22), & x<0, m\leq 11 \\ -(19.80)\exp(19.80), & x<0, 11<m\leq 22 \\ -(-20.72)\exp(-20.72), & x>0, m\leq 11 \\ -(-1.90m+0.15)\exp(-1.90m+0.15), & x>0, 11<m\leq 22 \end{cases} \tag{3.15}$$

$$f_{EAoA}(x) = \begin{cases} -(-0.17m+5.15)\exp(-0.17m+5.15), & x<0, 0<m\leq 20 \\ -(-2.76)\exp(-2.76), & x>0, m\leq 11 \\ -(-0.15m-1.08)\exp(-0.15m-1.08), & x>0, 11<m\leq 22 \end{cases} \tag{3.16}$$

The DS and the AS of EAoD and EAoA can be gained by the above results.

The DS shows a similar phonomenon as that described in Sections 3.3.1 and 3.3.2 and as shown in Fig. 3.11. The first figure in Fig. 3.12 shows that the AS of EAoD remains almost stable with different antenna heights. The second figure in Fig. 3.12 illustrates the AS of EAoA gains its maximum value when the antenna height is half of the building's height (11 m) and drops gradually to the ground or the top of the buildings.

Finally, the AS and the DS related to antenna height can be represented as:

$$\sigma_{AS,EAoD} = 4.05 \tag{3.17}$$

$$\sigma_{AS,EAoA} = \begin{cases} 0.9857m+17.7571, & m\leq 11 \\ -0.9m+23, & 11<m\leq 22 \end{cases} \tag{3.18}$$

$$\sigma_{DS} = \begin{cases} -0.3571m+18.4286, & m\leq 11 \\ 0.3m+11.2, & 11<m\leq 22 \end{cases} \tag{3.19}$$

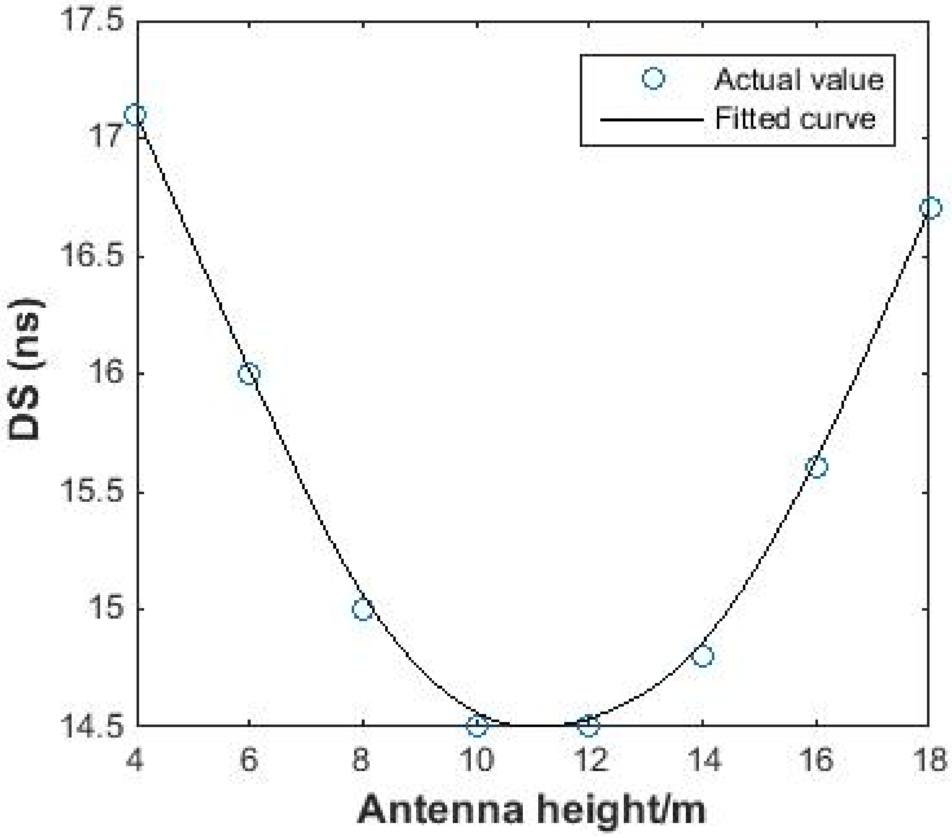

Fig. 3.11 The DS under the forked road scenario with various antenna heights (4 m, 6 m, 8 m, 10 m, 12 m 14 m, 16 m, and 18 m).

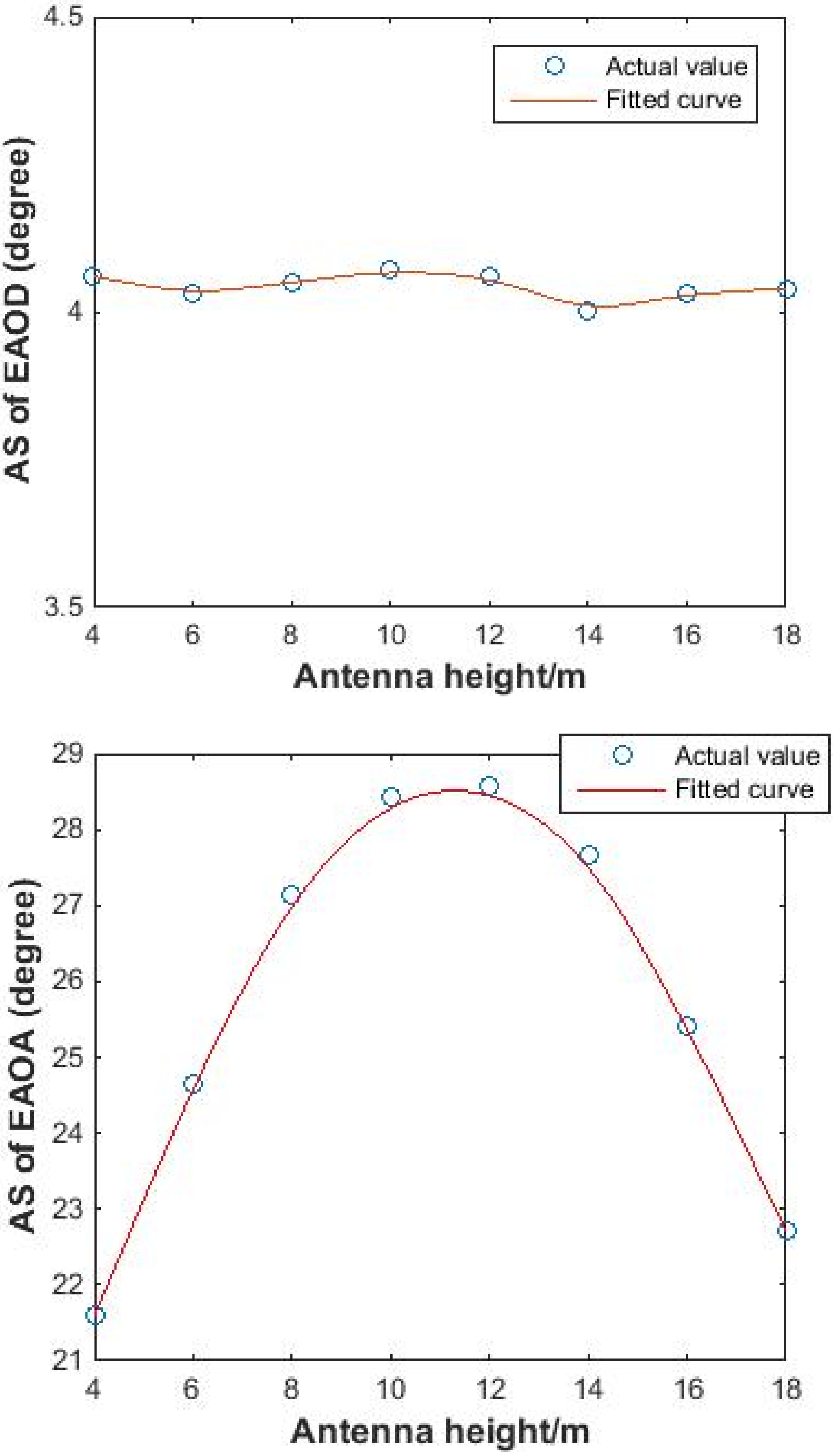

Fig. 3.12 The AS under the Crossroad scenario with various antenna heights (4 m, 6 m, 8 m, 10 m, 12 m, 14 m, 16 m, and 18 m). The first figure is the description of the AS of EAoD; and the second figure is the description of the AS of EAoA.

3.4 Discussions

Based on the simulation results in Section 3.3.1–3.3.2, some insights and observations regarding the 3-D wireless channels are given as follows: On the one hand, to obtain the maximum and minimum values of the AS and the DS, BS antennas need to be located at half of the building's height under three typical street scenarios. On the other hand, the PDFs of EAoD and EAoA are approximated as double-sided exponential functions. Meanwhile, the parameters of the double-sided exponential function are linearly correlated with the antenna height under the straight street scenario, but change dramatically when the BS antenna height is half of the buildings height under forked road and crossroad scenarios.

Futhermore, form Fig. 3.3, 3.7, and 3.10 we can find that most numbers of EAoD and EAoA concentrate at 0 radians, even though we ignore the LoS component. Generally, the path distance of a single reflection angle is smaller than the multi-path which makes the weighting value higher. Thus, we can conclude that the single reflection path plays a leading role for researching the distributions of EAoD and EAoA.

3.5 Conclusions

In this chapter, the impact of antenna height on EAoD and EAoA is investigated under typical outdoor scenarios: straight street, forked road, and crossroad. At the beginning, we briefly introduced the IRLA and the simulation scenario (center of Paris). Then, the closed-form expressions of the PDF of EAoD and EAoA were derived under various street scenarios. Simultaneous, the related AS and DS are also presented. Finally, the discussion of the results were given. According to the results, we conclude that the PDFs of EAoD and EAoA are modelled as exponential functions whose parameters are observed as a linear function of the antenna height under the straight street scenario. Meanwhile, the characteristics of EAoD and EAoA change dramatically when the BS antenna height is half of the building's height in the forked road and crossroad scenarios. Moreover, the results of the AS and DS show that in order to obtain the maximum or minimum value of the AS and the DS, the BS antenna should be deployed at half of the building's height under three typical street scenarios. We also conclude that the single reflection path dominates the distribution of EAoD and EAoA. In our future works, the PDFs of EAoD and EAoA with different antenna patterns and tilt will be considered under typical outdoor scenarios.

Chapter 4

2-D and 3-D Elevation Angle Models for Small Cell Environments

Overview

The deployment of small cells is one of the key enabling technologies for the next generation mobile communication. Due to the short coverage of small cells, the elevation angle, which is ignored in long distance transmission model, should be considered in channel modeling. In this chapter, an elevation angle model is proposed for the small cell environment with a geometrically based single bounce method. Two scatterer models are discussed. The first model assumes that scattering objects are located uniformly within an ellipse around the MS. The closed-form expression for joint and marginal PDF of EAoD is derived and validated by Monte Carlo simulation. With our derived PDF expression, the impacts of parameters such as the distance between the BS and MS, the height of the BS and the size of scatterers on the elevation angle are also discussed. In the second model, a MS and a BS, which employs an omnidirectional antenna, are assumed to be located at the center and at a typical point outside of a 3-D scattering ellipsoid, respectively. Closed-form expressions for PDF of the EAoD are derived and validated by Monte Carlo simulation. With our proposed PDF, the spatial correlation is discussed. The results show that the distance between the BS and the MS affects the spatial correlation more patently than the BS antenna height.

4.1 A Proposed 2-D Elevation Angle Model for Small Cell Environments

4.1.1 Introduction

A common feature of the research on future wireless communication technologies is the pursuit of high data amount with multiple MSs. Small cell technologies are expected to play a key role in the future [65]. To thoroughly investigate a small cell, it is essential to have a good understanding of the radio-propagation characteristics of the transmission path between the BS and the MS [101]. Geometrically based models have been verified to be fundamental for the performance evaluation of a mobile communication system. Therefore, different types of geometrical models have been proposed for the characterization of the radio channel [102–104]. For the conventional study on channel model, linear antenna arrays are considered in the horizontal direction. The assumption that the plane waves arrive horizontally is valid for the macrocellular environment since the distance between the MS and BS is much larger than that between the height of the BS antenna and that of the scatterers around the mobile unit. Due to the comprehensive application of a small cell which has short coverage, the elevation angle, which shows great influence on the performance of a mobile system, should also be considered in channel modelling [105].

The first work on EAoD was conducted in 1979 [106]. This model is appropriate to model fading at a mobile unit because scatterers are located close to the mobile and are of different heights. Then, more works have been done to precisely describe the elevation angle. In 1990, a measurement in Tokyo based on a 900 MHz band observed that the distribution of elevation angle was extremely close to Gaussian distribution [107]. After that, the PDF of EAoD of the multipaths at the BS was derived by assuming that the scattering objects are located uniformly within a circle around the MS and that the height of the BS is the same as that of the MS [108]. In work [109], a 3-D scattering model was generalised for macrocellular environment with an MS located at the center of a 3-D scattering semispheroid and a BS employing a directional antenna located outside of the semispheroid. Recently, the PDFs of the elevation angle, elevation AS and the elevation DS have been measured in two typical street environments [110]

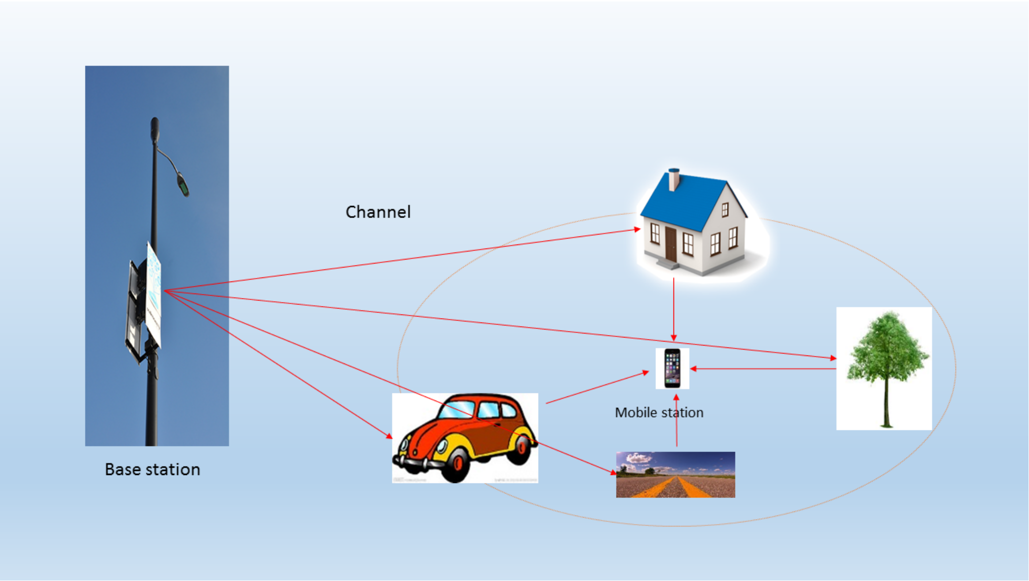

Fig. 4.1 Ellipse scatterers channel model

All the above mentioned studies are limited to long-distance transmission, which is used to model the macrocell channel model. However, few studies have considered the outdoor short-distance transmission model. In [111–113], the authors showed that the elliptical scattering model is more suitable for microcell or picocell types of environments which assume that the scatterers' density is constant within an elliptical region about the MSs and BSs. In this section, we show the development of a geometrical based single-bounce (GBSB) small cell channel model which assumes that the BS is located outside of the scatterers, as shown in Fig 4.1. Therefore, scatterers such as ground, cars, trees, and buildings are located uniformly within an ellipse around the mobile. Using this model, the range of the EAoD is evaluated and its closed-form expression is derived. Our obtained PDF of the EAoD is also validated by Monte Carlo simulation and the impacts of parameters such as the distance between the BS and MS, BS height, and the size of the scatterers on EAoD distribution are discussed.

This section is organised as follows. We first propose the GBSB channel model for a small-cell environment and deduce the range of the EAoD. Then, we derive the closed-form expression of the PDF of the EAoD and validate it by Monte Carlo simulation. After that, we relate the

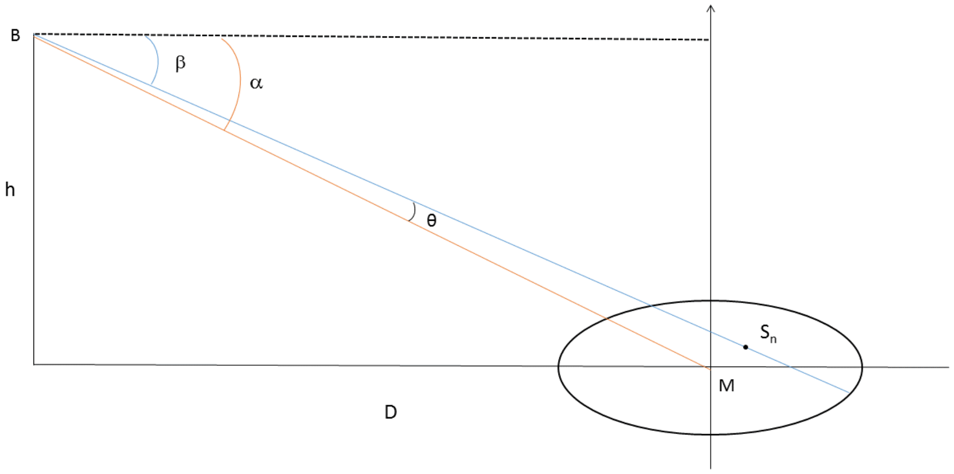

Fig. 4.2 GBSBS channel model

effect of parameters on the PDF of the EAoD by using simulation results. Meanwhile, the spatial correlation with the derived PDF is discussed. Finally, conclusions are presented.

4.1.2 Geometrically Based Single Bounced Small Cell Channel Model

In this subsection, we describe the proposed model and derive the elevation angle region of the multipath components in a small cell. In this model, we assume that each scatterer is an omnidirectional re-radiating element, and the signal is reflected directly to the MS without the influence from other scatterers. The proposed model is shown in Fig. 4.2. The scatterer model is regarded as uniformly located around the MS within an ellipse:

$$\frac{x^2}{a^2} + \frac{y^2}{b^2} = 1, \tag{4.1}$$

where a and b denote the lengths of the semi-major and semi-minor axes of the ellipse. Without loss of generality, we assume that $a > b$ and $b < h$, where h denotes the BS height, which means that the height of the BS is larger than that of the highest scatterer. We set the centre point of the ellipse as the origin of the coordinates. The parameters B, M, and S_n in Fig. 4.2 denote the BS, MS and scatterers, respectively, where $n = 1 \cdots n$ represents the number of scatterers. Therefore, the line set of BS_n can be represented as:

$$BS_n : y - h = k(x + D), k = -\tan(\beta), \tag{4.2}$$

where D is the distance between the BS and MS, and β is the intersection angle between BS_n and x axis. If the angle between BM and x axis is denoted as α, then according to definition of elevation angle in [108], the EAoD θ can be evaluated as: $\theta = \alpha - \beta$. To derive the PDF of θ, the restriction of the θ should be calculated first, which is given in Lemma 1.

Lemma 1. *The restriction of the range of θ is given as:*

$$\theta \in (\alpha - \beta_1, \alpha - \beta_2). \tag{4.3}$$

where, β_1 and β_2 indicates the maximum and minimum value of β:

$$\beta_i = \arctan \frac{(-1)^{i+1} b \sqrt{1 - (sin(t_i))^2}}{asin(t_i)}, i = 1, 2, \tag{4.4}$$

$$sin(t_i) = \frac{a^2bh + (-1)^i \sqrt{D^2a^2b^2h + D^4b^4 - D^2a^2h^4}}{a^2h^2 + D^2b^2}, i = 1, 2. \tag{4.5}$$

Proof. According to $\alpha = \arctan(\frac{h}{D})$ which is a fixed value, the restriction of the range of θ is determined by the range of β. For this purpose, we transfer the ellipse equation to a parametric equation, as follows:

$$x = a\cos(t), y = b\sin(t) \quad t \in (0, 2\pi) \tag{4.6}$$

With the slope function of the tangent line at the point of the ellipse and that of the plane δ, the following equation can be obtained:

$$\frac{-b\cos(t)}{a\sin(t)} = \frac{h - b\sin(t)}{-D - a\cos(t)}. \tag{4.7}$$

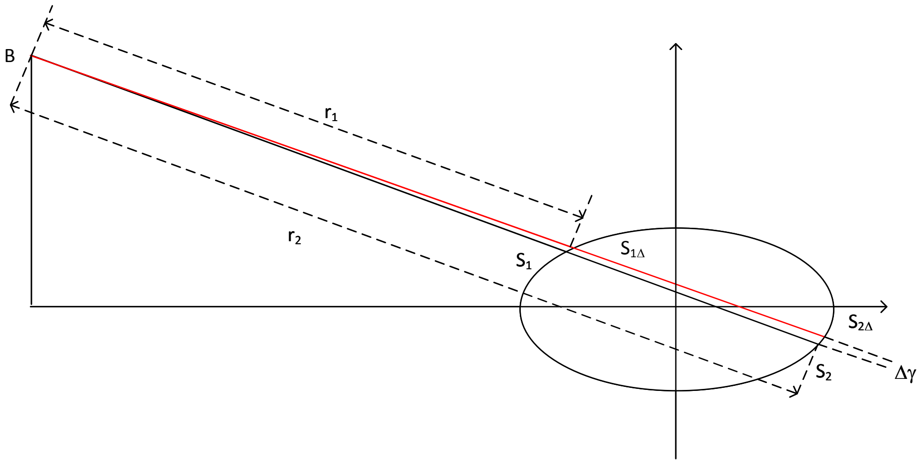

Fig. 4.3 EAoD model

This yields the range of β. Therefore, the range of EAoD can be calculated using formulation (4.3). □

4.1.3 PDF of EAoD

For clearly investigating the PDF of EAoD, Fig. 4.3 is given. Let us consider the strip $S_1S_{1\Delta}S_{2\Delta}S_2$ between γ and $\gamma+\Delta_\gamma$, where γ is the EAoD and Δ_γ is an infinitely small angle, which is approximately 0. S_1, S_2 and $S_{1\Delta}$, $S_{2\Delta}$ represent the intersections of two lines in BS_n (corresponding to two angles γ and Δ_γ) and the ellipse, respectively. Since the scatterers are uniformly distributed around the MS, the area within the strip accounts for the proportion of the entire ellipse can represent the probability of EAoD which is given in Theorem 1.

Theorem 1. *The PDF of the EAoD can be represented as follows:*

$$f(\theta)=\begin{cases}\dfrac{\sqrt{-D^2k^2-2Dhk+a^2k^2+b^2-h^2}}{f_1(\theta)(a^2k^2+b^2)^2}\times 4ab(k^2+1)(-hka^2+Db^2), & \\ \qquad \theta\in(\alpha-\beta_1,\alpha-\beta_2) & \\ 0, & otherwise\end{cases} \tag{4.8}$$

Proof. In order to obtain the PDF of the EAoD, the area of the strip $S_{S_1S_{1\Delta}S_{2\Delta}S_2}$ should be evaluated first. Fig. 4.3 shows that $S_{S_1S_{1\Delta}S_{2\Delta}S_2}=S_{BS_1S_{1\Delta}}-S_{BS_2S_{2\Delta}}$, where $S_{BS_1S_{1\Delta}}$ and $S_{BS_2S_{2\Delta}}$ is the area of the $BS_1S_{1\Delta}$ and $BS_2S_{2\Delta}$, respectively. Then, according to the infinitely small value of Δ_γ, the $BS_1S_{1\Delta}$ and $BS_2S_{2\Delta}$ can be regarded as a circular sector. Thus, $S_{BS_1S_{1\Delta}}$ and $S_{BS_2S_{2\Delta}}$ can be evaluated as:

$$S_{BS_iS_{i\Delta}} = \int_{\gamma}^{\gamma+\Delta\gamma} \frac{r_i^2}{2} d\theta, i = 1,2, \tag{4.9}$$

where r_1 and r_2 represent the lengths of BS_1 and BS_2, respectively.

For the calculation of the r_1 and r_2, we substitute line set equation (4.2) in ellipse equation (4.1) and solve y:

$$\frac{x^2}{a^2} + \frac{[k(x+D)+h]^2}{b^2} = 1. \tag{4.10}$$

This yields the x coordinate of the two points S_{1x} and S_{2x}:

$$\begin{aligned} S_{ix} = & \frac{(-1)^i ab(\sqrt{-D^2k^2 - 2Dhk + a^2k^2 + b^2 - h^2})}{a^2k^2 + b^2} \\ & - \frac{a(ahk + Dak^2)}{a^2k^2 + b^2}, i = 1,2. \end{aligned} \tag{4.11}$$

Substituting equation (4.10) into equation (4.2) to calculate the two corresponding y coordinates S_{1y} and S_{2y}, then $r_{1,2}$ is derived by: $r_i = \sqrt{(S_{ix}+D)^2 + (S_{iy}-H)^2}, i = 1,2$. Therefore, r_1 and r_2 can be expressed as:

$$r_i = ((-1)^{i+1}a^2hk + (-1)^i Db^2 + abw)\frac{\sqrt{k^2+1}}{(a^2k^2+b^2)}, \text{ i=1.2,} \tag{4.12}$$

and $w = \sqrt{-D^2k^2 - 2Dhk + a^2k^2 + b^2 - h^2}$.

After obtaining r_1 and r_2, $S_{S_1S_{1\Delta}S_{2\Delta}S_2}$ can be derived as:

$$S_{S_1S_{1\Delta}S_{2\Delta}S_2} = \int_{\gamma}^{\gamma+\Delta\gamma} \frac{r_2^2 - r_1^2}{2} d\theta. \tag{4.13}$$

The cumulative distribution function (CDF) of the EAoD $F(\theta)$ can be derived by using result above:

$$F(\theta) = \int_0^{\theta} \frac{r_2^2 - r_1^2}{2\pi ab} d\theta. \tag{4.14}$$

By deriving the CDF of EAoD with respect to θ, the PDF of EAoD $f(\theta)$ can be expressed as:

$$f(\theta)=\frac{r_2^2-r_1^2}{2\pi ab f_1(\theta)}. \tag{4.15}$$

where $f_1(\theta)$ is the normalization constant which can be expressed as:

$$f_1(\theta)=\int_{\theta_1}^{\theta_2}\frac{r_2^2-r_1^2}{2\pi ab}\mathrm{d}\theta, \tag{4.16}$$

Thus, the study of the $f(\theta)$ is now reduced to the evaluation of the $f_1(\theta)$. According to $k=-\tan(\alpha-\theta)$, and $d\theta=\frac{dk}{1+k^2}$. The $f_1(\theta)$ can be expressed as:

$$f_1(\theta)=\int_{k_1}^{k_2}\frac{2w(k^2+1)}{\pi}(Db^2-a^2hk)(a^2k^2+b^2)^{-2}\mathrm{d}k, \tag{4.17}$$

According to

$$w=(k-w_1)^{\frac{1}{2}}\times(k-w_2)^{\frac{1}{2}}, \tag{4.18}$$

where

$$w_i=\frac{Dh-(-1)^i\sqrt{D^2h^2-(a^2-D^2)(b^2-h^2)}}{a^2-D^2}, i=1.2. \tag{4.19}$$

By using Newton's binomial formula, we can obtain:

$$f_1(\theta)=\frac{2Db^2G}{\pi(i+j+2\eta+1)}k^{i+j+2\eta+1}\Big|_{k_1}^{k_2}-\frac{2ha^2G}{\pi(i+j+2\eta+2)}k^{i+j+2\eta+2}\Big|_{k_1}^{k_2}, \tag{4.20}$$

where,

$$G=\sum_{i=0}^{\infty}\binom{\frac{1}{2}}{i}w_1^{\frac{1}{2}-i}\sum_{j=0}^{\infty}\binom{\frac{1}{2}}{i}w_2^{\frac{1}{2}-j}\sum_{\eta=0}^{\infty}\binom{-2}{\eta}a^{2\eta}b^{-4-2\eta}, \tag{4.21}$$

and

$$\binom{\tau}{\upsilon}=\frac{\tau(\tau-1)\dots(\tau-\upsilon+1)}{\upsilon!}. \tag{4.22}$$

Equipped with the equations above, the PDF expression of the EAoD (4.8) can be derived.

□

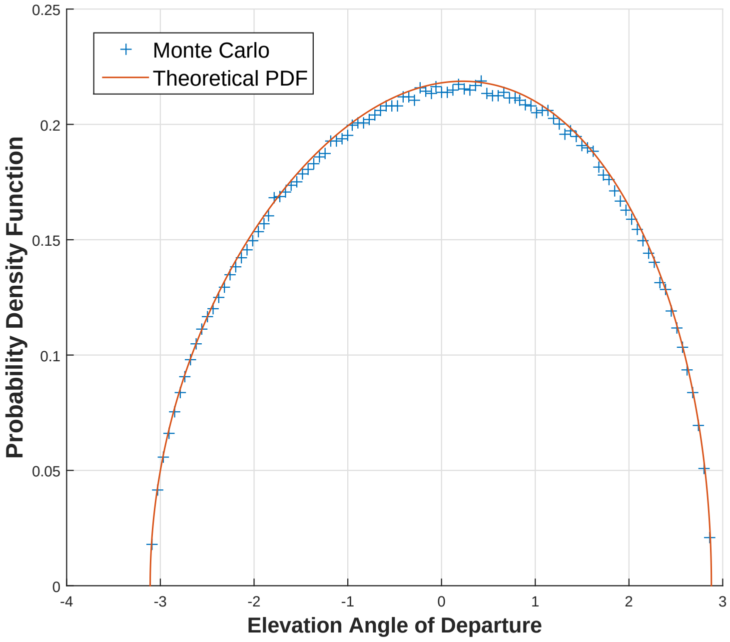

Fig. 4.4 PDF for Theoretical and Monte Carlo

In order to validate our proposed theoretical model, the results of the theoretical model and the Monte Carlo simulation are compared. The parameters of Monte Carlo simulation are shown in Table 4.1:

Parameter	Description	Value
D	Distance between BS and MS	200m
h	Height of BS	20m
a	length of semi-major of the ellipse	30m
b	length of semi-minor of ellipse	10m

Table 4.1 Parameter settings for the experimental scenarios.

By creating uniformly scatterers located around a mobile within an ellipse, the histogram for the EAoD can be obtained by conduction 10,000 Monte Carlo simulations. The PDF of the EAoD for the theoretical model and the Monte Carlo simulation are plotted in Fig. 4.4. As can be seen in this figure, the Monte Carlo simulation results closely match the theoretical results, which justifies our derivation.

4.1.4 The Impact of Parameters on the PDF of the EAoD

With the model derived in Section 4.1.3, we can see that the parameters such as the distance between the BS MS, the BS height and the type of scatterers have great impact on the PDF of the EAoD. In this subsection, we will analyse their impacts in detail.

The PDF of the EAoD with various distances between BS and MS

The PDF of the EAoD with various distances between the BS and MS is shown in Fig. 4.5. During the simulation, we fix the height of the BS, the length of the semi-major (located on x-axis) and the length of the semi-minor axis of the ellipse 20, 30 and 10m, respectively. The distance between the BS MS ranges from 50 to 200m.

Fig. 4.5 indicates that as the distance between the BS and MS increases, the vertex point of the curve approaches 0^0 and the variation range of EAoD decreases. One common feature of these four curves is that the region of the rising edge is much larger than that of the falling edge, which means that the elevation angle that is below the connecting line of the BS and MS has higher proportion than that above the connecting line. Moreover, as long as the grows of the distance between the BS and MS, the range of the elevation angle increases.

The PDF of the EAoD with various BS heights

The PDF of the EAoD with various BS heights is plotted in Fig. 4.6, where the distance between the BS and MS is set 100m. Moreover, the lengths of the semi-major (located on x-axis) and semi-minor axes of the ellipse are set as 30 and 10 m, respectively. In addition, the BS height is varied from 10 to 30 m.

Fig. 4.6 shows that with an increase in BS height, the range of EAoD expands and the vertex points of the curves rise. Another phenomenon observed is that the elevation angle which is below the connecting line between the BS and MS has a conspicuous increase when the BS height increases, while that above the connecting line remains nearly unchanged. What’s more, the range of the elevation angle has a slightly increase when the antenna hight grows.

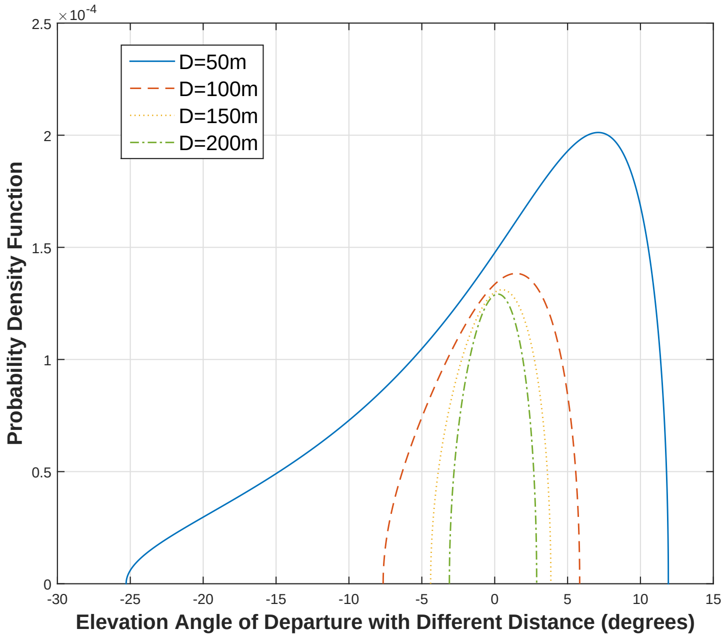

Fig. 4.5 PDF of EAoD with various distance between BS and MS (50m, 100m, 150m, 200m)

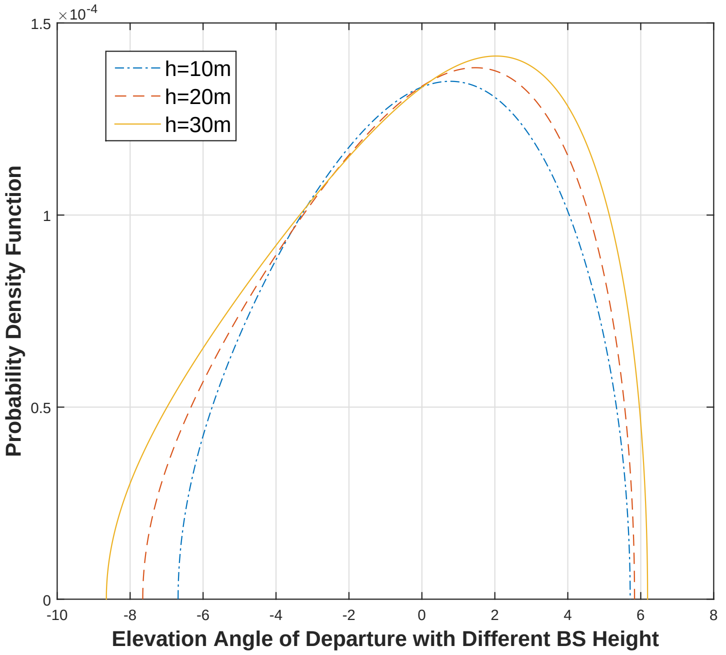

Fig. 4.6 PDF of EAoD with various BS height (10m, 20m, 30m)

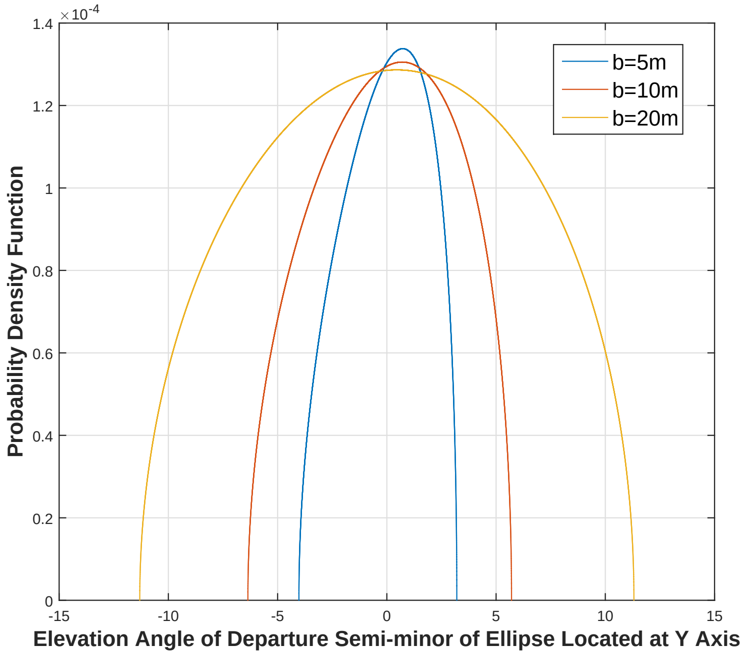

Fig. 4.7 PDF of EAoD with various semi-minor axis height (5m, 10m, 20m) at y axis

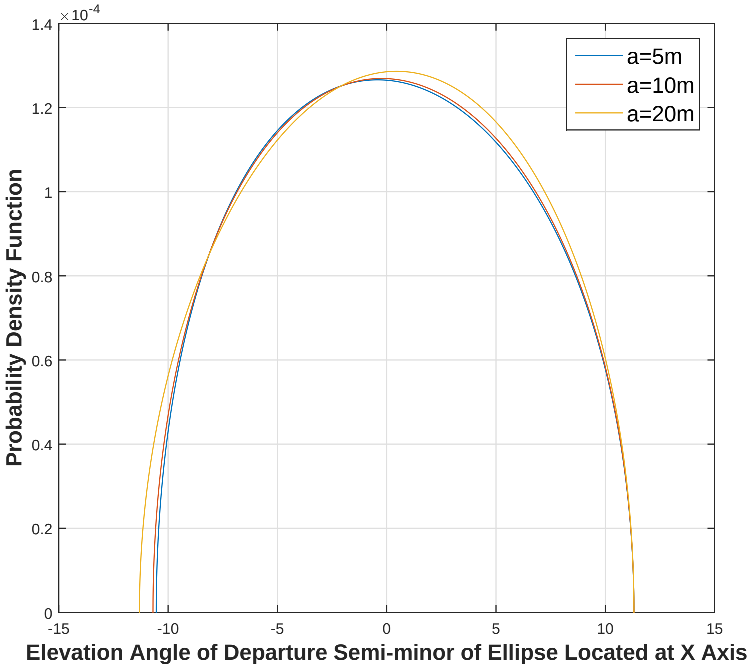

Fig. 4.8 PDF of EAoD with various semi-minor axis height (5m, 10m, 20m) at x axis

The PDF of the EAoD with various type of scatterers

Here, we discuss the PDF of the EAoD from two aspects: the semi-minor axis of the ellipse is located on the y-axis or x-axis. Here, we fix the distance between the BS and MS to 100 m and the height of the BS is 20 m. First, the semi-major axis of the ellipse is located on the x-axis, and is set as 30 m. The semi-minor axis on the y-axis is set as 5, 10, and 20 m. The PDF of the EAoD is shown in Fig. 4.7.

Then, we locate the semi-major axis of the ellipse on the y-axis and set the value as 30 m. The semi-minor axis on the x-axis ranges from 5 to 20 m. The PDF of the EAoD is shown in Fig. 4.8.

The above two figures show that the vertex points of these curves remain nearly unchanged with the increasing length of the semi-minor axis. The range of the EAoD obviously increases when the length of the semi-minor increases on the y-axis. However, the variation can be ignored when the length of the semi-minor axis increases on the x-axis.

From these four figures, we can conclude that the distance between the BS and MS, as well as the height of the scatterers, in the vertical plane shows great influence on the PDF of EAoD. Meanwhile, the height of the BS and the length of the scatterers in the horizontal plane have little influence on the PDF of the EAoD.

4.1.5 Spatial correlation of the proposed model

In this subsection, we will first discussed the basic mechanism of the spatial correlation, and then present the spatial correlation using the proposed PDF.

Spatial correlation refers to the waves impinging on two antennas, and has been extensively studied [114, 115]. These previous studies indicated that the spatial correlation coefficient is mainly determined by the PAS and antenna pattern. Without loss of generality, the antenna will be assumed to be omnidirectional in this section. Therefore, the matrix R of the spatial correlation coefficient can be defined as:

$$R_{m,n} = \int_{-\pi}^{\pi} e^{j(\Phi_m(\theta)-\Phi_n(\theta))} P_\theta \theta, \tag{4.23}$$

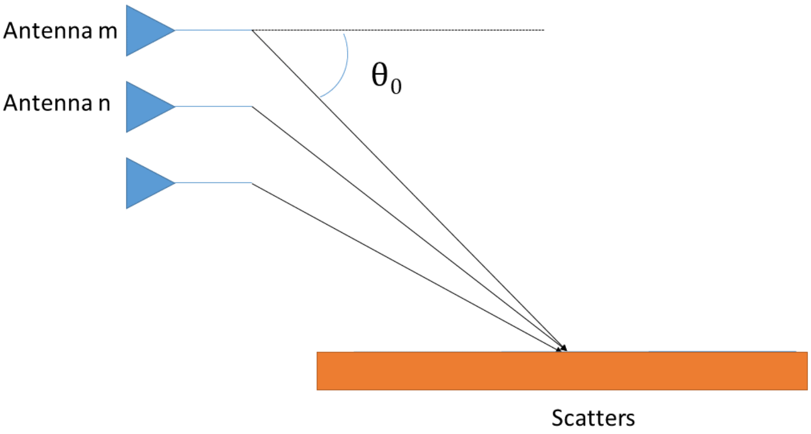

Fig. 4.9 Spatial correlation in the vertical direction

where $\Phi_m(\theta)$, and $\Phi_n(\theta)$ represent the phase for *m*th and *n*th arrays, respectively. P_θ is the PAS, which is the above-derived PDF. Considering two linear adjacent BS antennas in the vertical direction shown in Fig. 4.9, the phase shift of the *2*th and *1*th array can be expressed as:

$$\Phi_2(\theta) - \Phi_1(\theta) = kd\sin(\theta - \theta_0), \tag{4.24}$$

where, $k = \dfrac{2\pi}{\lambda}$ is the wavenumber, d is the distance between the antennas, and θ_0 is the mean value of the EAoD θ. Then, according to the first-order Taylor series,

$$\sin(\theta - \theta_0) \approx \sin\theta_0 - \theta\cos\theta_0, \tag{4.25}$$

where R can be expressed according to the formulations in [116]:

$$R = e^{jkd\sin\theta_0}\int_{-\pi}^{\pi} e^{-jkd\theta\times\cos\theta_0} f(\theta)\mathrm{d}\theta \tag{4.26}$$

Finally, the two Figures (Fig. 4.10, Fig. 4.11) are drawn to discuss the spatial correlation under various scenarios. Fig. 4.10 shows that with an increase in BS antenna height h with the distance between the BS and MS, D, kept constant, the spatial correlation coefficients decrease

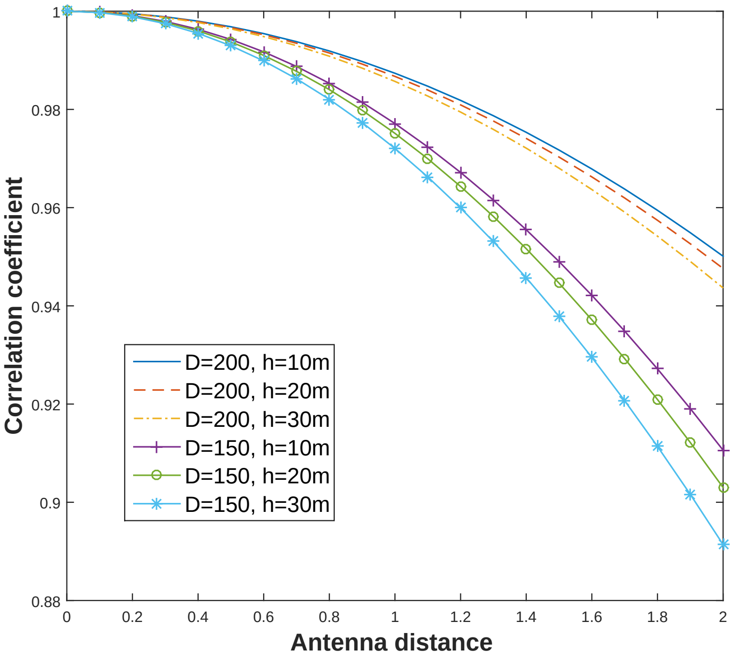

Fig. 4.10 Spatial correction with various distances form BS to MS and various antenna heights.

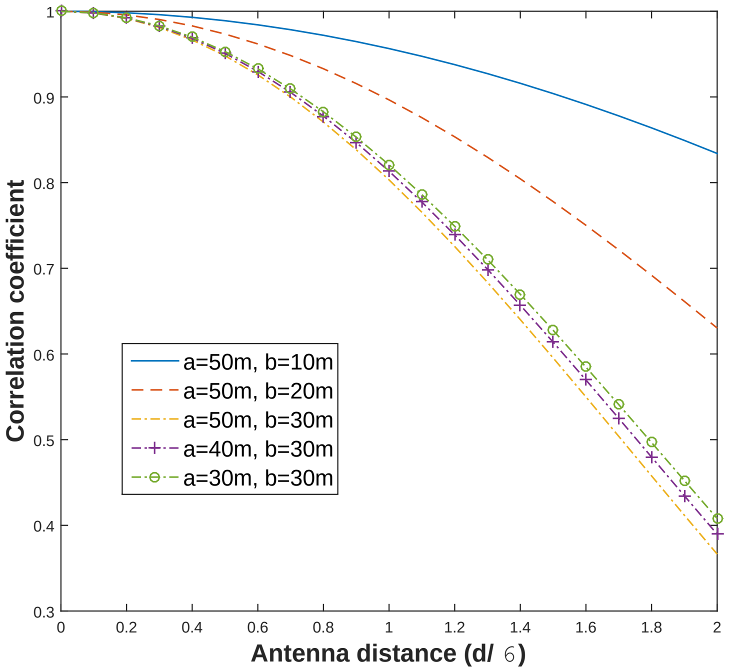

Fig. 4.11 Spatial correction with various type of scatterers.

gradually. Moreover, when D increases with the same h, the spatial correlation coefficients increase significantly. Therefore, we conclude that the distance between the BS and MS shows greater influence on spatial correlation than the BS antenna height.

Fig. 4.11 illustrates that with the growth of the semi-minor axis on the y-axis, b, while maintaining the semi-major axis on the x-axis, a, constant, the spatial correlation coefficients decrease dramatically. Conversely, with the growth of a under a constant b, the spatial correlation remains nearly constant. Therefore, we conclude that the scatterer height affects the spatial correlation more significantly than the scatterer length.

4.1.6 Conclusion

In this section, we proposed a statistical geometric propagation model for a small cell mobile environment. This channel model assumes that the scatterers are located uniformly within an ellipse around the mobile. Closed-form expression of the PDF of the EAoD for this model is derived and verified by Monte Carlo simulation. The impacts of parameters including the distance between the BS and MS, the BS height the scatterers size on the distribution of EAoD are also analysed. We conclude that the distance between the BS and MS, and the scatterer height in a vertical plane have a significant effect on the PDF of the EAoD. Finally, the spatial correlation obtained using the proposed PDF is presented. The results indicate that the distance between the BS and MS together with the scatterer height shows greater influence on the spatial correlation.

4.2 A Proposed 3-D Scattering Elevation Angle Model for Small Cell Environments

4.2.1 Introduction

Nowadays, with universal deployment of small cells, the conventional study studies on channel which focus on the 2-D channel are considered invalid because of the smaller serving distance of the small cells. Therefore, the vertical height of a BS cannot be ignored. The elevation angle is a key metric in the investigation of 3-D channel models with different BS heights [117]. The first work on a 3D channel model can be tracked back to [118], where the author extended the elevation angle into the Clark's model. In work [119], the PDFs of EAoA at the MS were derived under the land mobile environment. In [120], the authors estimated the penetration loss suffered by a building by considering the high elevation angles. In [121], a 3D-vehicle massive MIMO model was developed using the a spherical wave-front instead of the a plane wave-front.

Some elliptical scattering models have been investigated in [111, 122, 113]. In [111], the elliptical scattering model was found to be more suitable for microcell or picocell scenarios. In [122], an ellipse scattering channel model in which the BS and MS were placed at the two foci of the ellipse was developed. Then, in [111], the ellipse scattering model was extended into an elliptical model. However, the case of the BS located outside of the scattering area has not yet been considered in the literature.

In this section, we show the development of a GBSB channel model for a small-cell environment which assumes that the ellipsoid scatterers are located uniformly around the MS and the BS is located at a point outside of the ellipsoid. Using this model, the range of EAoD is evaluated and the closed-form expression of the PDF of EAoD is derived. Our obtained PDF of the EAoD is also validated by Monte Carlo simulation. Moreover, the spatial correlation is analysed based on our proposed model.

This rest of this section is organised as follows. Section 4.2.2 provides the GBSB channel model for a small small-cell environment and the closed closed-form expression of the PDF. In section 4.2.3, we validate the analytical model by using the Monte Carlo simulation and discuss the spatial correlation of our model. Finally, conclusions are given in section 4.2.4.

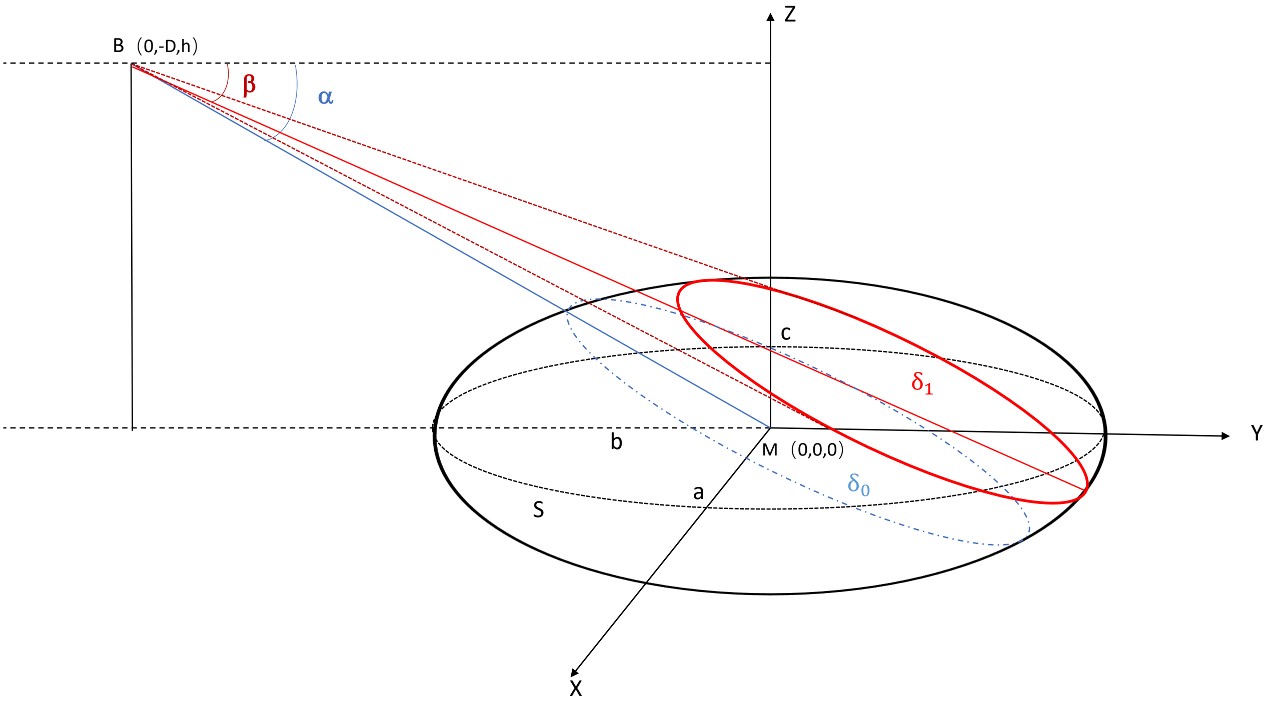

Fig. 4.12 3D GBSB small cell channel model

4.2.2 3-D GBSB channel model for small cell environment

The range of EAoD

The proposed 3-D scattering model is depicted in Fig. 4.12. Considering the scatterers may locate around the MS [123, 124], the scatterers S are assumed to be uniformly placed around the MS within an ellipsoid:

$$\frac{x^2}{a^2} + \frac{y^2}{b^2} + \frac{z^2}{c^2} = 1, \tag{4.27}$$

where a, b, and c respectively denote the three semi-axes of the ellipsoid. Without loss of generality, we assume that $a > b > c$. h denotes the BS height and is larger than the height of the highest scatterer, i.e., $c < h$. The angle between the plane set δ and plane XOY is donated by β, where the δ is defined as the plane set which parallels to the X axis and intersects with point

$B(0,-D,h)$:

$$\delta : ky - z + h + Dk = 0, k = -\tan(\beta). \tag{4.28}$$

where D is the distance between the BS and the MS. Besides, we denote the specific plane in plane set δ which intersects with X axis as δ_0, and the angle between this plane and plane XOY as α. Thus, according to the definition of elevation angle in [109], the EAoD θ can be evaluated as: $\theta = \alpha - \beta$. To derive the PDF of EAoD, the restriction of the θ should be calculated first, which is given in Lemma 2.

Lemma 2. *The restriction of the range of θ is given as:*

$$\theta \in (\alpha - \beta_1, \alpha - \beta_2). \tag{4.29}$$

where, β_1 and β_2 are the maximum and minimum value of β:

$$\beta_\eta = \arctan \frac{(-1)^{\eta+1} c \sqrt{1 - (sin(t_\eta))^2}}{b sin(t_\eta)}, \eta = 1,2, \tag{4.30}$$

$$sin(t_\eta) = \frac{b^2ch + (-1)^\eta \sqrt{D^2c^2b^2h + D^4c^4 - D^2b^2h^4}}{b^2h^2 + D^2c^2}, \eta = 1,2. \tag{4.31}$$

Proof. For purpose of calculation the range of θ, the value of α and the range of β should be achieved respectively. Fig. 4.12 shows that $\alpha = \arctan(\frac{h}{D})$. Thus in order to clearly present the range derivation of β, Fig. **??** is given. Since the ellipsoid is symmetric to the YOZ plane and the plane δ parallels to the X axis, the β_1 and β_2 are represented as the angles between the tangent line of the ellipse in plane YOZ and the x axis. The parametric equation of the ellipse can be expressed:

$$y = b\cos(t), z = c\sin(t) \quad t \in (0, 2\pi). \tag{4.32}$$

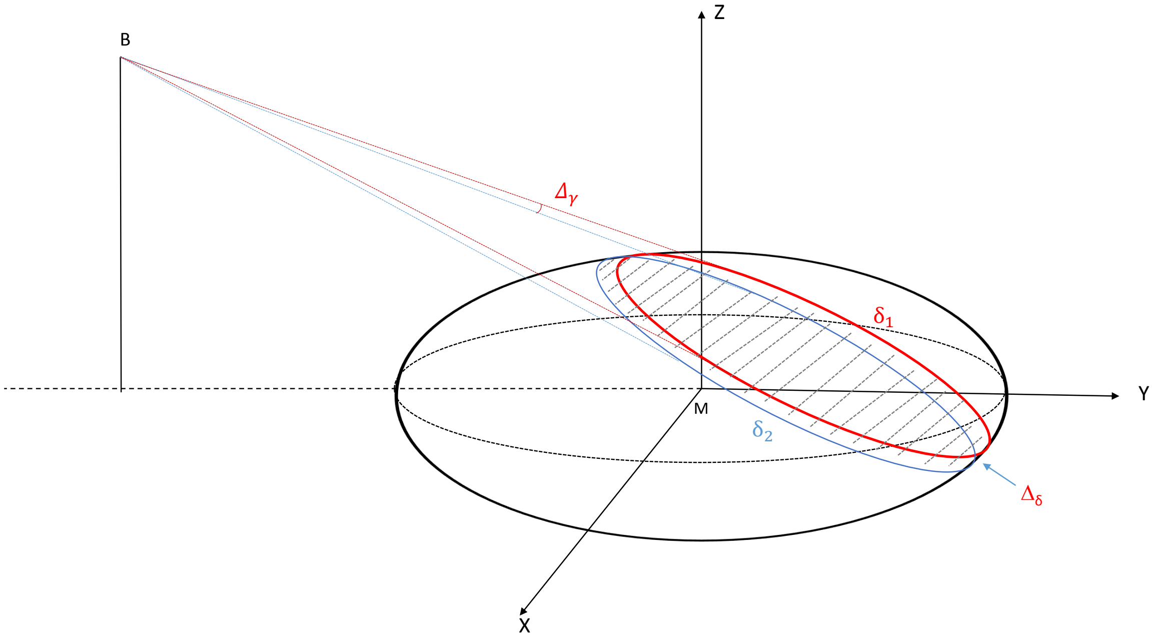

Fig. 4.13 3-D EAoD model

With the slope function of the plane δ and the point-slope equation of a line, the following equation can be obtained:

$$\frac{-c\cos(t)}{b\sin(t)} = \frac{h-c\sin(t)}{-D-b\cos(t)}. \tag{4.33}$$

This yields the range of the β. Therefore, the restriction of the range of θ can be calculated by using the formulation (4.29). □

4.2.3 PDF of EAoD

In the proposed GBSB small cell model, each scatterer is considered as an omnidirectional re-radiating element, and the signal reflected by each scatterer transmits directly to the MS without any influence from other scatters. Thus the amount of scatterers corresponding to each EAoD accounts for the total number of scatterers that can represent the PDF of the EAoD, which is given in Theorem 2.

Theorem 2. *The PDF of EAoD can be represented as the following result:*

$$f(\theta) = \frac{\pi(1+k^2)(Dc^2-b^2hk)w^2}{240(b^2k^2+c^2)^{\frac{5}{2}}f_1(\theta)} \tag{4.34}$$

where, $w=\sqrt{-D^2k^2-2Dhk+b^2k^2+c^2-h^2}$*, and* $k=-\tan(\alpha-\theta)$*.* $f_1(\theta)$ *can be found in expressions (4.50) and (4.51).*

Proof. Since the scatterers are assumed uniformly distributed within the scattering ellipsoid, the PDF of the EAoD can be depicted as the volume of Δ_δ accounting for the proportion of the entire ellipsoid as shown in Fig. 4.13 [108], where Δ_δ is the strip between γ and $\gamma+\Delta_\gamma$. γ is the angle between the plane δ_0 and the plane set δ_1 (the interjection of the plane set δ and the ellipsoid), Δ_γ is an infinitesimal angle which is approximately 0. In order to obtain the volume V_{Δ_δ} of Δ_δ, we regard the Δ_δ as an elliptic cylinder, whose its volume can be calculated by multiplying of the area S_{δ_1} of δ_1 and the height $d\iota$ of the elliptic cylinder.

$$V_{\Delta_\delta} = S_{\delta_1} d\iota. \tag{4.35}$$

Then, we derive the height of the elliptic cylinder and the area S_{δ_1} separately.

The height of the elliptic cylinder

Due to the infinitesimal value of Δ_γ, the value of $d\iota$ is assumed as an arc-length, with the corresponding radius being the distance from point B to the δ_1. It can be approximately derived as:

$$\mathrm{d}\iota = \frac{r_1+r_2}{2}\frac{\pi}{180}\Delta_\gamma, \tag{4.36}$$

where, r_1 and r_2 are the minimum and maximum distances from point B to the δ_1 respectively. Considering that the δ_1 is symmetric to the plane YOZ, the r_1 and r_2 should be also located on the plane YOZ. Then, the problem becomes calculation of the coordinates of the two corresponding points on the plane YOZ. Thus, we substitute the δ equation (4.28) into the ellipsoid equation

(4.27) with $x = 0$: $\frac{y^2}{b^2} + \frac{[k(y+D)+h]^2}{c^2} = 1$, This yields the y coordinate of the two points $y_{1,2}$:

$$\begin{aligned} y_\eta = & \frac{(-1)^\eta bc(\sqrt{-D^2k^2 - 2Dhk + b^2k^2 + c^2 - h^2})}{b^2k^2 + c^2} \\ & - \frac{b(bhk + Dbk^2)}{b^2k^2 + c^2}, \eta = 1,2. \end{aligned} \tag{4.37}$$

By using equation (4.28), the z coordinate of the two points $z_{1,2}$ can also be calculated. Finally the $r_{1,2}$ can be derived as:

$$r_\eta = \sqrt{(y_\eta + D)^2 + (z_\eta - h)^2}, \eta = 1,2. \tag{4.38}$$

Therefore, we can obtain:

$$r_\eta = (-b^2hk + Dc^2 + (-1)^\eta bcw)\frac{\sqrt{k^2+1}}{(b^2k^2+c^2)}, \eta = 1.2, \tag{4.39}$$

and $w = \sqrt{-D^2k^2 - 2Dhk + b^2k^2 + c^2 - h^2}$.

The area of S_{δ_1}

For the calculation of the S_{δ_1}, the semi-minor r_{minor} and semi-major r_{major} axis of δ_1 need to be obtained. On the one hand, considering the symmetry of δ_1, the r_{minor} is also located on the plane YOZ which can be gained by the $y_{1,2}$ and $z_{1,2}$: $r_{minor} = \frac{\sqrt{(z_1-y_1)^2+(z_2-y_2)^2}}{2}$. Thus:

$$r_{minor} = bc\sqrt{(k^2+1)}\frac{\sqrt{-(h+Dk)^2 + c^2 + b^2k^2}}{c^2 + b^2k^2}. \tag{4.40}$$

On the other hand, since the r_{major} is perpendicular to the r_{minor} and parallels to X axis, the length of the r_{major} is the same as that of r'_{major} which is the semi-major axis of the projection area of δ_1 on plane XoY. Therefore, the projection area of δ_1 on plane XoY should be obtained first. By substituting equation (4.28) in equation (4.27) and solving for z, the function of the projection can be expressed as:

$$\frac{1}{a^2}X^2 + (\frac{1}{b^2} + \frac{K^2}{C^2})Y^2 + \frac{2k(h+Dk)}{c^2}Y + \frac{(h+Dk)^2}{c^2} - 1 = 0. \tag{4.41}$$

Then the semi-major axis r'_{major} of this projection area can be calculated as [125]:

$$r'_{major} = r_{major} = a\sqrt{\frac{-(h+Dk)^2+c^2+b^2k^2}{c^2+b^2k^2}}, \tag{4.42}$$

After obtaining the semi-minor and semi-major axes of the ellipse δ_1, its area can be calculated as below:

$$S_{\delta_1} = \pi r_{minor} r_{major}, \tag{4.43}$$

thus the volume V_{Δ_δ} of Δ_δ can be achieved by the following integration:

$$V_{\Delta_\delta} = \int_{\gamma}^{\gamma+\Delta\gamma} S_{\delta_1} \frac{r_1+r_2}{2} \frac{\pi}{180} \mathrm{d}\gamma. \tag{4.44}$$

Since we assumed the scatters are uniformly distributed around the MS, the density of the scatters can be obtained as the reciprocal of ellipsoid volume:

$$\rho = \frac{3}{4\pi abc}. \tag{4.45}$$

Using the results, the CDF of the EAoD, $F(\theta)$, can be expressed as:

$$F(\theta) = \int_{0}^{\theta} S_{\delta_1} \frac{r_1+r_2}{2} \frac{\pi}{180} \times \rho \mathrm{d}\theta. \tag{4.46}$$

Then the PDF of the EAoD is the differential of the CDF with respect to θ as $f(\theta) = S_{\delta_1} \frac{r_1+r_2}{2} \frac{\pi}{180} \times \frac{\rho}{f_1(\theta)}$. Then, we can obtain:

$$f(\theta) = \frac{\pi}{240}(1+k^2)\frac{Dc^2-b^2hk}{(b^2k^2+c^2)^{\frac{5}{2}}}\frac{w^2}{f_1(\theta)}. \tag{4.47}$$

where $f_1(\theta)$ is the normalization constant which can be expressed as:

$$f_1(\theta) = \int_{\theta_1}^{\theta_2} \frac{\pi}{240}(1+k^2)w^2\frac{Dc^2-b^2hk}{(b^2k^2+c^2)^{\frac{5}{2}}}\mathrm{d}\theta, \tag{4.48}$$

Thus, the study of the $f(\theta)$ is now reduced to the evaluation of the $f_1(\theta)$. According to $k = -\tan(\alpha - \theta)$, and $d\theta = \frac{dk}{1+k^2}$. The $f_1(\theta)$ can be expressed as:

$$f_1(\theta) = \int_{k_1}^{k_2} \frac{\pi}{240} b^2 h w^2 (\frac{Dc^2}{b^2 h} - k)(b^2 k^2 + c^2)^{-\frac{5}{2}} \mathrm{d}k, \tag{4.49}$$

By using Newton's binomial equation, we can obtain:

$$f_1(\theta) = \frac{\pi b^2 h G}{240} (\frac{M_1 k^{2io+1}}{2i+1} + \frac{M_2 k^{2i+2}}{2i+2} + \frac{M_3 k^{2i+3}}{2i+3} + \frac{M_4 k^{2i+4}}{2i+4})|_{k_1}^{k_2}, \tag{4.50}$$

where,

$$G = \sum_{i=0}^{\infty} \binom{-\frac{5}{2}}{i} c^{-5-2i} b^{2i}, \tag{4.51}$$

and $M_1 = \frac{Dc^4}{b^2 h} - \frac{Dc^2 h}{b^2}, M_2 = -c^2 + h^2 - \frac{2D^2 c^2}{b^2}, M_3 = 2hD + \frac{Dc^2}{h} - \frac{D^3 c^2}{b^2 h}, M_4 = D^2 - b^2$. Equipped with the formulas above, the PDF expression of the EAoD (4.34) can be derived. □

4.2.4 Numerical results

Validation of the theoretical model

To validate the theoretical model, the analytic results and the Monte Carlo simulations are compared. In simulations, the scatterers are uniformly distributed around the MS within the ellipsoid. 10,000 realizations of scatterers are employed to yield the EAoD. The parameters setting are following [109, 126]. In [109], the authors give the distance form BS to MS and the size of scatterers under marcocell environment. In [126], the height of the BS antenna under small cell environment was specified. The parameters used in our simulation are shown in Table 4.2 .

The comparison of the PDF of the EAoD between the theoretical result and the Monte Carlo simulation is illustrated in Fig. 4.14. The comparison shows that these two results closely matches, which proves the effectiveness of our proposed model.

Parameter	Description	Value
D	Distance between BS and MS	50,70m
h	Height of BS	12,20m
a	semi-principal axes of the ellipsoid at X axis	20m
b	semi-principal axes of the ellipsoid at Y axis	10m
c	semi-principal axes of the ellipsoid at Z axis	5m

Table 4.2 Parameter settings of the 3-D experimental scenarios.

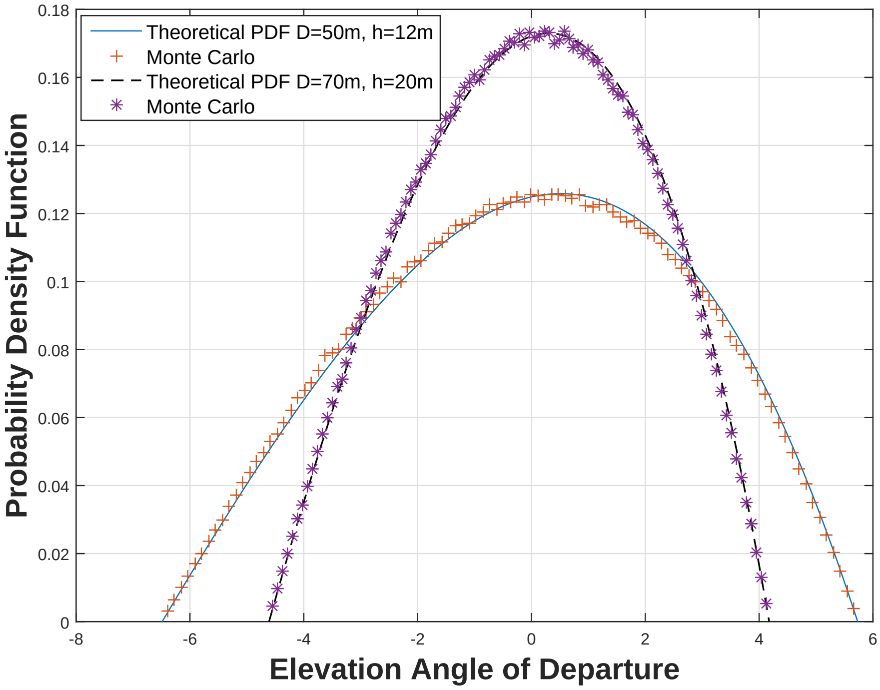

Fig. 4.14 PDF for Theoretical and Monte Carlo under 3-D scenario

Spatial correlation of the proposed model

In this section, the spatial correlation using the proposed PDF is discussed. Considering two linear adjacent BS antennas in the vertical direction, the spatial correction R can be expressed according to the formulations in [116]:

$$R = e^{jkd\sin\theta_0}\int_{-\pi}^{\pi} e^{-jkd\theta\times\cos\theta_0} f(\theta)\mathrm{d}\theta, \tag{4.52}$$

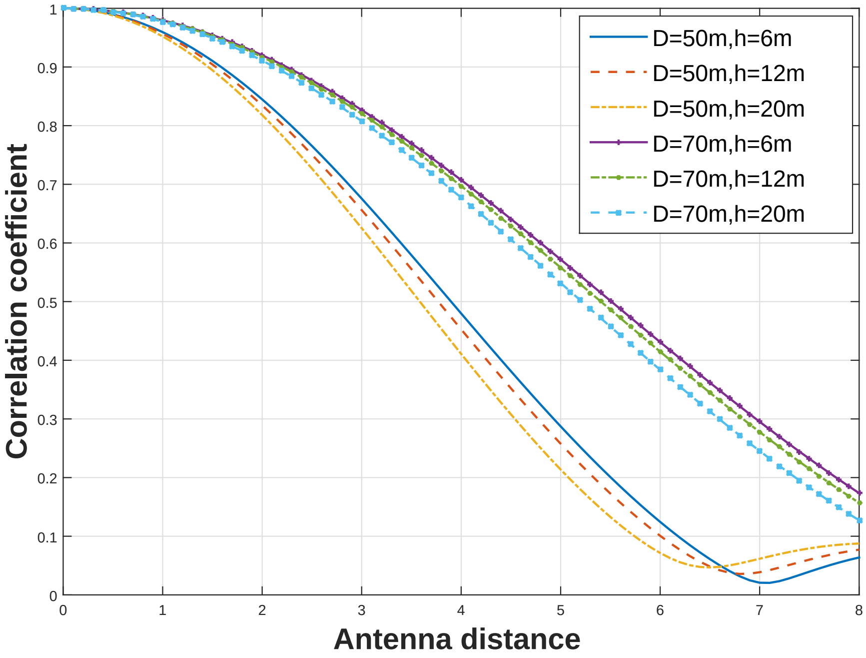

Fig. 4.15 Spatial correction with different antenna distances

where, $k = \dfrac{2\pi}{\lambda}$ is the wavenumber, d is the distance between antennas, and θ_0 is the mean value of the EAoD θ.

The spatial correlation coefficients with different antenna heights are shown in Fig. 4.15. It is observed that with the growth of BS antenna height h while the distance between the BS and the MS D keeps the same, the spatial correlation coefficients decrease gradually. Moreover, when the D increases with the same h, the spatial correlation coefficients increase significantly. Therefore, we conclude that the distance between the BS and MS shows greater influence on the spatial correlation than the BS antenna height.

4.2.5 Conclusion

In this section, a statistical geometric propagation model is proposed for a small cell mobile environment with scatters uniformly located within an ellipsoid around the mobile. The PDF of EAoD is derived in a closed form and validated by Monte Carlo simulation. With the derived

PDF, it is concluded that the spatial correlation coefficients reduce with an increase in the antenna height, and the distance between the BS and MS distinctly affects the spatial correlation.

Chapter 5

Diffuse Scattering in 3-D Ray-Launching

Overview

The millimeter-wave is one of the key technologies for the next generation mobile communication since most bands in low-frequencies have already been allocated. In the millimeter-wave band, the effect of diffuse scattering must be considered during channel modeling because the roughness of the reflection surface can not be ignored compared to the wavelength. In this chapter, the diffuse scattering effect on the millimeter-wave is investigated using typical building structures through measurement. During the measurement, we find that the two-ray propagation mechanism exerts a significant influence on the measurement data processing. Therefore, an algorithm to separate the two referred rays is proposed. With the obtained results, the impact of various materials on diffuse scattering is analyzed. This chapter sheds light on how to take diffuse scattering into account in an RT model.

5.1 Introduction

The predictable rapid increase in indoor mobile data in the future wireless communication will lead to an increase in the operating frequency of the communication system. Because most frequencies in the low-frequency band have already been allocated, the millimeter-wave band, such as 40–50 GHz, is promising in the future wireless network for larger bandwidth allocations

[127]. To thoroughly investigate the millimeter wave, it is essential to have a good understanding of its radio-propagation characteristics. Appropriate indoor channel models are also required to simulate and evaluate a millimeter-wave wireless network.

Over the past decade, the RT and RL channel models have been employed to predict the radio channel for the system design and evaluation [128–131]. For example, in [128], a vertical plane launch technique for approximating a full 3D site-specific ray trace to predict the propagation was proposed. In [129], an RL algorithm was presented to estimate the small-cell system. In [130], the RL tool was used to generate parameters such as signal strength and AoA for all possible paths. In [131], a technique based on collaborative filtering was proposed to improve the RL tool.

In the state of the art RT or RL models, specular reflections are widely used. For each incident ray, the angle of incidence equals the angle of reflection. Meanwhile, the incident, normal, and reflected directions are coplanar following the law of reflection. For specular reflections, a gloss surface must be assumed. In general, it works well at a low-frequency band. However, in the millimeter wave, the surface roughness cannot be ignored because of the reduced wavelength. In the millimeter-wave band, the reflection might be diffused and the electromagnetic waves are scattered away from the surface in a range of directions. Therefore, diffuse scattering, which shows a significant impact on millimeter-wave propagation, should be accounted for in the millimeter-wave channel model.

Recently, the diffuse scatteing effects have been taken into account in RT and RL models [132–135]. In [132], effective roughness diffuse scattering models were proposed and justified by measurement. In addition, different scattering coefficient values were optimised through measurements. In [133], diffuse scattering from rough surfaces in the terahertz band was derived using an RT tool. In [134], the authors proposed a new method to model the channel in straight tunnels with an arch-shaped cross section and that in curved tunnels with a rectangular cross section by using an RL tool. In work [135], the RL tool was used to simulate a typical urban scenario in the WINNER - II, and the results showed that the effect of diffuse scattering at 28 GHz was higher than that at low lower frequencies. Although studies have analyzed the diffuse scattering in RT and RL tools, the impact of using a millimeter-wave, especially the 40—50 GHz band, on the diffuse scattering has not been well understood yet.

In this chapter, to support 3D RL channel modelling, which takes diffuse scattering into account, we investigate the reflection of the millimeter-wave from typical building structures through measurement. More specifically, this chapter makes the following contributions. First, we introduce the mechanism of diffuse scattering in a millimeter wave and introduce how to use it in an RL tool. Then, the reflection of the 40–50 GHz millimeter-wave band from typical building structures is measured. Finally, using the measurement results, the impact of various materials on the scattering lobe is analysed. This chapter sheds light on how to take defuse reflection into account in an RL channel model.

The remainder of this chapter is organized as follows. In section 5.2, we briefly introduce the mechanism of diffuse scattering, and the reflection ray generation in 3-D RL is described in section 5.3. In section 5.4, we present the experiment setup and some measurements conducted under various materials. The simulation results are presented in section 5.5, and finally, the conclusions are drawn in section 5.6.

5.2 Diffuse Scattering

In the millimeter-wave band, the effect of diffuse scattering must be considered during channel modelling because the roughness of the reflection surface cannot be ignored as compared to the wavelength. Diffuse scattering refers to the scattering of signals in several directions rather than a particular direction, as illustrated in Fig. 5.1.

Assuming that the power of diffuse scattering is concentrated in the direction perpendicular to the scattering direction, the scattering power can be calculated using the well-known Lambertian model [137]:

$$E_s^2 = E_{s0}^2 \times \cos(\theta_s). \tag{5.1}$$

where E_s indicates the norms of the scattered field, E_{s0} indicates the field in the vertical direction of the wall, and θ_s is the angle of scattering. Basically, the scattering power should satisfy the

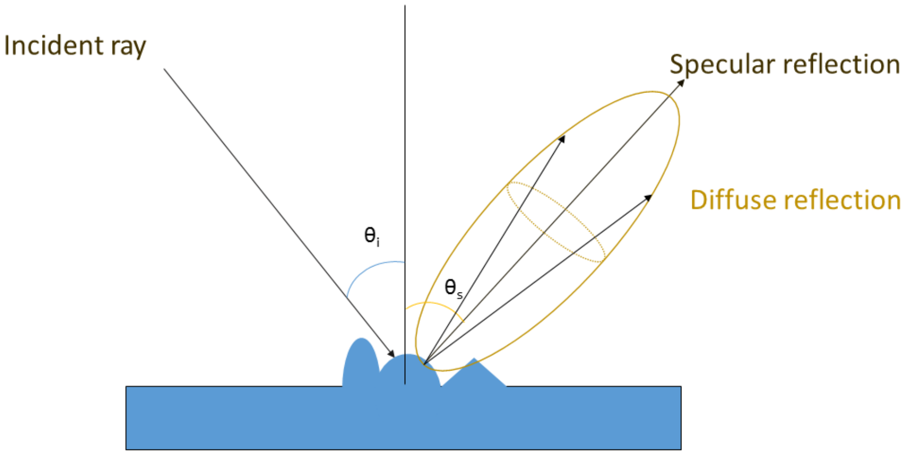

Fig. 5.1 Diffuse Scattering.

scattering power balance [137]:

$$S^2 E_i^2 \Delta_\Omega r_i^2 = \int_0^{\frac{\pi}{2}} \int_0^{2\pi} E_s r_s^2 \sin(\theta_s) d\theta_s d\varphi, \tag{5.2}$$

where S is the scattering coefficient, E_i indicates the norms of the incident field, and Δ_Ω is the AoD impinging on the scattering surface. r_i and r_s represent the distance from the scattering to transmitter antenna and receiver antenna, respectively.

According to the expression in [138], E_{s0} can be expressed as:

$$E_{s0} = (\frac{K \times S}{r_i \times r_s})^2 \frac{\delta_s \cos(\theta_i)}{\pi}. \tag{5.3}$$

where K is a constant depending on the amplitude of the impinging wave, and δ_s and θ_i indicate the areas of scattering and the angle of incidence, respectively.

For the directive model, it is assumed that the maximum power of the scattering rays is the specular reflection ray.

$$E_s^2 = E_{s0}^2 (\frac{1 + \cos(\xi_R)}{2})^\alpha. \tag{5.4}$$

where, E_{s0} is the specular reflection field and ξ_R is the angle between the specular reflection ray and other scattering rays. α represents the width of the scattering lobe, which is an adjustable variable under different scenarios. Similar to equation (5.3), E_{s0} can be represented as:

$$E_{s0} = (\frac{K \times S}{r_i \times r_s})^2 \frac{\delta_s \cos(\theta_i)}{F_\alpha}. \tag{5.5}$$

and

$$F_\alpha = \frac{1}{2^\alpha} \sum_{\eta=0}^{\alpha} \binom{\alpha}{\eta} I_\eta. \tag{5.6}$$

,

$$I_\eta = \frac{2\pi}{\eta+1} [\cos(\theta_i) \sum_{\beta=0}^{\frac{\eta-1}{2}} \binom{2\beta}{\beta} \times \frac{\sin^{2\beta}(\theta_\eta)}{2^{2\beta}}]^{(\frac{1-(-1)^\eta}{2})}. \tag{5.7}$$

As seen in the equation (5.4), the power of diffuse scattering is mainly determined by the specular reflection field, the angle of scattering and the parameter α, which indicates the scattering lobe. Therefore, we conduct an experiment to investigate these values in this chapter.

An important phenomenon that needs to considered in the millimeter-wave diffuse scattering model is the resonant phenomenon caused by multiple reflections and transmissions, as shown in Fig. 5.2. As we can see in Fig. 5.2, the specular reflection mainly comprises a single reflection ray and multiple reflection rays. For researching the best connection between the single reflection ray and the diffuse scattering rays, the effect of the multiple reflection rays needs to be deleted. Because the second reflection 2 ray (Fig. 5.2) dominates the power in multiple reflection rays, we mainly delete the effect of the second reflection ray. Therefore, the proposed algorithm is introduced here. First, the field of the single reflection ray with the second reflection ray can be expressed as:

$$S_{21} = \Gamma_1 \exp(j\omega t) + \Gamma_2 \exp[j\omega(t+\Delta t)], \tag{5.8}$$

where $\Gamma_1 \exp(j\omega t)$ indicates the field of the single reflection ray and $\Gamma_2 \exp[j\omega(t+\Delta t)]$ is indicates the second reflection rays. Γ_1 and Γ_2 are the received amplitudes of the first and the second rays, respectively, while Δt is the phase caused by the difference in the path lengths.

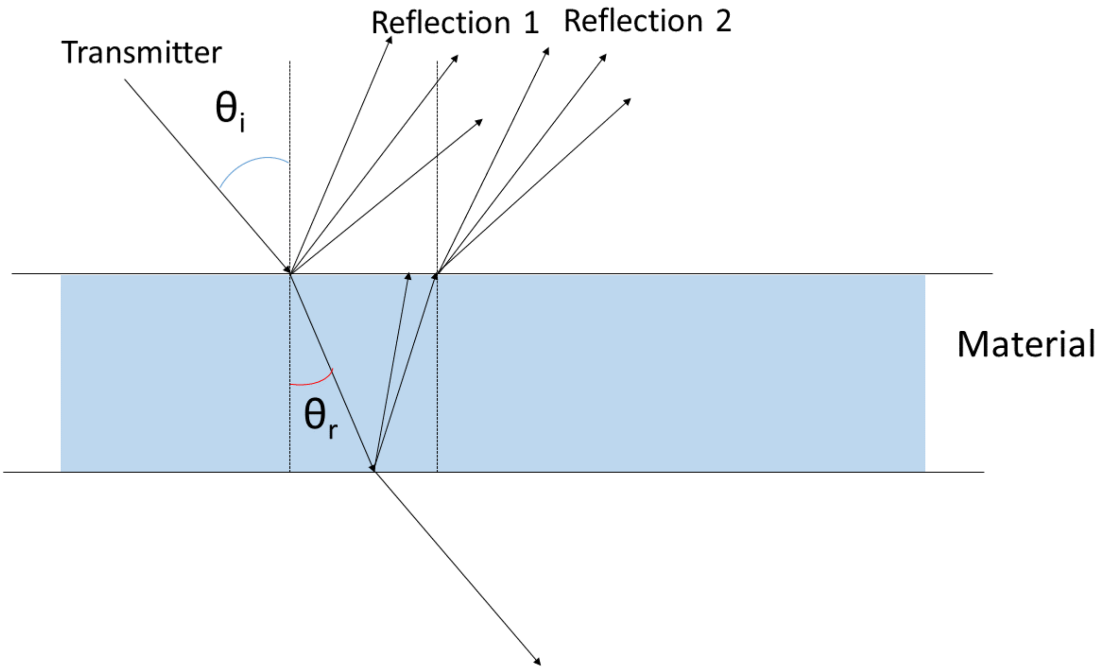

Fig. 5.2 Multiple reflections and transmissions.

It is observed that the final results of the reflection rays are determined by the power of the single reflection ray, the power of the multiple reflection rays, and the phase shift. An objective of this chapter is to empirically model the first ray through measurement.

5.3 Reflection Ray Generation in 3-D Ray Launching

This subsection discusses the issues concerning the implementation of the reflection ray generation in a 3-D RL channel model while considering diffusion scattering. In an RL channel model, the rays are computed from the emitter. Basically, when the ray hits the blockage building structure, a specular reflection ray is generated. However, taking diffusion scattering into account, multiple rays are generated for one reflection.

Owing to the irregularities of a flat layer, the diffuse scattering rays will are extended into 3D space, as shown in Fig. 5.3. In 3-D space, the parameter α determines the scattering lobe, which mainly affects the angle modelling in a millimeter-wave channel model. As long as the relation between α and frequency is empirically modelled through measurements, the 3D diffuse

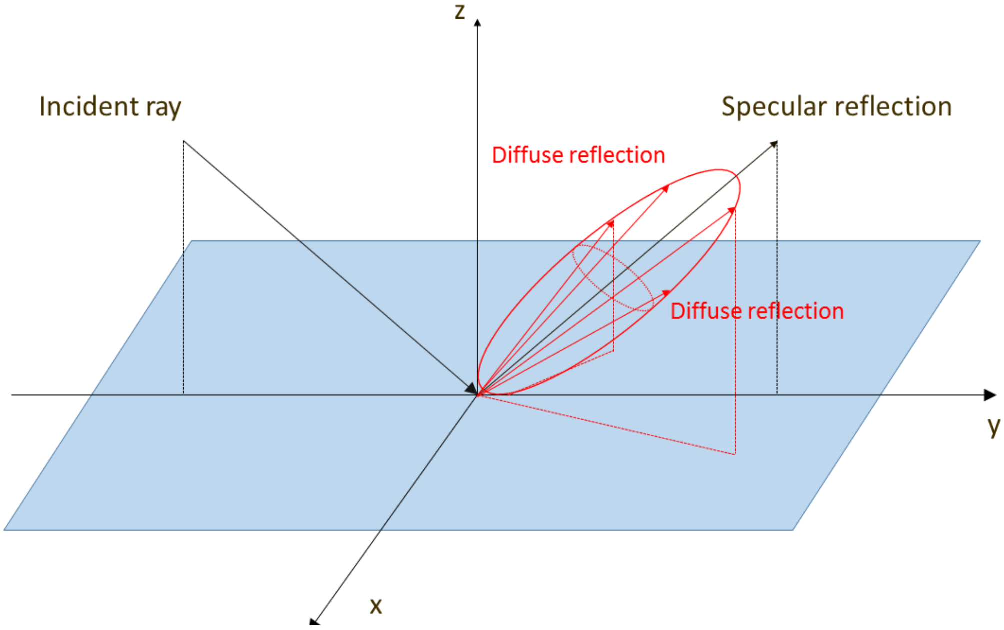

Fig. 5.3 3-D diffuse scattering.

scattering rays can be generated in the RL tool.

Assuming that n scatter rays are generated in one reflection, first, parameters in (5.4), i.e., α and E_{s0} are generated through a measurement-based empirical model. Second, the reflection point is considered as a transmit antenna and creates an array of $n-1$ independent and identically distributed (i.i.d.) random scatter rays, with a PAS of (5.4). Third, the n generated rays are emitted to continue the simulation of the RL model.

5.4 Measurement

In order to investigate the diffuse scattering, especially the parameter α in (5.4), the power of the specular reflection and the power of the other rays moving towards the specular reflection, which indicate diffuse scattering, need to be determined. Therefore, we establish a measurement system and measure the diffusion properties under typical materials of building structures. In this section, the measurement is introduced.

Woodenboard Plasterboard Granite

Fig. 5.4 Involved materials

5.4.1 Equipment and materials

A Vector network analyzer (VNA) based measurement system is established in this section which is employed to measure the S_{21} parameter of the transmission channel via the reflection of the involved materials.

Two horn-direction antennas with high gains are connected to the VNA via cables to transmit and receive radio frequency signals. With high directionality, the antennas efficiently reduce the interference caused by the unwanted direction. A laptop is used to collect and analyse the data obtained from the VNA.

Various materials are used to retrofit the indoor environment. In this study, typical materials of building structures, i.e., woodenboard, plasterboard, and granite, are considered. A photograph of the referred materials is shown in Fig. 5.4, and their sizes are shown in Table 5.1.

5.4.2 Measurement procedure

The measurement campaign is conducted under an indoor corridor scenario on the fifth floor of the YIFU building, Chongqing University of Posts and Telecommunications (CQUPT), as

Materials	length (cm)	width (cm)	thickness (cm)
Woodenboard	121.5	80.7	1.68
Plasterboard	119.8	79	0.90
Granite	76.8	42	1.52

Table 5.1 Size of involved materials.

Fig. 5.5 measurement campaign.

Fig. 5.6 Measurement setup scheme.

shown in Fig. 5.5. A scheme schematic of the measurement setup is shown in Fig. 5.6. The antennas are connected to the VNA through cables with loss of 20 dB at 45 GHz. The VNA plus cables are calibrated by using the short, open, load, and through (SOLT) standards. During each measurement, the antennas are mounted on tripods and kept at fixed locations to ensure consistent measurement conditions for all the construction materials; meanwhile, the height and polarization of the antennas are adjustable. For each material, we conduct the measurement at the 40 GHz—50 GHz bands with an interval of 0.025 GHz. The angles of the Tx transmitting antenna are 60°, and 75°, as illustrated in Fig. 5.7. The position of Rx receiving antenna is located at 15° away from both sides of the specular reflection angle. In order to satisfy the far-field condition, the distance between the antennas and the scattering position is 50 cm, which leads to a path loss.

Examples of the measured S_{21} parameters are given in Figs. 5.8, 5.9, 5.10, and 5.11. In Figs. 5.8 and 5.9, the material is woodenboard and the incident angles are 60° and 75°, respectively. In Figs. 5.10 and 5.11, we perform the measurements under plaster and granite materials at an incident angle of 75°. Theoretically, the power of the specular reflection ray should be the

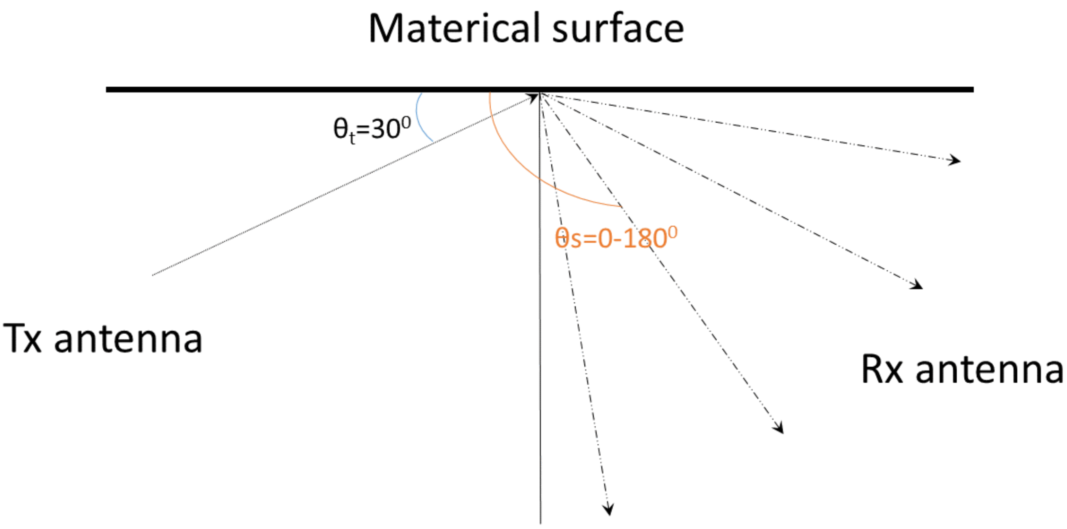

Fig. 5.7 Illustration of the reflected signal measurement procedure.

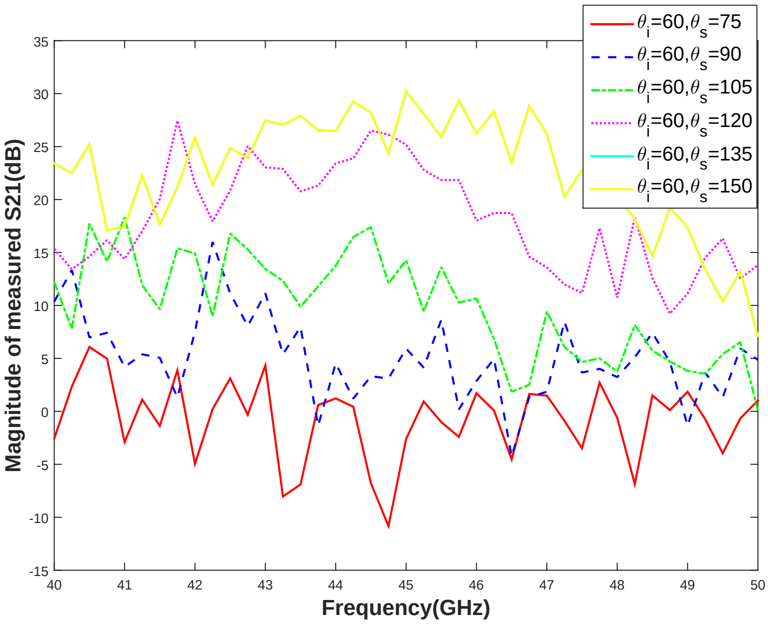

Fig. 5.8 Example of measured S_{21} via wooden board reflection, the incident angle is 60°.

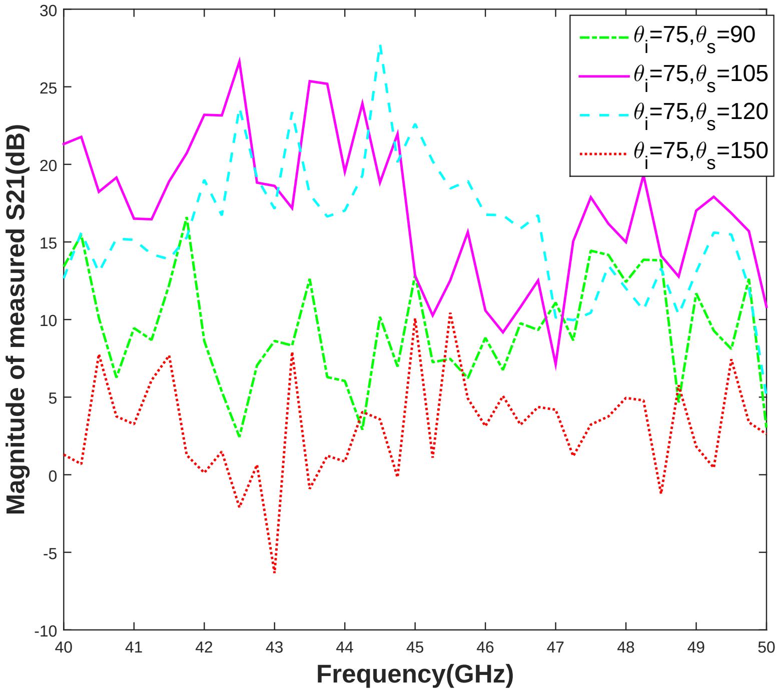

Fig. 5.9 Example of measured S_{21} via wooden board reflection, the incident angle is 75°.

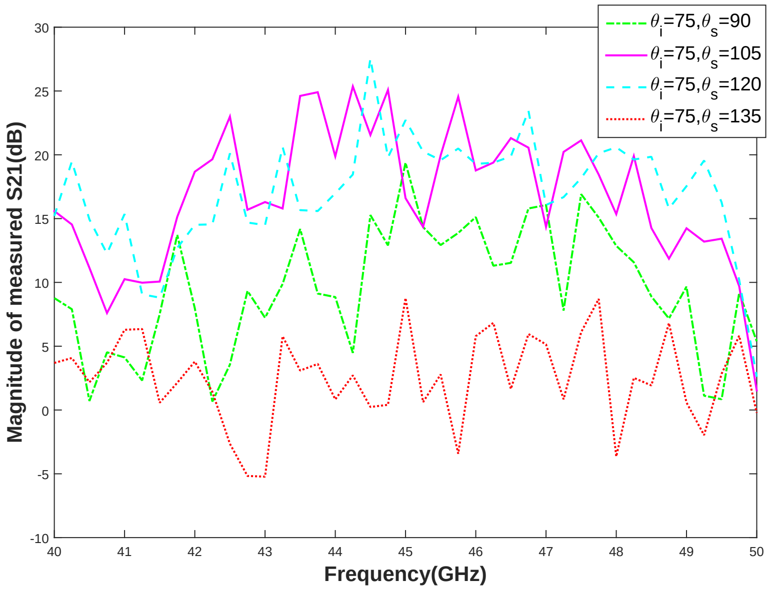

Fig. 5.10 Example of measured S_{21} via plasterboard reflection, the incident angle is 75°.

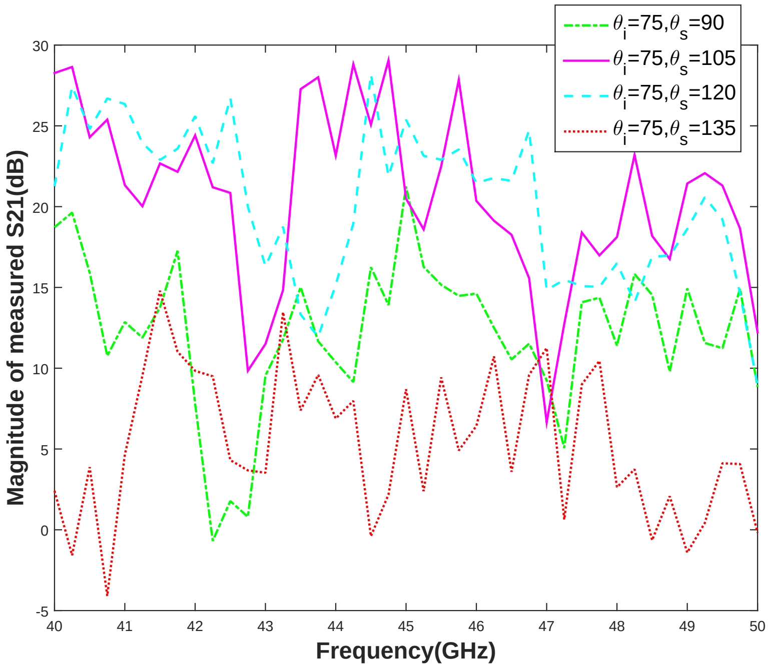

Fig. 5.11 Example of measured S_{21} via granite reflection, the incident angle is 75°.

biggest one among the diffuse scattering rays. Meanwhile, the equation (5.4) indicates that the power of the scattering ray decreases when the ray farther away with the specular reflection ray. However, these figures indicate that the power of the specular reflection ray is not always larger than that of other rays, such as the magenta line ($\theta_i = 75, \theta_s = 105$) in Fig. 5.10. Therefore, it is observed that the deep fading in the measurement due to the two-ray model shown in Fig. 5.2 must be taken into account.

5.4.3 Reflection rays separation

The two-ray propagation mechanism introduces challenges on measurement data processing if the materials are in the shape of a thin board. In a practical measurement, if the measured material is in the shape of a thin board, the two rays are very difficult to separate. For example, even if the measurement bandwidth is as large as 10 GHz, the resolution of Δt is 0.1 ns and the minimum resolvable distance in air is 3 cm, which is comparable to the thickness of the involved material. Therefore, an algorithm for separating the two referred rays is given as follows.

First, the power of the single reflection ray with the second reflection ray can be derived as:

$$\begin{aligned} |S_{21}|^2 &= |\Gamma_1 \exp(j\omega t) + \Gamma_2 \exp[j\omega(t+\Delta t)]|^2 \\ &= |\Gamma_1 + \Gamma_2 \exp[j\omega(\Delta t)]|^2 \end{aligned} \tag{5.9}$$

where, Γ_1, Γ_2 are the amplitudes of the single reflection ray and second reflection ray. Δt is the time difference between the single reflection ray and second reflection ray.

Finally, since the average of the phase shift of the multiple reflection rays is equal to 0, the following equation can be obtained:

$$|S_{21}|^2 = |\Gamma_1|^2 + |\Gamma_2|^2 + 2|\Gamma_1||\Gamma_2|[\cos(\omega\Delta t + \phi)]. \tag{5.10}$$

where, ϕ is the phase shift of the single reflection ray and second reflection ray. Since the field of the ray is almost reciprocal linearly correlated with the frequency, we can assume that $|\Gamma_1| = \gamma_1/\omega, |\Gamma_2| = \gamma_2/\omega$. where γ_1 and γ_2 are unknown constants. Therefore, the following equation can be obtained by multiplying ω^2 on both sides of the above expression:

$$|S_{21}|^2\omega^2 = \gamma_1^2 + \gamma_2^2 + 2\gamma_1\gamma_2\cos(\omega\Delta t + \phi) + P_m. \tag{5.11}$$

where P_m is the error introduced by multipath.

In order to extract γ_1 from the measured S_{21} function, we propose a minimum Euclidean distance estimator (MEDE) algorithm, whose basic mechanism is to conduct subspace estimation by minimizing the mean square distance between the actual value and the estimated value:

$$\begin{aligned} &[\hat\gamma_1, \hat\gamma_2, \Delta\hat t, \hat\phi] = \arg\min \left\|\hat\gamma_1^2 + \hat\gamma_2^2 + 2\hat\gamma_1\hat\gamma_2\cos(\omega\Delta\hat t + \hat\phi) - |S_{21}|^2\omega^2\right\|^2 \\ &= \arg\min \left\|\hat\gamma_1^2 + \hat\gamma_2^2 - \gamma_1^2 - \gamma_2^2 + 2\hat\gamma_1\hat\gamma_2\cos(\omega\Delta\hat t + \hat\phi) - 2\gamma_1\gamma_2\cos(\omega\Delta t + \phi) + P_\mathrm{m}\right\|^2 \end{aligned} \tag{5.12}$$

where, $\hat\gamma_1$, $\hat\gamma_2$, $\Delta\hat t$ and $\hat\phi$ are the fitting values of the γ_1, $/\gamma_2$, Δ and ϕ respectively. Owing to the expensive computation of this equation, we estimate $[\hat\gamma_1, \hat\gamma_2]$ and $[\Delta\hat t, \hat\phi]$ separately using our MEDE algorithm.

Step 1: We estimate the $[\Delta\hat{t},\hat{\phi}]$ first. Here, assuming $\hat{\gamma}_1 \approx \gamma_1$ and $\hat{\gamma}_2 \approx \gamma_2$. Thus, we can obtain:

$$[\Delta\hat{t},\hat{\phi}] = \arg\min \left\| \gamma_1^2 + \gamma_2^2 + 2\gamma_1\gamma_2\cos(\omega\Delta\hat{t} + \hat{\phi}) - |S_{21}|^2\omega^2 \right\|^2 . \tag{5.13}$$

As we known that:

$$\int_{2\pi\times 40GHz}^{2\pi\times 50GHz} \cos(\omega\Delta t + \phi) d\omega \approx 0 \tag{5.14}$$

. Therefore,

$$\int_{2\pi\times 40GHz}^{2\pi\times 50GHz} \left(2\hat{\gamma}_1\hat{\gamma}_2\cos(\omega\Delta\hat{t} + \hat{\phi}) - 2\gamma_1\gamma_2\cos(\omega\Delta t + \phi)\right) \mathrm{d}\omega \approx 0, \tag{5.15}$$

and

$$\int_{2\pi\times 40GHz}^{2\pi\times 50GHz} \cos^2(\omega\Delta\hat{t} + \hat{\phi}) \mathrm{d}\omega \approx \int_{2\pi\times 40GHz}^{2\pi\times 50GHz} \cos^2(\omega\Delta t + \phi) \mathrm{d}\omega \approx \pi \times 10^{10}. \tag{5.16}$$

Therefore, the formulation (5.13) can be derived as:

$$[\Delta\hat{t},\hat{\phi}] = \arg\min\{(\gamma_1^2 + \gamma_2^2 - |S_{21}|^2\omega^2)^2 + (2\gamma_1\gamma_2\cos(\omega\Delta t + \phi))^2 + \\ \int_{\omega} (\gamma_1^2 + \gamma_2^2 - |S_{21}|^2\omega^2)(2a_1a_2\cos(\omega\Delta t + \phi \tag{5.17}$$

Ignoring the constant terms, we can obtain:

$$[\Delta\hat{t},\hat{\phi}] = \arg\min\left\{ \int_{\omega} \left[\gamma_1^2 + \gamma_2^2 - |S_{21}|^2\omega^2\right] \left[2\gamma_1\gamma_2\cos(\omega\Delta\hat{t} + \hat{\phi})\right] \mathrm{d}\omega \right\}. \tag{5.18}$$

Then, substituting (5.15) and (5.16) into (5.18), we obtain:

$$[\Delta\hat{t},\hat{\phi}] = \arg\max \textstyle\int_{\omega} |S_{21}|^2\omega^2\cos(\omega\Delta\hat{t} + \hat{\phi}) \tag{5.19}$$

After the measurement, the $[\Delta\hat{t},\hat{\phi}]$ can be obtained by an exhaustively search.

Step 2: After substituting $[\Delta\hat{t},\hat{\phi}]$ into equation (5.13), $[\hat{\gamma}_1,\hat{\gamma}_2]$ can be estimated through the

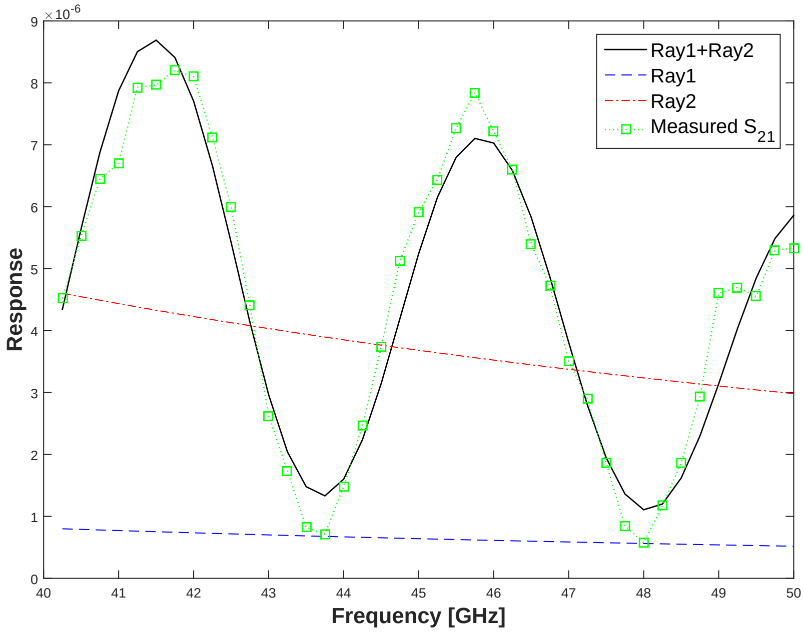

Fig. 5.12 Two-ray separation with an incident angle of 60°, and a reflection angle of 120°.

MED principle. Then, the response of the reflection ray is obtained as $\frac{\gamma_1}{\omega}\exp(j\omega t)$.

Examples of two-ray separation are proposed in Figs. 5.12, 5.13, and 5.14, where the granite is considered. The incident angle is 60° and the reflection angle is 120°. It is observed that the combination of the separated rays matches the measured S_{21} parameter very well, and the separation is validated. In the following analysis, the first ray for each reflection angle is evaluated as the reflection signal.

5.5 Measurement Results

5.5.1 Parameter estimation

With the fitting results in Fig. 5.12, 5.13 and 5.14, the γ_1 shown in equation (5.11) can be obtained:

$$S_{21} = \frac{\gamma_1}{\omega} exp(j\omega t), \tag{5.20}$$

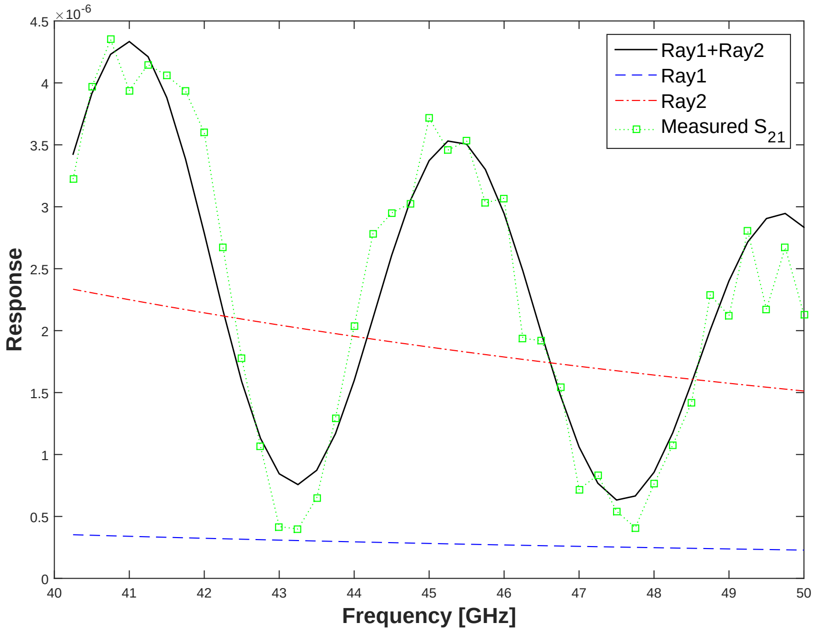

Fig. 5.13 Two-ray separation with an incident angle of 60°, and a reflection angle of 105°.

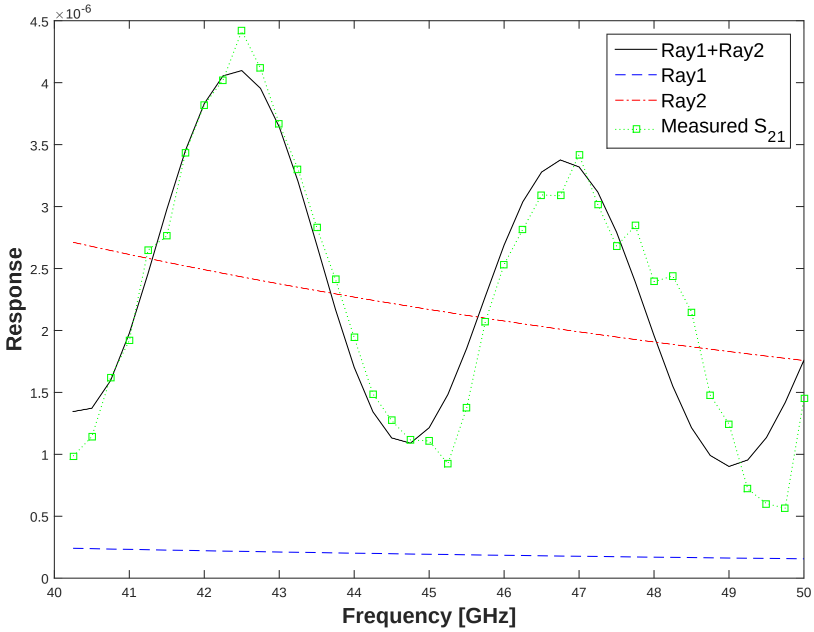

Fig. 5.14 Two-ray separation with an incident angle of 60°, and a reflection angle of 135°.

Therefore, substituting equation (5.20) into equation (5.4) and taking the pathloss into account, we can obtain:

$$\left(\frac{\gamma_1(\xi_R)}{\omega}\right)^2 L = E_{s0}^2 \left(\frac{1+\cos(\xi_R)}{2}\right)^\alpha, \tag{5.21}$$

Because the distance between both antennas and the scattering position at the material surface is 50 cm in our measurements, we denote L the pathloss of the measurement link with a length of 1m.

To eliminate the effect of the pathloss in our measurement, the specular reflection ray (ξ_R was set to be 0) is considered. Then the following equation can be gained:

$$\gamma_1^2(0) = \frac{\omega^2 E_{s0}^2}{L}, \tag{5.22}$$

Therefore, we can have:

$$\gamma_1^2(\xi_R) = \gamma_1^2(0)(\frac{1+\cos(\xi_R)}{2})^\alpha, \tag{5.23}$$

Finally, taking logarithm at both sides of equation (5.23), the estimator of parameter α is expressed as:

$$\alpha = \frac{2\ln\left(\frac{\gamma_1(\xi_R)}{\gamma_1(0)}\right)}{\ln\left(\frac{1+\cos(\xi_R)}{2}\right)}. \tag{5.24}$$

5.5.2 Results and discussion

Fitting the α at 60° and 75° under plasterboard material, Fig. 5.15 can be drawn.

Then with the same research steps to investigate the woodenboard and plasterboard materials. The relationship between the fitting value α and the incident angle can be obtained from Table 5.2.

In this table, -15° and 15° represent the scattering angles away from both sides of the specular reflection angle (60° and 75°). As seen from the table, the fitting values of α always vary from 30 to 70. Moreover, the average value of α is in the order woodenboard $>$ granite $>$ plasterboard. This phenomenon maybe caused by the different materials' surfaces: the surface of the wooden material is the roughest, while that of the plasterboard material is the smoothest.

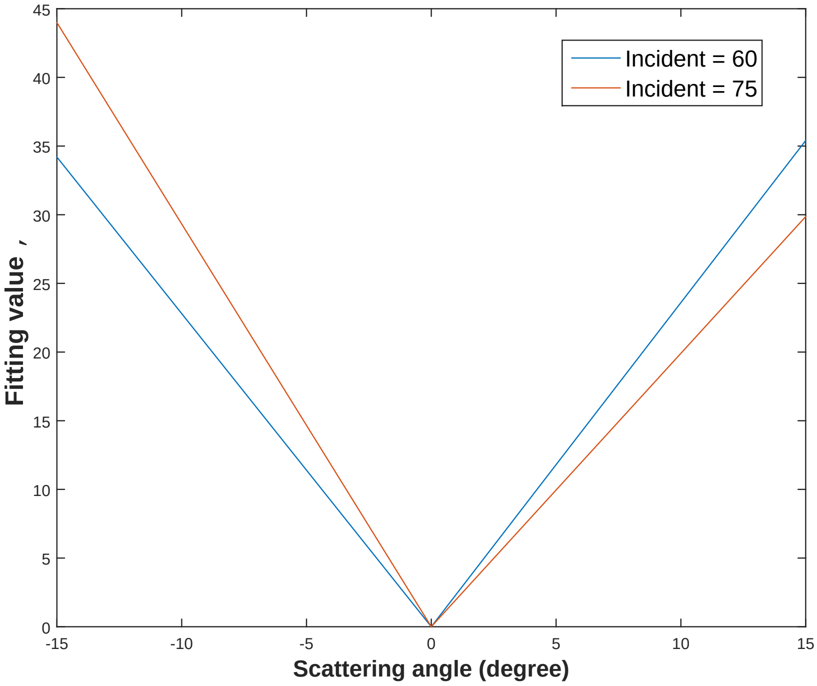

Fig. 5.15 Fitting value under plasterboard material.

Reflection angle Material	Incident 60°		Incident 75°	
	$-15°$	$+15°$	$-15°$	$+15°$
Plasterboard	34.2	35.4	43.99	29.86
Wooden board	32.85	69.52	50.95	42.53
Granite	39.4	30.79	59.96	34.5

Table 5.2 Fitting values under various materials

5.6 Conclusion

In this chapter, first, the mechanism of the diffuse scattering is introduced and the reflection ray generation in 3D RL is given first. Then, we proposed an algorithm to separate the two referred rays when performing the measurement. With the proposed algorithm, some measurements are executed to obtain the diffuse properties, especially the scattering lobe parameter α under typical materials of buildings structures. Some notable results on the relationship between the fitting value of α and the incident angle are gained. We find that the α always varies between 30 to and 70. With the obtained values, the power of the diffuse scattering rays can be calculated and used to generate the diffuse scattering in 3-D RL. We also conclude that the roughness, width, and permittivity of the materials significantly affect the diffuse properties, which we will investigate in our future work.

Chapter 6

Conclusions and Future Work

6.1 Conclusions

In this thesis, the small cell and millimeter-wave channel modeling were mainly investigated. First, the elevation angle in the 3-D channel model was researched under some typical street scenarios. Then, closed-form expressions of the PDF of the EAoD are derived and verified with two scattering models. Finally, the diffuse scattering effect on the millimeter-wave are investigated with typical building structures.

In chapter 2, the impact of antenna height on EAoD and EAoA is investigated under typical outdoor scenarios: straight street, fork road, and crossroad. In order to research the PDF of the EAoD and the EAoA, the IRLA was introduced and used to simulate angle problem under different scenarios. The closed-form expressions of the PDF of EAoD and EAoA together with the related AS and DS were derived under various street scenarios. According to the results, we conclude that the PDFs of EAoD and EAoA are modelled as exponential functions whose parameters are observed as a linear function of the antenna height under the straight street scenario. Another conclusion we can obtain is that in the forked road and crossroad scenarios, the characteristics of EAoD and EAoA change significantly when the BS antenna height is half of the building's height. Moreover, according to the results of the AS and the DS, we conclude that the BS antenna should be deployed at half of the building's height if we want to obtain the maximum or minimum value of the AS and the DS under the three typical street scenarios.

Then in chapter 3, due to the importance of the elevation angle in small cell channel modeling, an elevation angle model was proposed for the small cell environment by using GBSB method. Two scattering models are discussed in this chapter. For the first mode, it is assumed that the scatterers are located uniformly within an ellipse around the mobile. We derive the expression of the PDF of the EAoD and verify it by using the Monte Carlo simulation. The impact of parameters including the distance between the BS and MS, the BS height and the size of the scatterers on the distribution of EAoD have also been analysed. With the results, we conclude that the distance between the BS and MS together with the height of scatterers at vertical plane significantly affect the PDF of the EAoD. Then, the spatial correlation using the proposed PDF are also presented. We find that the distance between the BS and MS together with the height of the scatterers show greater influence on the spatial correlation. For the second mode, a statistical geometric propagation model is proposed for a small cell mobile environment with scatterers uniformly located within an ellipsoid around the mobile. The PDF of the EAoD is derived in closed-form and validated by Monte Carlo simulation. With the derived PDF, we conclude that the spatial correlation coefficients have similar characteristics as the first model.

At last, the millimeter-wave channel model is investigated after researching the small cell channel model. We introduce the mechanism of the diffuse scattering and the reflection ray generation in 3-D RL first. To best understanding the effect of the diffuse scattering on the millimeter-wave, some measurements are executed. During the measurements we find that the two-ray propagation mechanism show great influence on the measurement data processing. Therefore, an algorithm is developed to separate the referred two rays when doing the measurement. Some notable results about the relationship between the scattering lobe parameters α and the incident angle are gained. It is conclude that the α always varied between 30 to 70. With the results, the power of the diffuse scattering rays can be calculated and used to generate the diffuse scattering in 3-D RL. This method shed light on how to take defuse scattering into account in an RL model.

6.2 Future Work

For future work, some remaining problems and potentials of improvement are existed in our works.

The future work for chapter 3 is list as follow:

- The results are obtained when the BS was located at the center of the street scenarios. However, this BS location is unrealistic in practice which can be improved in the future.

- In the three typical street scenarios, more parameters in channel modeling can be researched except PDF of EAoD and EAoA, AS and DS. Such as the reflection coefficient, the diffuse coefficient and etc..

- The methods can be applied in some complex scenarios, such as the train station, airport, football field and etc..

- The IRLA need to be developed under different frequencies, especially under high frequencies like millimeter-wave.

- During the simulations in this chapter, we always assume the buildings on both sides of the street have the same height. This can be improved because the heights of the building are different in practice.

- Besides, the researches in chapter 3 are achieved by assuming that the antenna type is omni-directional. In our future works, the PDFs of EAoD and EAoA with different antenna patterns and tilt will be considered under typical outdoor scenarios.

The future work for chapter 4 is list as follow:

• As shown in Chapter 4, the PDFs of the EAoD are derived with the assumption that the scatters are located around the MS as an ellipse or elliptical. These assumptions are valid under some typical small cell scenarios. However, with the complexity of small cell environments, more specific scattering models should be considered.

• The distribution of the horizontal angle of departure and arrival in the 2-D and 3-D scenarios can be researched. Meanwhile, the correlation between the horizontal angle and elevation angle can also be studied.

• The antenna type in chapter 4 is regarded as omni-directional. However, with different antenna types, the distribution of the elevation angle will be different which can be researched in the future.

• Besides, with the derived PDFs, more channel characteristics such as the capacity, coverage and density can be obtained.

The future work for chapter 5 is list as follow:

• As can be seen in Chapter 5, the measurements are conducted with the frequency band from 40 GHz to 50 GHz. With the improvement of the measure equipments, more frequency bands can be measured in the future.

• During the measurements, the distance between the antenna and the scattering material is fixed. Actually, due to the high signal propagation loss for millimeter-wave, the distance between the antenna and the scattering material show great effect on the diffuse scattering.

• More materials can be measured, such as plastic, glass, iron and etc..

- More characteristics of millimeter-wave need to be researched except the diffuse scattering.

- Besides, we conclude that the roughness, width, and the permittivity of the materials significantly affect the diffuse properties which we will investigate in our future work.

References

[1] J. G. Andrews, H. Claussen and M. Dohler, , “Femtocells: past, present, and future,” *IEEE J. Sel. Areas Commun.*, vol. 30, pp. 497-508, 2012.

[2] C. Dehos, etc., “ Millimeter-wave access and backhauling: the solution to the exponential data traffic increase in 5G mobile communications systems?” *IEEE Commun. Mag.*, vol. 52, pp. 88-95, 2014.

[3] I. Hwang, B.y. Song, and S. Soliman, “A holistic view on hyper-dense heterogeneous and small cell networks,” *IEEE Commun. Mag.*, vol. 51, pp. 20-28, 2013.

[4] V. Chandrasekhar, J. G. Andrews, A. Gatherer, “Femtocell networks: a survey,” *IEEE Commun. Mag.*, vol. 8, pp. 59-67, 2008.

[5] T. Nakamura, etc., “Trends in small cell enhancements in LTE advanced,” *IEEE Commun. Mag.*, vol. 51, pp. 98-105, 2013.

[6] P. Smulders, “ Exploiting the 60 GHz band for local wireless multimedia access: prospects and future directions,” *IEEE Commun. Mag.*, vol. 40, pp. 140-147, 2002.

[7] ITU-R, “ Attenuation by Atmospheric Gases.”Approved in 2016-09-30

[8] C.-X. Wang, M. Pätzold, and Q. Yao,“ Stochastic modeling and simulation of frequency correlated wideband fading channels,” *IEEE Trans. Veh. Technol.*, vol. 56, pp. 1050-1063, 2007.

[9] I. Telatar, “ Capacity of multi-antenna gaussian channels,” *European Trans. on Telecommunications,*, vol. 10, pp. 585-595, 1999.

[10] A. J. Paulra, D. A. Gore and R. U. Nabar, “ An Overview of MIMO Communications—A Key to Gigabit Wireless,” *Proc. IEEE*, vol. 92, pp. 198-218, 2004.

[11] H. Sawada, Y. Shoji and C.S. Choi, “ Proposal of novel statistic channel model for millimeterwave WPAN,” *IEEE APMC.*, pp. 1855-1858, 2006.

[12] N. Guo, R. C. Qiu, and M. Shao, “ 60-GHz Millimeter-wave radio: principle, technology, and new results,” *EURASIP journal on Wireless Communications and Networking*, vol. 1, pp. 48-48, 2007.

[13] D. Solomitckii, “ Characterizing the impact of diffuse scattering in urban millimeter-wave deployments,” *IEEE Wireless Commun. Lett.*, vol. 5, pp. 432-435, 2016.

[14] C. X. Wang, etc.,“ Cooperative MIMO channel models: a survey,” *IEEE Commun. Mag.*, vol. 48, pp. 80-87, 2010.

[15] J. Robson, “ Small cell backhaul requirements,” NGMN Alliance. white Paper, 2012.

[16] A. H. Jafari, D. L´opez P´erez, and J. Zhang, “ Small cell backhaul: challenges and prospective solutions,” *IEEE Communications Surveys and Tutorials*, 2004.

[17] J. Robson and L. Hiley, “ Easy small cell backhaul: an analysis of small cell backhaul requirements and comparison of solution,” *Cambridge Broadband Networks Limited*, white Paper, 2012.

[18] J. Hoydis, M. Kobayashi, M. Debbah, “ Green Small-cell Networks,” *IEEE Commun. Mag.*,vol. 6, pp. 37-43, 2011.

[19] H. H. Meinel, “ Automotive Millimeterwave Radar History and present Status,” *IEEE 28th European Microwave Conference*, vol. 1, pp. 619-629, 1998.

[20] N. Patwari and P. Agrawal, “ Nesh: a joint shadowing model for links in a multi-hop network ,” *IEEE ICASSP.*, pp. 2873-2876, 2008.

[21] P. Adhikari, “ Understanding millimeter wave wireless communication,” *Millimeter Wave Wireless Communication*, white Paper, 2008.

[22] H. H. Meinel, “ Commercial applications of millimeterwaves: history, present status, and future trends,” *IEEE Trans. on Micro. Theory and Tech.*, vol. 43, pp. 1639-1653, 1995.

[23] R. Jain, “ Channel Models: A Tutorial,” *WiMax Forum*, vol. 1, pp. 1-21, 2007.

[24] H. Sun, A. Nallanathan, C. X. Wang, “ Wideband spectrum sensing for cognitive radio networks: a survey,” *IEEE Wireless Commun. Mag.*, vol. 20, pp. 74-81, 2013.

[25] P. Almers, etc., “ Survey of Channel and Radio Propagation Models for Wireless MIMO Systems,” *EURASIP Journal on Wireless Communications and Networking*, vol. 1, pp. 56-56, 2007.

[26] M. Steinbauer, A. F. Molisch, and E. Bonek,“ The double-directional radio channel,” *IEEE Mag. Ant. and Pro.*, vol. 43, pp. 51-63, 2001.

[27] C. Balanis, “ Advanced engineering electromagnetics,” New York: John Wiley & Sons, 1999.

[28] J. Ling, D. Chizhik, and R. Valenzuela,“ Predicting multi-element receive and transmit array capacity outdoors with ray tracing,” *IEEE VTC.*, vol. 53, pp. 392-394, 2001.

[29] A. F. Molisch, and S. Member,“ A generic model for MIMO wireless propagation channels in macro- and microcells,” *IEEE Trans. on Signal Processing*, vol. 52, pp. 61-70, 2004.

[30] J. W. Wallace, and M. A. Jensen,“ Modeling the indoor MIMO wireless Channel,” *IEEE Trans. Antennas Propagat.*, vol. 50, pp. 591-600, 2002.

[31] D. Chizhik, F. Rashid-Farrokhi, and A. Lozano,“ Effect of antenna separation on the capacity of BLAST in correlated channels,” *IEEE Trans. Commu. Lett.*, vol. 4, pp. 1-3, 2000.

[32] W. Weichselberger, etc.,“ A stochastic MIMO channel model with joint correlation of both link ends,” *IEEE Trans. Wireless Commun.*, vol. 5, pp. 90-99, 2006.

[33] A. M. Sayeed,“ Deconstructing multiantenna fading channels,” *IEEE Transactions on Signal Processing*, vol. 50, pp. 2563-2579, 2002.

[34] A. F. Molisch, etc.,“ The COST 259 directional channel model: overview and methodology,” *IEEE Trans. Wireless Commun.* , vol. 5, pp. 3421-3433, 2006.

[35] H. El-Sallabi, etc.,“ Wideband spatial channel model for MIMO systems at 5 GHz in indoor and outdoor environ- ments,” *IEEE 63rd Vehicular Technology Conference* , vol. 6, pp. 2916-2921, 2006.

[36] V. Erceg, etc.,“ TGn channel mod-els,” *IEEE P802.11, Wireless LANs* , 2004. http://www.802wirelessworld.com/8802.

[37] 3GPP,“ Spatial channel model for MIMO simulations,” TR 25.996 V6.1.0, 2003. [Online]. Available: http://www.3gpp.org/

[38] Y. Fan and J. S. Thompson,“ MIMO configurations for relay channels: theory and practice,” *IEEE Wireless Commun.*, vol. 6, pp. 74-86, 2007.

[39] C. X. Wang, X. m. Hong, and X.h. Ge,“ Cooperative MIMO channel models: a survey,” *IEEE Commun. Mag.*, vol. 48, pp. 80-87, 2010.

[40] G. R. Maccartney, etc.,“ Millimeter-Wave omnidirectional path loss data for small cell 5G channel modeling,” *IEEE Access*, vol. 3, pp. 1573-1580, 2015.

[41] A. Roivainen,“ Parametrization and validation of geometry-based stochastic channel model for urban small cells at 10 GHz,” *IEEE Trans. Antennas Propagat.*, vol. 65, pp. 3809-3814, 2017.

[42] F. Letourneux, etc.,“ Dual-polarized channel measurement and modeling in urban macro- and small-cells at 2 GHz,” *IEEE WCNC.*, pp. 1-6, 2017.

[43] A. O. Kaya, D. Calin,“ Modeling three dimensional channel characteristics in outdoor-to-indoor LTE small cell environments,” *IEEE Commu. Conference*, pp. 933-938, 2013.

[44] R. Zhang, etc.,“ Cross-polarized three-dimensional channel measurement and modeling for small-cell street canyon scenario,” *IEEE Trans. on Vehicular Tech.*, Early Access, 2018.

[45] B. Pitakdumrongkij,“ Performance evaluation of massive MIMO with low-height small-cell using realistic channel models,” *IEEE Vehicular Tech. Conference*, pp. 1-5, 2016.

[46] B. Pitakdumrongkij,“ Performance evaluation of massive MIMO with low-height small-cell using realistic channel models,” *IEEE Vehicular Tech. Conference*, pp. 1-5, 2016.

[47] H. Xu, V. Kukshya, and T. S. Rappaport,“ Spatial and temporal characteristics of 60 GHz indoor channels,” *IEEE J. Sel. Areas Commun.*, vol. 20, pp. 620-630, 2002.

[48] A. Maltsev, R. Maslennikov, and A. Lomayev,“ Experimental investigations of 60 GHz wireless systems in office environment,” *IEEE J. Sel. Areas Commun.*, pp. 1488-1499, 2009.

[49] A. Maltsev, E. Perahia, and A. Khoryaev,“ Impact of polarization characteristics on 60 GHz indoor radio communication systems,” *IEEE Antennas Wirel. Propag. Lett.* , pp. 413-416, 2010.

[50] A. Maltsev, etc.,“ Statistical channel model for 60 GHz WLAN systems in conference room environment,” *IEEE EuCAP.* , pp. 1-5, 2010.

[51] S. G. Larew, T. A. Thomas, and A. Ghosh,“ Air interface design and ray tracing study for 5G millimeter wave communications,” *IEEE Globecom. Workshops*, pp. 117-122, 2013.

[52] Q. Li, G. Wu and T. S. Rappaport,“ Channel model for millimeter-Wave communications based on geometry statistics,” *IEEE Access*, pp. 427-432, 2014.

[53] M. Peter, etc.,“ A ray tracing based stochastic human blockage model for the IEEE 802.llad 60 GHz channel model,” *IEEE EuCAP*, pp. 3084-3088, 2011.

[54] W. Qi, J. Huang, R. Feng, C. X. Wang, and X. Ge,“ Measurements and modeling of human blockage effects for multiple millimeter wave bands,” *IEEE IWCNC*, pp. 1064-1069, 2017.

[55] J. Chen, X. Yin and S. Wang, “ Measurement-based massive MIMO channel modeling in 13-17 GHz for indoor hall scenarios,” *IEEE ICC*, pp. 1-5, 2016.

[56] J. Huang, R. Feng, J. Sun, C.-X. Wang, W. Zhang, and Y. Yang, “ Multi-frequency millimeter wave massive MIMO channel measurements and analysis,” *IEEE ICC*, pp. 1-6, 2017.

[57] M. K. Samimi and T. S. Rappaport, “ 3-D millimeter-wave statistical channel model for 5G wireless system design,” *IEEE Trans. Microw. Theory Techn.*, vol. 64, no. 7, pp. 2207-2225, 2016.

[58] Y. Tan, J. Huang, R. Feng, and C.-X, Wang, “ A study of angular stationarity of 5G millimeter wave channels,” *in Proc. ISWCS’18 Worshop*, 2017.

[59] T. S. Rappaport, etc., “ 38 GHz and 60 GHz angle-dependent propagation for cellular and peer-to-peer wireless communications,” *in Proc. IEEE ICC*, pp. 4568-4573, 2012.

[60] Y. Azar, etc., “ 28 GHz propagation measurements for outdoor cellular communications using steerable beam antennas in New York city,” *in Proc. IEEE ICC*, pp. 5143-5147, 2013.

[61] G. R. MacCartney and T. S. Rappaport, “ 73 GHz millimeter wave propagation measurements for outdoor urban mobile and backhaul communications in New York city,” *in Proc. IEEE ICC*, pp. 4862-4867, 2014.

[62] J. Huang, R. Feng, J. Sun, C.-X. Wang, W. Zhang, and Y. Yang, “ Multi-frequency millimeter wave massive MIMO channel measurements and analysis,” *IEEE VTC*, pp. 1-5, 2017.

[63] T. S. Rappaport, S. Sun, and F. Gutierrez,“ Millimeter wave mobile communications for 5G: It will work!” *IEEE Access*, vol. 1, pp. 335-349, 2013.

[64] S. Rangan, T. S. Rappaport, and E. Erkip,“ Millimeter-wave cellular wireless networks: Potentials and challenges,” *Proceedings of the IEEE*, vol. 102, pp. 366-385, 2014.

[65] L. P. David,“Enhanced intercell interference coordination challenges in heterogeneous Networks,” *IEEE Wireless Commun.*, vol. 18, pp.22-30, 2011.

[66] R. N. Almesaeed; et al., “3D channel models: Principles, Characteristics, and System Implications,” *IEEE Commun. Mag.*, vol. 55, pp.152-159, 2017.

[67] R. B. Ertel and J. H. Reed, “Angle and time of arrival statistics for circular and elliptical scattering models,” *IEEE J. Sel. Areas Commun.*, vol. 11, pp.1829-1840, 1999.

[68] N. M. Khan, et al., “A generalized model for the spatial characteristics of the cellular mobile channel,” *IEEE Trans. Veh. Technol.*, vol. 1, pp.22-37, 2008.

[69] M. Haenggi, et al., “Stochastic geometry and random graphs for the analysis and design of wireless networks,” *IEEE J. Sel. Areas Commun.*, vol. 7, pp.1029-1046, 2009.

[70] A. F. Molisch, “Modeling of directional wireless propagation channels,” . *URSI Radio Science Bulletin*, vol. 302, pp.16-26, 2002.

[71] W. C. Jakes and D. C. Cox, “Microwave Mobile Communications,” *Wiley-IEEE Press*, 1994.

[72] S. S. Mahmoud, Z.M. Hussain, O.S. Peter, “A space-time model for mobile radio channel with hyperbolically distributed scatterers,” *IEEE Antennas Wirel. Propag. Lett.* , vol. 1, pp.211-214, 2002.

[73] M. Alsehaili, et al., “Angle-of-Arrival statistics of a three-dimensional geometrical scattering channel model for indoor and outdoor propagation environments,” *IEEE Antennas Wireless Propagat. Lett.*, vol. 9, pp.946-949, 2010.

[74] A. Kammoun, et al., “. Preliminary results on 3DD channel modelling: from theory to standardization,” *IEEE J. Sel. Areas Commun.*, vol. 32, pp.1219-1229, 2014.

[75] T. Aulin, “A modified model for the fading Signal at a mobile radio channel,” *IEEE Trans. Veh. Technol.*, vol. 28, pp.182-204, 1979.

[76] T. Taga, “Analysis for mean effective gain of mobile antennas in land mobile radio environments,” *IEEE Trans. Veh. Technol.* , vol. 39, pp.117-131, 1990.

[77] P. Petrus, et al., “Geometrical-based statistical macrocell channel model for mobile environments,” *IEEE Trans. Commun.*, vol. 3, pp.495-502, 2002.

[78] M. Shafi, “The impact of elevation angle on MIMO capacity,” *IEEE ICC.*, pp.4155-4160, 2006.

[79] S. J. Nawaz, “A generalized 3-D scattering model for a macrocell environment with a directional antenna at the BS,” *IEEE Trans. Veh. Technol.*, vol. 7, pp.3193-3204, 2010.

[80] C. Dimitrios, et al., “Resonant scattering characteristics of homogeneous dielectric sphere,” *IEEE Trans. Antennas Propagat.* , vol. 6, pp.3184-3191, 2017.

[81] S. Qu and T. Yeap, “A Three-dimensional scattering model for fading channels in land mobile environment,” *IEEE Trans. Veh. Technol.*, vol. 3, pp.765-781, 1999.

[82] K. Kalliola, et al., “Angular power distribution and mean effective gain of mobile antenna in different propagation environments,” *IEEE Trans. Veh. Technol.*, vol. 5, pp.823-838, 2002.

[83] B. Mondal, et al., “3D channel model in 3GPP,” *IEEE Commun. Mag.* , vol. 3, pp.16-23, 2015.

[84] M. Ballot, “Radio-wave propagation prediction model tuning of land cover effects,” *IEEE Trans. Veh. Technol.*, vol. 8, pp.3490-3498, 2014.

[85] T. Kurner, "Radio wave propagation part one "theoretical aspects"," *1st COST2100 Training School.*, Wroclaw, Poland, 2008.

[86] Y. Lostanlen, "Radio wave propagation part two "practical aspects".," *1st COST2100 Training School.*, Wroclaw, Poland, 2008.

[87] M. Klepal, "Novel approach to indoor electromagnetic wave propagation modelling," Ph.D. dissertation, Czech Technical University, Prague. 2003.

[88] R. Janaswamy, "Angle and time of arrival statistics for the Gaussian scatter density model," *IEEE Trans. Wireless Commun.*, vol. 3, pp.488-497, 2002.

[89] R. Hoppe, G. Wolfle and F. Landstorfer, "Accelerated ray optical propagation modelling for the planning of wireless communication networks," *IEEE Raido and Wirelss Conference.*, RAWCON 99, 1999.

[90] Z. Lai, et al., "An intelligent ray launching for urban propagation prediction," *IEEE EuCAP.*, pp.2867-2871, 2009.

[91] Z. Lai, et al., "A performance evaluation of a grid-enabled object-oriented parallel outdoor ray launching for wireless network coverage prediction," *IEEE EuCAP.*, pp.38-43, 2009.

[92] Z. Lai, et al., "A new approach to solve angular dispersion of discrete ray launching for urban scenarios," *Loughborough Antennas and Propagation Conference.*, pp.133-136, 2009.

[93] Z. Lai, et al., "The characterisation of human-body influence on indoor 3.5 GHz path loss measurement," *Second International Workshop on Planning and Optimization of Wireless Communication Networks*, 2010.

[94] D. Umansky, et al., "A new deterministic hybrid model for indoor-to-outdoor radio coverage prediction," *IEEE EuCAP.*, pp.3771 - 3774, 2011.

[95] D. L. Roche, et al., "Combination of geometric and finite difference models for radio wave propagation in outdoor to indoor scenarios," *IEEE EuCAP.*, 2010.

[96] D. L. Roche, et al., “Optimized implementation of the 3D MR-FDPF method for indoor radio propagation prediction,” *IEEE EuCAP.*, 2009.

[97] D. L. Roche, et al., ‘Implementation and validation of a new combined model for outdoor to indoor radio coverage predictions,” *Hindawi Publishing Corporation EURASIP Journal on Wireless Communications and Networking.*, 2010.

[98] J. Weng, et al., “Indoor Massive MIMO Channel Modelling Using Ray-Launching Simulation,” *International Journal of Antenna and Propagation.*, 2014.

[99] Ranplan, “The Role and Benefits of RF and Performance Modelling Tools in the HetNet Era.” White Paper. 2015. Available online: https://ranplanwireless.com/wp-content/uploads/The-Role-and-Benefits-of-RF-and-Performance-Modelling-tools-in-HetNet-Era.pdf (31.12.2017)

[100] S. Donikian., “Vuems: a virtual urban environment modelling system,” *Proceedings Computer Graphics International.*, pp.84-92, 1997.

[101] G. D. Durgin and T. S. Rappaport,“Theory of multipath shape factors for small-scale fading wireless channels,” *IEEE Trans. Antennas Propag.*, vol. 48, pp.682-693, May 2011.

[102] K. Junghoon, et al., “ Millimeter-Wave channel measurements and analysis for statistical spatial channel model in in-building and urban environments at 28 GHz,” *IEEE Trans. Wireless Commun.*, vol. 16, pp.5853-5868, 2017.

[103] J. Thomas, et al., “A Geometry-Based channel model to simulate an Averaged-Power-Delay profile,” *IEEE Trans. Antennas Propag.*, vol. 65, pp.4925-4930, Sep. 2017.

[104] R. Zhang, et al., “Measurement and modeling of angular spreads of Three-Dimensional urban street radio channels,” *IEEE Trans. Veh. Technol.*, vol. 66, pp.3555-3570, 2017.

[105] J. H. Zhang, et al., “Three-dimensional fading channel models: A survey of elevation angle research,” *IEEE Mag. Commun.*, vol. 52, pp.218-226, 2014.

[106] T. Aulin,“A modified model for the fading signal at a mobile radio channel,” *IEEE Trans. Vehic. Tech.*, vol. 28, pp.182-204, Aug. 1979.

[107] T. Taga,“Analysis for mean effective gain of mobile antennas in land mobile radio environments,” *IEEE Trans. Vehic. Tech.*,vol. 39, pp.117-131, May 1990.

[108] P. Petrus, et al., “Geometrical-Based statistical macrocell channel model for mobile environments,” *IEEE Trans. Commun.*, vol. 50, pp.495-502, 2002.

[109] S. J. Nawaz, “A generalized 3-D scattering model for a macrocell environment with a directional antenna at the BS,” *IEEE Trans. Vehic. Tech.*, vol. 59, pp.3193-3204, Sep. 2010.

[110] R. Zhang, et al., “Angle and time of arrival statistics for the Gaussian scatter density model,” *IEEE Trans. Veh. Technol.*, vol. 66, pp.3555-3570, 2017.

[111] R. Janaswamy, “Angle and time of arrival statistics for the Gaussian scatter density model,” *IEEE Trans. Wireless Commun.*, vol. 1, pp.488-497, July 2002.

[112] K. N. Le, “On angle-of-arrival and time-of-arrival statistics of geometric scattering channels,” *IEEE Trans. Vehic. Tech.*, vol. 58, pp.4257-4264, Oct. 2009.

[113] A. Mohammad, et al., “Angle-of-Arrival statistics of a three-dimensional geometrical scattering channel model for indoor and outdoor propagation environments,” *IEEE Ant. Wireless Prop. Lett.*, vol. 9, pp.946-949, 2010.

[114] L. Schumacher, K. I. Pedersen, and P. E. Mogensen, “From antenna spacings to theoretical capacities—Guidelines for simulating MIMO systems,” *IEEE Int. Symp. Pers.*, vol. 2, pp.587-592, 2002.

[115] K. I. Pedersen, P. E. Mogensen, and B. H. Fleury, “Spatial channel characteristics in outdoor environments and their impact on BS antenna system performance,” *IEEE Veh. Technol. Conf.*, vol. 2, pp.719-723, 1998.

[116] A. Forenza, et al., " Simplified spatial correlation models for clustered MIMO channels with different array configurations," *IEEE Trans. Veh. Technol.*, vol. 56, no. 4, pp.1924-1934, 2007.

[117] R. N. Almesaeed, et al., " 3D Channel Models: Principles, Characteristics, and System Implications," *IEEE Commun. Mag.*, vol. 55, no. 4, pp.152-159, 2017.

[118] T. Aulin, " "A Modified Model for the Fading Signal at a Mobile Radio Channel," *IEEE Trans. Vehic. Tech.*, vol. 28, pp.182-204, 1979.

[119] S. Qu and T. Yeap, "A three-dimensional scattering model for fading channels in landmobile environment," *IEEE Trans. Vehic. Tech.*, vol. 48, no. 3, pp.765-781, 1999.

[120] D. I. Axiotis; M. E. Theologou, "An empirical model for predicting building penetration loss at 2 GHz for high elevation angles," *IEEE Ant. Wireless Prop. Lett.*, vol. 2, pp.234-237, 2003.

[121] H. Jiang, et al., "A novel 3D massive MIMO channel model for vehicle-to-vehicle communication environments," *IEEE Trans. Commun.*, 2017.

[122] J. C. Liberti, T. S. Rappaport, " A geometrically based model for line-of-sight multipath radio channels," *IEEE VTC.*, vol. 2, pp.844-848, 1996.

[123] C. Dimitrios, et al. "Resonant scattering characteristics of homogeneous dielectric sphere," *IEEE Trans. Ant. Pro.*, vol. 65, pp.3184-3191, 2017.

[124] R. Alina, et al. "Some features of electromagnetic scattering by radially inhomogeneous DNG spheres," *IEEE Eucap.*, vol. 11, pp.1096-1100, 2017.

[125] S. Bektas. "Intersection of an ellipsoid and a plane" *International Journal of Research in Engineering and Applied Sciences,*, vol. 6, pp.273-283, 2016.

[126] B. BADIC, et al., " Energy efficient radio access architectures for green radio: large versus small cell size deployment" *IEEE VTC-Fall, 2009.*, pp.1-5, 2009.

[127] T. S. Rappaport and etc.,‘Millimeter wave mobile communications for 5G cellular: It Will Work!,” *IEEE Access.*, vol. 1, pp.335-349, 2013.

[128] G. Liang and H. L. Bertoni,“A new approach to 3D ray tracing for propagation prediction in cities,” *IEEE Trans. Ant. Pro.*, vol. 46, pp.853-863, 1998.

[129] M. C. Lawton and J. P. McGeehan,“The application of a deterministic ray launching algorithm for the prediction of radio channel characteristics in small-cell environments,” *IEEE Trans. Veh. Technol.*, vol. 43, pp.955-969, 1994.

[130] Z. Dai and etc.,“ UAV-aided source localization in urban environments based on ray launching simulation,” *IEEE USNC/URSI*, pp.595-596, 2017.

[131] F. Casino and etc.,“ Optimized wireless channel characterization in large complex environments by hybrid ray launching-collaborative filtering approach,” *IEEE Trans. Ant. Pro.*, vol. 16, pp.780-783, 2017.

[132] V. Degli-Esposti and etc.,“Measurement and modelling of scattering from buildings,” *IEEE Trans. Ant. Pro.*, vol. 55, pp.143-153, 2007.

[133] C. Jansen and etc.,“Diffuse Scattering From Rough Surfaces in THz Communication Channels,” *IEEE Trans. Terahertz Science and Tech.*, vol. 1, pp.462-472, 2011.

[134] E. Masson and etc.,“Radio wave propagation in curved rectangular tunnels at 5.8 GHz for metro applications,” *EURASIP Journal on Wireless Communications and Networking*, pp.81-85, 2011.

[135] D. Solomitckii and etc.,“Characterizing the impact of diffuse scattering in urban millimeter-wave deployments,” *IEEE Wire. Commun. Lett.*, vol. 5, pp.432-435, 2016.

[136] R. Hoppe; G. Wolfle; F. Landstorfer,“Accelerated ray optical propagation modelling for the planning of wireless communication networks,” *IEEE Raido and Wirelss Conference*, 1999.

[137] V. Degli-Esposti and H. L. Bertoni,“Evaluation of the role of diffuse scattering in urban microcellular propagation,” *IEEE VTC*, 1999.

[138] V. Degli-Esposti,“A diffuse scattering model for urban propagation prediction,” *IEEE Trans. Ant. Pro.*, vol. 49, pp.1111-113, 2001.